



universität  
wien

# DISSERTATION

Titel der Dissertation

„Experiments on  
Quantum Frequency Conversion of Photons“

Verfasser

Dipl. Phys. Sven Ramelow

angestrebter akademischer Grad

Doktor der Naturwissenschaften (Dr. rer. nat.)

Wien, 2011

Studienkennzahl lt. Studienblatt: A 091 411

Dissertationsgebiet lt. Studienblatt: Physik

Betreuerin / Betreuer: o. Univ.-Prof. Dr. DDr. h.c. Anton Zeilinger

This work was carried out in the Group of Prof. Anton Zeilinger at the Vienna Institute of Quantum Optics and Quantum Information (IQOQI) from the Austrian Academy of Sciences.

The different sources of funding that have contributed to this work are: the doctoral program on Complex Quantum Systems (CoQuS) and the SFB FoQus funded by the Austrian Science Fund (FWF), the European Research Council (ERC) under the Advanced Grant QIT4QAD, as well as the John Templeton Foundation via a Templeton Fellowship.

# Contents

0.1	Abstract . . . . .	5
0.2	Zusammenfassung . . . . .	6
<b>1</b>	<b>Introduction</b>	<b>9</b>
<b>2</b>	<b>Single-photon upconversion (SPUC)</b>	<b>13</b>
2.1	Introduction . . . . .	14
2.2	Principles . . . . .	19
2.2.1	Photonic entanglement . . . . .	19
2.2.2	Parametric processes . . . . .	23
2.2.3	Quasi-phase-matching . . . . .	29
2.3	Setup . . . . .	32
2.3.1	Entangled photon source . . . . .	32
2.3.2	Optimal focussing for SPUC . . . . .	36
2.3.3	Setup for polarization coherent upconversion . . . . .	38
2.4	Results . . . . .	43
2.4.1	Efficiency and background . . . . .	43
2.4.2	Polarization coherent SPUC . . . . .	44
2.5	Conclusions and outlook . . . . .	54
2.6	Publication arXiv:1106.1867 . . . . .	55
<b>3</b>	<b>Coherent photon conversion (CPC)</b>	<b>61</b>
3.1	Introduction . . . . .	62
3.2	Principles . . . . .	65
3.2.1	Coherent photon conversion . . . . .	65

3.2.2	Applications of efficient CPC . . . . .	67
3.2.3	Coherent photon conversion efficiency . . . . .	74
3.2.4	Pair creation from four-wave mixing . . . . .	79
3.3	Experimental Setup . . . . .	82
3.3.1	Coherent photon conversion setup . . . . .	82
3.3.2	Photonic crystal fibers and phase-matching . . . . .	85
3.4	Results . . . . .	88
3.4.1	Pair creation in the PFC . . . . .	88
3.4.2	Coherent photon conversion in PCF . . . . .	90
3.5	Conclusions and Outlook . . . . .	100
3.6	Publication Nature 478, 360-363 (2011) . . . . .	101
<b>4</b>	<b>Discrete, tunable color-entanglement</b>	<b>107</b>
4.1	Introduction . . . . .	108
4.2	Publication Phys. Rev. Lett. 103, 253601 (2009) . . . . .	109
<b>5</b>	<b>Conclusions and Outlook</b>	<b>115</b>
<b>6</b>	<b>Acknowledgements</b>	<b>129</b>

## 0.1 Abstract

Coherently converting photons between different states offers intriguing new possibilities and applications in quantum optical experiments. In this thesis three experiments on this theme are presented.

The first experiment demonstrates the *quantum frequency conversion of polarization entangled photons*. Coherent frequency conversion of single photons offers an elegant solution for the often difficult trade-off of choosing the optimal photon wavelength, e.g. regarding optimal transmission and storage of photons in quantum memory based quantum networks. In our experiments, we verify the successful entanglement conversion by violating a Clauser-Horne-Shimony-Holt (CHSH) Bell inequality and fully characterised our close to unity fidelity entanglement transfer using quantum state- and process tomography. Our implementation is robust and flexible, making it a practical building block for future quantum technologies.

The second part of the thesis introduces a deterministic scheme for photonic quantum information processing. While single photons offer many advantages for quantum information technologies, key unresolved challenges are scalable on-demand single photon sources; deterministic two-photon interactions; and near 100%-efficient detection. All these can be solved with a single versatile process – a novel four-wave mixing process that we introduce here as a special case of the more general scheme of *coherent photon conversion* (CPC). It can provide valuable photonic quantum processing tools, from scalably creating single- and multi-photon states to implementing deterministic entangling gates and high-efficiency detection. Notably, this would enable scalable photonic quantum computing. Using photonic crystal fibres, we experimentally demonstrate a nonlinear process suited for coherent photon conversion. We observe correlated photon-pair production at the predicted wavelengths and experimentally characterise the enhancement of the interaction strength by varying the pump power. We further explain how current technology can provide a feasible path towards deterministic operation. Our scheme could also be implemented in opto-mechanical or superconducting systems which can exhibit extremely strong intrinsic nonlinearities.

The third experiment demonstrates the creation and verification of *discrete color entanglement*. We experimentally create high-quality, discretely color-entangled states by transferring polarization entanglement of non-degenerate photons onto the color. We then unambiguously verify and quantify the amount of entanglement by reconstructing a restricted density matrix. Our technique can be generalized to transfer polarization entanglement for example onto orbital angular momentum.

## 0.2 Zusammenfassung

Koherent Photonen zwischen verschiedenen Zuständen zu konvertieren eröffnet faszinierende neue Möglichkeiten und Anwendungen in Quantenoptik-Experimenten. In dieser Arbeit werden drei Experimente zu dieser Thematik vorgestellt.

Das erste Experiment demonstriert Quanten-Frequenzkonversion von polarisationsverschränkten Photonen. Kohärente Frequenzkonversion einzelner Photonen bietet eine elegante Lösung für den oft schwierigen Kompromiss die optimale Wellenlänge zu finden: beispielsweise bezüglich der optimalen Übertragung und Speicherung in Quantennetzwerken. In unseren Experimenten verifizieren wir die erfolgreiche Konversion der Verschränkung durch die Verletzung einer Clause-Horne-Shimony-Holt (CHSH) Bell-Ungleichung. Ausserdem wird der fast optimale Verschränkungstransfer genau durch Quantenzustands - und Quantenprozess - Tomografie charakterisiert. Unsere Implementation ist robust und flexibel und dadurch ein geeigneter Baustein für zukünftige Quantentechnologien.

Der zweite Teil der Arbeit widmet sich der Vorstellung eines neuen deterministischen Schemas zur photonischen Quanteninformationsverarbeitung. Während einzelnen Photonen viele Vorteile für Quanteninformationstechnologien aufweisen, sind die bisher ungelösten Herausforderungen deterministische Einzelphotonen-Quellen, deterministische Photon-Photon Wechselwirkungen sowie nahe 100% effiziente Detektion. All diese können mit einem einzigen, vielseitigen Prozess gelöst werden – einem Vier-Wellen-Mischungsprozess der hier als Spezialfall des generellerem Schemas der "Kohärenten Photonen-Konversion" vorgeschlagen wird. Dies kann viele, wertvolle Werkzeuge für die Quantenverarbeitung bereitstellen, angefangen von skalierbaren Multi-Photonen-Quellen, über die Implementation von deterministischen Verschränkungsgattern bis hin zur Ermöglichung hocheffizienter Einzelphotonen-Detektion. Beachtlicherweise würde sogar skalierbares optisches Quantencomputing ermöglicht. In unserem Experiment demonstrieren wir mit Hilfe von Photonischen-Kristall-Fasern einen Vier-Farben nichtlinearen Prozess, der für die "Kohärente Photonen-Konversion" geeignet wäre. Dafür weisen wir die Erzeugung korrelierter Photonenpaare bei den vorhergesagten Wellenlängen nach und bestimmen quantitativ die lineare Verstärkung der Wechselwirkung abhängig von der benutzten Pumpleistung. Wir erörtern weiterhin, wie man mit Hilfe derzeitiger Technologie in das angestrebte Regime der deterministischen Wechselwirkung gelangen könnte. Ausserdem könnte das vorgeschlagene Prinzip auch in anderen physikalischen Systemen, wie opto-mechanischen, elektromechanischen oder supraleitenden Sys-

temen eingesetzt werden, welche auch zum Teil sehr hohe intrinsische Nicht-linearitäten aufweisen.

Im dritten Experiment wird die Erzeugung und der Nachweis von diskreten Farb-verschränkten Zuständen beschrieben. Wir erzeugen diese Zustände durch die Übertragung von Polarisationsverschränkung von nicht-degenerierten Photonenpaaren auf den Farb-Freiheitsgrad. Wir weisen dann streng die Verschränkung nach und quantifizieren den Grad der Verschränkung mithilfe der Rekonstruktion einer reduzierten Dichtematrix. Unsere Technik kann generalisiert werden um den Transfer von Polarisationsverschränkung auf andere photonische Freiheitsgrade zu ermöglichen wie zum Beispiel den Bahndrehimpuls der räumlichen Moden einzelner Photonen.





# Chapter 1

## Introduction

Photons are in many aspects ideal for studying a wide range of quantum phenomena. They are virtually immune from interactions from their environment that would destroy their quantum properties and can be handled relatively easy and very precisely with well established optical techniques.

On the other hand, producing single and entangled photon states is a not yet in all aspects sufficiently solved technical challenge. In the beginning of the history of experiments with entangled photons stood a purely fundamental motivation: testing Bell inequalities [8, 15] to experimentally exclude local-realistic world views [28, 6]. Technologically, the first sources of polarization entangled photons employed for these pioneering experiments in photonic quantum optics were based on cascaded transitions in atoms. However, these sources required bulky vacuum setups and featured only a low brightness - mostly because of the non-directional emission of the photon pairs. A break-through was the development sources of pairs of (entangled) photons [47] based on spontaneous parametric down-conversion (SPDC). SPDC is a second order ( $\chi^{(2)}$ ) nonlinear process where a pump photon converts into two lower energy photons - a photon pair. Quickly this has become the standard technique for photon pair creation in the new developing field of optical quantum information processing and quantum communication including the first already commercialized application of quantum key distribution.

In other words: *nonlinear optics* became the physical basis for the *production* of photon pairs and entanglement and was used in a plethora of experiments.

In another important conceptual step, linear optics was shown to be sufficient for enabling universal optical quantum computing [41], provided deterministic photon sources and quantum memories are available. Indeed, based on SPDC and using simple linear optical elements like (polarizing) beam splitters and wave-plates, up to 6-qubit quantum computing schemes have been demonstrated and moreover the creation of multi-photon entanglement up to 8 entangled photons. However, there are serious drawbacks when using only SPDC and linear optics: most importantly it only provides intrinsically inefficient production and of multi-photon states, as well as only probabilistic and inefficient interactions between photons.

The idea of using non-linear optics not only for the creation of photonic states, but also for their manipulation is a general approach for breaking these roadblocks and moreover gives access to so far unexplored effects. The three experiments presented in this thesis revolve around this motive: *Using nonlinear optics and enable the conversion of photons* with respect to various degrees-of-freedom.

The main theme of converting photons using nonlinear optics has been addressed in the last 5 years there with a first serious line of experiments concentrating on changing the wavelength of (entangled) photons (see chapter 2.1 and references therein). The primary motivation for this series of experiments was mainly a technological one: changing the photon wavelength from the telecommunication wavelength 1550 nm (lowest loss in glass fibers) to the visible regime, where better detectors are available, than for 1550 nm. The main application for this would be fiber based QKD. However, coherently converting photons between different wavelengths addresses a much broader class of problems including beside quantum communication contexts also a variety of building blocks for quantum information processing: In general it can provide an elegant solution whenever a single wavelength is not suited optimally for every necessary task (e.g. transmission, storage, manipulation, detection).

The experiment, presented in chapter 2 of this thesis addresses the issue of coherently converting photons between different wavelengths, while preserving their polarization entanglement – an important degree-of-freedom for its ease of control and precise measurement and for which this was so far not been demonstrated. The results show, that nonlinear optics is in practice indeed fully suited to coherently convert photon states with a very high fidelity – in this case preserving polarization entanglement. Aiming at higher

conversion efficiencies combined with possibly moving to integrated optics architectures realizing integrated nonlinear optics is a promising route for future conceptual and experimental studies.

To fully appreciate the potential that converting photonic states with nonlinear optical processes has, one has to go a step further. As soon as three or more fully quantized optical modes interact with each other in a nonlinear medium with a second (or higher) order nonlinearity the dynamics has no more any classical analogue. This is in contrast to e.g. photon upconversion, where only two of the three interacting fields are quantized optical modes and the third is the classical (coherent) pump beam being classically analogue to the well known process of sum frequency generation.

An approach that directly utilises this potential of nonlinearly converting photonic states is the concept of "coherent photon conversion" (CPC) [49] that is introduced and presented in chapter 3 of this thesis. A main aspect of CPC is, that by using strong pump fields higher order nonlinearities can be turned into effective lower order nonlinearities for the remaining interacting modes. The most practically important example is that a strong pump field transforms a third order ( $\chi^{(3)}$ ) nonlinearity that mediates a four-wave-mixing interaction into an effective second order ( $\chi^{(2)}$ ) nonlinearity for the remaining three modes. Importantly, for a sufficiently high enough effective interaction strength which can be tuned and enhanced by the pump laser, several novel effects can be achieved: for example, the deterministic doubling of single photons becomes possible, as well as a new type of photon-photon-interaction and moreover a type of down-conversion with much lower error terms. These would open up a new field of experimental and conceptual possibilities, including the implementation of a nonlinear optical quantum computer.

The main challenge of this proposed schemes lies in reaching sufficiently high nonlinear interaction-strength. The results of a first experimental step are presented in chapter 3 as well. The main conclusion is, that a tunable effective  $\chi^{(2)}$  can indeed be realized in a  $\chi^{(3)}$  medium – in our case a highly nonlinear photonic crystal fiber made from silica glass. Moreover, the measured nonlinear interaction strength – while not being in the high efficiency regime necessary to start harnessing the full potential of CPC – implies that with other materials like highly nonlinear glasses this is within reach with current technology. This conclusion already determines the outlook: that future conceptual and experimental efforts need to be aimed at demonstrating high enough interaction strengths. Moreover, future more detailed theoretical studies could reveal fundamental effects of CPC, that itself could be another

goal of experimental efforts.

An interesting direct consequence of using nonlinear optics for processing photonic states is that it naturally gives access to the energy (or frequency) degree-of-freedom of photons. This is one of the most intuitive degrees-of-freedom of light. Noteworthy, using different frequency bands in parallel wavelength division multiplexing has revolutionized classical fiber-optical communication technology. The fact that no discretely frequency entangled states of photons have been prepared before, gave the motivation for demonstrating this in the experiment presented in chapter 4 of this thesis. Because of the widely separated frequencies we called this type of entanglement "colour entanglement". The states are created by coherently converting polarization entanglement into colour entanglement. The experiment not only resulted in a novel way of verifying and quantifying discrete frequency entanglement (by anti-bunching in non-classical two-photon interference) but also established the general idea to convert polarisation entanglement (which is relatively easy to produce with high fidelity) to other degrees-of-freedom. The latter is even already used in new experiments that use a conversion to orbital angular momentum as proposed in the publication of this experiment [66].

## Chapter 2

# Single-photon upconversion (SPUC)

## 2.1 Introduction

The ability to change the wavelength of single photons has fundamental importance as it gives access to its frequency (or energy) degree-of-freedom. This is one of the most intuitive degrees of freedom for light, but is also of immense practical importance: In many experiments with single photons the wavelength is a trade-off between different experimental requirements and technical limitations. These include for example the performance of single photon detectors in the chosen wavelength regime, transmission and dispersion properties of the materials or the availability of laser sources. Moreover, when atomic media are involved, one can only use a restricted number of (typically narrow-band) electronic transitions that are at fixed wavelengths (and only slightly shift-able by external fields).

One illustrative example for such a trade-off are multi-photon experiments. Here, high detection efficiencies ( $\eta$ ) are crucial, because they severely influence the final rate of  $N$ -fold coincidences proportional to  $\eta^N$ . The highest detection efficiency for commercially available devices is currently achieved by silicon based avalanche photon diodes (Si-APDs) operated in Geiger-mode, which have their highest efficiency between 550 nm and 850 nm. This is the reason, why virtually all multi-photon experiments are carried out in this wavelength regime, and not for example at the telecommunication wavelength of 1550 nm.

Another example connected to this, where the trade-off is very hard is fiber-based quantum key distribution [32]. Because optical fibers have their absorption minimum at the telecom band around 1550 nm one uses photons at this wavelength to get to longest transmission distances. However, InGaAs-based APDs that have been the only commercially available choice for single photon detection at this wavelength have a poor performance compared to Si-APDs, which unfortunately are not sensitive at 1550 nm. Converting the photons from 1550 nm to a wavelength accessible for Si-APDs is one way of solving this detection problem [18, 82].

A third and important example concerns quantum networks which are a key requirement for large-scale deployment of quantum communication [73] for example for global, unconditionally secure communication. Building a quantum network requires the distribution of entanglement using flying qubits (photons) between quantum repeater nodes which can coherently store entanglement using quantum memories and concatenate it by entanglement swapping [61]. The standard wavelength for optical fiber transmission is 1550 nm, where optical loss is minimal, whereas currently the highest quantum memory efficiencies have been achieved in Rubidium vapour at around

800 nm. One key element of a quantum network is therefore a quantum interface converting between the different wavelengths of flying qubits and quantum memories.

These examples illustrate that the possibility of transferring single photons from one wavelength to another can be an ubiquitous building block for a diverse range of future quantum technologies (and even for some classical optics applications at the single photon level [52]).

In the following, a summary of previous experimental works connected to single photon conversion will be given which will in detail illustrate the associated experimental challenges and also further applicabilities.

### Overview of previous works on single photon conversion

One of the first considerations of transferring quantum states of light from one frequency to another is given in [44]. This work proposes a scheme for transferring continuous-variable encoded states in the form of squeezed states from 1064 nm to 420 nm with a pump at 694 nm. It is theoretically shown that for high enough pump powers 100% conversion efficiency can be achieved in principle and, more importantly, that the quantum state of light is conserved in the conversion. As a motivation for this the usefulness of a tunable squeezed light source is pointed out. This proposal was two years later demonstrated experimentally (slightly modified from the proposal) [36]. There, the observation of the conversion of one mode of a pair of 1064 nm beams that is non-classically intensity correlated to beam at 532 nm is reported. The preservation of non-classical intensity correlations between the converted beam at 532 nm and the unconverted beam at 1064 nm is shown by a reduction of the intensity noise by 1.5 dB below the classical limit.

In another early work on single photon conversion the possible application of achieving fs timing resolution single photon counting was demonstrated in an experiment [55], where photons at 700 nm stemming from single molecules of Oxazine 725 in a micro cavity were converted with fs-pulses at 615 nm to 327 nm with an intrinsic efficiency of 40%.

In 2002, the role of frequency conversion of discretely entangled quantum states of light especially in the context of long-distance quantum communication with the help of quantum memories has been recognized by Shapiro [75]: Specifically, he proposes the conversion of polarization entangled photon pairs at 1570 nm, which would be ideally suited for long-distance fiber transmission, to 795 nm at which they could be stored in Rb-based quantum memories. The proposed pump wave length is 1608 nm with a conversion

crystal made from periodically poled  $\text{LiNbO}_3$  (ppLN). As one of the first experimental demonstrations at the single photon level, in 2003, the phase preserving conversion of photons at 876 nm from an attenuated diode laser to 417 nm with a pulsed pump at 795 nm has been reported [30]. The phase-preserving characteristic of the upconversion has been verified by having a two path interferometer, converting the photons in both arms and showing that the interferometer fringes of the 876 nm light and the 417 nm show the same phase period.

In the following years, a number of experiments focussed on using single photon conversion to enhance the detection of photons at 1550 nm by converting this wavelength to one in the visible optical regime, where Si-based avalanche photo diodes (APDs) can be used. Si-APDs have much better performance characteristics than InGaAs-APDs, that are used for the detection of photons at 1550 nm.

To achieve high conversion efficiencies different methods were used: in [3] the pump laser at 1064 nm was enhanced in an actively locked travelling-wave cavity to more than 20 W circulating pump power. With a 40 mm long ppLN (type I) crystal an intrinsic conversion efficiency from 1550 nm to 633 nm of about 90% could be observed. At the maximal intrinsic conversion efficiency pump-induced dark count rates of 500 kcps were observed. In a later work of this group, the polarization independent conversion for classical input light could be shown by a double-pass Michelson type interferometric configuration [2]. No data for single photon input was reported nor quantitative information about performance at the single photon level.

A similar approach of using cavity enhanced pump fields was reported in [60] with an intra-cavity design for the 1064 nm pump laser for converting 1550 nm to 633 nm.

Another way of achieving high enough conversion efficiencies to be useful for replacing InGaAs-detectors is to use the high peak powers of pulsed lasers with the drawback of having to synchronize the to be converted photons with the pump escort pulses, which excludes cw operation. In [83] pulses at 1064 nm with 7.2 kHz repetition rate were used to convert photons from 1550 to 631 nm. Near unity intrinsic upconversion efficiency could be measured, unfortunately also accompanied by high levels of pump induced dark counts. Later on, based on this work the group could further show the phase coherence of the upconversion setup by making use of a Michelson-type two arm configuration and observing the corresponding fringes [85]. Also with this scheme of high intensity escort pulses by using the  $\pi$ -phase shift that is achieved by a full conversion to 631 nm and back to 1550 nm a fast all-optical



switch at a telecom wavelength could be implemented [84].

In [71] ppLN waveguides were used to achieve high conversion efficiencies of 1550 nm to 713 nm with moderate pump powers at 1320 nm of only around 100 mW. In a later experiment of this group, the conversion at the single photon level was demonstrated [51] revealing pump induced dark count rates around 800 kcps. In the same paper also the conversion of 1320 nm photons with the pump at 1550 nm was demonstrated with much reduced pump induced dark counts. As a reason for the lower noise it was pointed out that in this combination the pump has a lower photon energy than the input and therefore Raman scattering is suppressed. Other results for using ppLN waveguides for single photon conversion were reported in [22]: Here a pulsed pump at 1530 nm is used to convert 1550 nm input light to 770 nm - again high rates of pump induced background counts (via Raman scattering) were seen.

As suggested from its first observation [3], the production of pump induced dark counts can be strongly suppressed by using a pump wavelength, which has lower energy than input (and output) field, because Raman processes that are responsible for this noise are typically much weaker for the anti-stokes side (higher energy). This could be experimentally demonstrated: in [20] 1064 nm light was converted to 632 nm with a ps pulsed pump laser at 1550 nm. Near unity intrinsic efficiency was observed, while no pump induced background counts could be observed. Similarly, [39] reports on the conversion of 1550 nm to 830 nm with a pump laser at 1810 nm (thulium doped fiber laser) in a ppLN waveguide achieving 40% intrinsic conversion efficiency with 26 mW (cw) pump power.

In the first experiment showing the conversion of entangled photons [81], time-bin entangled photons were converted from 1312 nm to 712 nm with a pump field at 1560 nm. The entanglement of the 1312 nm photons to their partner photons at 1555 nm is conserved and the entanglement of the 712/1555 nm photons is verified by measuring non-local correlation fringes with appropriately aligned unbalanced Mach-Zehnder interferometers and post-selection on arrival time differences.

An interesting use of single photon conversion was reported in [79] where photons at different wavelengths were made spectrally indistinguishable by the conversion to the same wavelength. The indistinguishability was demonstrated by two-photon-interference.

The reverse process of upconversion has also been shown: photons have been "down-converted" to lower energies using single photon difference frequency generation (DFG): in [17] photons from an attenuated diode laser at 710 nm

were converted to 1310 nm with a 1550 nm pump laser. It was further demonstrated that coherent time encoding ("pseudo time bin qubits") of the input was conserved in the output with high fidelity. A similar experiment was reported in [80] where also photons at 710 nm were converted to 1310 nm while preserving the phase encoding of the input photons.

Single photon conversion with very short pump pulses can also be used to bring the timing resolution of photon detection in the fs-regime. This has been experimentally demonstrated in [46] where 150 fs pump pulses at 790 nm were used to convert both 1580 nm photons generated by SPDC pumped by the same laser. The authors also used the same setup to demonstrate for the first time a direct measurement of the joint temporal resolution of the created bi-photons [45], which they used to measure the heralded single photon purity.

Photon conversion is also possible using  $\chi^3$  media such as silica. Using a photonic crystal fiber, the conversion of heralded photons at 683 nm to 659 nm with two pulsed pumps at 808 nm and 845 nm was demonstrated [56].

Very recently, the conversion of single photons from a quantum dot from 1310 nm to 710 nm was reported [65]. The single photon character of the converted photons could be shown by measuring a  $g^{(2)}(0)$  of 0.165 which demonstrates strong anti-bunching. The experiment used a ppLN waveguide and a 1550 nm cw pump laser.

Also very recently, the conversion of 795 nm photons to 1376 nm and back to 795 nm in cold rubidium vapour was reported in an experiment combining this conversion with a cold rubidium based quantum memory [64]. Non-classical photon correlations were preserved in the process. In a follow-up experiment the experimental arrangement could even be used to create, store polarization entanglement [21]. Moreover, the entangled photons could be converted to a fiber compatible wavelength at 1376 nm, passed through 100 m telecom fiber and converted back to 795 nm while preserving polarization entanglement.

## 2.2 Principles

### 2.2.1 Photonic entanglement

Since the now famous paper of Einstein, Podolsky and Rosen [24] on the (in their view paradoxical) consequences of the predictions of quantum mechanics for entangled states, entanglement has been the central element not only for fundamental aspects regarding the description of nature. It also became the essential phenomenon for potentially revolutionary quantum technological applications such as quantum computing as well as secure quantum communication. One of the most successfully used physical systems to study entanglement are photons [89]. The reasons for photons being so widely used is the relatively easy manipulation and detection of photonic quantum states, and, even more importantly, their practical immunity to decoherence, with no requirements for cryogenic temperatures nor vacuum conditions. Also, entangled photon states can be generated – with very high quality – using parametric downconversion [47, 25]. Various photonic degrees-of-freedom have been experimentally used so for entanglement generation: path [68], energy-time [12], frequency [66] (also see chapter 4), and orbital angular momentum (OAM) [86]. The most widely used degree-of-freedom, however, is the polarization (or spin) of photons. Polarization – naturally only 2-dimensional with the conventionally used basis states of horizontal  $|H\rangle$  and vertical  $|V\rangle$  linear polarization – offers a number of practical advantages such as the easy universal manipulation and detection with standard polarization optics, e.g. birefringent wave plates and polarization dependent beam splitters, and also various reliable methods of creating polarization entanglement.

Formally, bipartite (polarization-)entanglement of two photons can be defined in a  $2 \times 2$  dimensional Hilbert space ( $\mathcal{H} = \mathcal{H}^A \otimes \mathcal{H}^B$ ) of two qubits  $A$  and  $B$  (states in the 2-dimensional Hilbert spaces  $\mathcal{H}^A$  and  $\mathcal{H}^B$  describing the state of photons  $A$  and  $B$ ) in the following way: A state in this space is entangled if and only if it is **not separable**, i.e. it cannot be written as a tensor product (or convex sum of tensor products for mixed states):

$$\text{separable pure states : } |\psi\rangle = |\psi^A\rangle \otimes |\psi^B\rangle \quad (2.1)$$

$$\text{separable mixed states : } \rho = \sum_j p_j \rho_j^A \otimes \rho_j^B \quad (2.2)$$

$$\text{( with } p_j > 0 \text{ and normalized } \sum_j p_j = 1 \text{ )} \quad (2.3)$$

Clearly, this abstract definition neither gives a straight-forward experimental recipe to detect (verify) entanglement nor shows how to quantify a "degree-of-entanglement". For the last decade, considerable theoretical effort has been invested into the question of characterising entanglement both theoretically and practically in the lab. A recent and detailed review of many results on this topic can be found in [35].

### Bell violation for entanglement verification

One of the most stringent ways to verify the non-separability – and thus entanglement – of a given quantum state relies on the experimental violation of a Bell inequality [8]. In experiments in most cases a more practical form – a Clauser-Horne-Shimony-Holt(CHSH)-type Bell inequality [15] is used. These inequalities have to be fulfilled by any local realistic theory (or local hidden variable theory) and an experimental violation therefore excludes any separable (local) description of the state including a separable quantum mechanical description. Therefore, any violation of a Bell inequality is also a stringent proof for entanglement. Consequently, this has been used in many experiments to conclusively prove the creation of entanglement. However, although any pure bipartite state violates a specifically constructed Bell inequality [31], there is no single inequality that is violated for every entangled state. Moreover, there are certain non-separable mixed states, that do not allow the violation of *any* CHSH-Inequality [87]. Therefore, Bell inequalities, although very useful and one of the most accepted and practically used methods for the verification of entanglement, have to be complemented by more general procedures and concepts to detect and analyse entanglement, e.g. *entanglement witnesses* and *entanglement measures* (summarized for example in [35]).

### Tangle as entanglement measure

One of the entanglement measures used in this thesis beside Bell-violations is the *tangle*, which is related to the *entropy of entanglement*, *entanglement of formation* and *concurrence*. One of the striking characteristics of a bipartite entangled state is that its strong correlations can only exist at the expense of the existence of their local, individual properties – i.e. for maximally entangled states with perfect correlations, the local properties must appear to be fully random. Formalized information theoretically, the corresponding local state has the maximum entropy. This is the underlying motivation for the entanglement measure for pure states called *entropy of entanglement*

$E(\psi)$  based on the von Neumann entropy  $S(\rho)$  of locally reduced states defined by [58]:

$$E(\psi) = S(\rho_A) = -\text{Tr}(\rho_A \log(\rho_A)) \quad (2.4)$$

$$\rho_A = \text{Tr}_B(\psi) \text{ (reduced density matrix of subsystem A)} \quad (2.5)$$

For a maximally entangled state of two qubits it is 1, it is 0 for any product state and lies between 1 and 0 for any non-maximally entangled state. It is essential that  $S(\rho_A) = S(\rho_B)$ , i.e.  $E(\psi)$  is independent of which of the two subsystems is considered, which is necessary to make the entropy of entanglement a valid entanglement measure for pure states. From an operational point of view  $E(\psi)$  gives the ratio of the number  $n$  and  $m$ : of copies  $n$  of maximally entangled states minimally needed to prepare  $m$  copies of the state  $\psi$  using only classical means – i.e. local operations and classical communication (LOCC):  $E(\psi) = \frac{m}{n}$ . Note also that many other entanglement measures for mixed states reduce to the entropy of entanglement if considered for pure states[35].

A straight-forward generalisation of the entropy of entanglement for mixed states is the *entanglement of formation*  $E_F$  [34], which is defined as the minimal combined entropy of entanglement minimized over all possible pure state decompositions of the state  $\rho$ ,  $\rho = \sum_j p_j |\psi_j\rangle\langle\psi_j|$ :

$$E_F(\rho) = \min \sum_j p_j E(\psi) \quad (2.6)$$

Importantly, Hill and Wootters [34] found a closed formula to calculate  $E_F$  for any mixed state of two qubits:

$$E_F(\rho) = h\left(\frac{1}{2} + \frac{1}{2}\sqrt{1 - C(\rho)^2}\right) \quad (2.7)$$

$$h(x) = -x \log(x) - (1 - x) \log(1 - x) \quad (2.8)$$

This formula directly uses two other entanglement measures – the concurrence  $C(\rho)$  and its square, the tangle  $T(\rho) = C(\rho)^2$  which are defined by:

$$T(\rho) = C(\rho)^2 \quad (2.9)$$

$$C(\rho) = \max(0, \lambda_1 - (\lambda_2 + \lambda_3 + \lambda_4)) \quad (2.10)$$

$$\lambda_i = \text{sorted Eigenvalues of } R = \sqrt{\sqrt{\rho} \tilde{\rho} \sqrt{\rho}} \quad (2.11)$$

$$\tilde{\rho} = (\sigma_y \otimes \sigma_y) \rho^* (\sigma_y \otimes \sigma_y) \quad (2.12)$$

The importance of the tangle and reason why it was chosen to be used in this work has to do with two features: firstly, the tangle is significantly more susceptible to any decrease in the quality of the entanglement than other measures, allowing it to more sensitively analyse any entanglement degradation. And secondly, one can show that for a system of three qubits A, B and C the tangle obeys a relation similar to a conserved quantity [16]:

$$T(\rho_{A:B}) + T(\rho_{A:C}) \leq T(\rho_{A:BC}) \quad (2.13)$$

That is, the combined tangle of  $A$  with  $B$  and  $A$  with  $C$  cannot be greater than the tangle between  $A$  and the combined system of  $B$  and  $C$ . Note that this does not hold for  $E_F$  or the concurrence. Interestingly, the discovery of this relation for the tangle was also a starting point for many theoretical investigations into properly defining and quantifying genuine multi-partite entanglement, with the 3-tangle itself being one the first proposed multi-partite entanglement measures and defined by  $T(A : B : C) = T(A : BC) - T(A : B) - T(A : C)$ , originally referred to as *residual entanglement* [16].

### Quantum tomography

Fully determining an unknown quantum state can – in principle – not be achieved by single shot measurements. The easiest way to see this is as a consequence of the no-cloning theorem [88]. Nevertheless, by using many and different measurements, so called quantum state tomography, allows to completely characterise the state of a quantum system, that is, to reconstruct its density matrix [38]. The analysis in this thesis fully builds on the tomographic techniques laid out in detail in [50]. The general method is to take many copies of the quantum state and measure an (over-)complete set of measurements, typically consisting of local measurements and their correlations. In an ideal situation, where one could measure the corresponding probability without any error, one could mathematically directly calculate the given density matrix. However, under realistic conditions, where every measurement is inevitably accompanied by noise (in the case of photons typically Poissonian counting noise), the resulting density matrix will generally not be physical. In this case, one has to estimate the density matrix of the quantum state by using maximum likely-hood methods using numeric optimisation methods. This yields an experimental estimate of the density matrix  $\rho$ . Error margins can than be calculated by using Monte-Carlo techniques based on Poissonian noise models.

There are a number of quantities that can be derived from  $\rho$ : an important one is the fidelity  $F(\rho : \psi)$  with respect to an aimed for target state  $\psi$  defined

by:

$$F(\rho : \psi) = \langle \psi | \rho | \psi \rangle \quad (2.14)$$

with the physical interpretation that given a state with the density matrix  $\rho$  the probability to find  $\psi$  is  $F(\rho : \psi)$ .

Another important quantity is the purity  $P(\rho)$  defined by:

$$P(\rho) = \text{Tr}(\rho^2) \quad (2.15)$$

and ranges from 1 for pure states to  $1/d$  for completely mixed states of dimension  $d$ .

Including also the tangle, these three quantities –  $F$ ,  $P$  and  $T$  – form the standard set of parameters that were calculated in this thesis together with the reconstructed density matrices.

Quantum processes can also be reconstructed with a similar tomographic method. Again, this thesis builds upon the procedures and computer code in detail explained in [50]. For quantum process tomography the aim is to reconstruct a process matrix  $\chi$  that fully characterises the experimental process. For this, for a set of input states the output state of the process is measured for a set of projections. The data then allows to estimate the process matrix, using again the techniques of numerical maximum likelihood methods and Monte Carlo simulation to estimate the error margins. Derived quantities include the process fidelity and purity, that have a similar physical interpretation as the equally named quantities for quantum state tomography.

For all further details and explanations concerning quantum state and process tomography see [50].

### 2.2.2 Parametric processes

Non-linear optics based on second order non-linear crystals has long been used for a plethora of applications, and, in the last decades, became also a vital building block in the field of photonic quantum optics. In general, non-linear optics is based physically on a medium reacting non-linearly to an electromagnetic field – that means that the components of the dielectric polarization  $P_i$  in the medium is a non-linear function of the field and can be approximated by a Taylor expansion:

$$P = \epsilon_0 \chi E + \epsilon_0 \chi^{(2)} E^2 + \epsilon_0 \chi^{(3)} E^3 + \dots \quad (2.16)$$

where  $\chi$  is the linear susceptibility, and  $\chi^{(2)}$  and  $\chi^{(3)}$  the first two higher order non-linearities. The second order non-linearity  $\chi^{(2)}$  is responsible for all three-wave-mixing phenomena, such as sum- and difference frequency generation or optical parametric oscillation. The whole topic of parametric processes is extensively covered in many standard text books – as an example see the relevant chapters in [72].

It is worth mentioning that in general the generation of non-classical states of light is very closely linked to second order non-linear optical processes, with the generation of so called squeezed state with optical parametric oscillators taking a pioneering role in the field of experimental quantum optics. Another second-order nonlinear process, which enables the production of entangled pairs of photons – and therefore of great importance – is spontaneous parametric down-conversion (SPDC) and will be described in the following section.

### Spontaneous parametric down-conversion (SPDC)

This non-linear process – first predicted in 1967 [40] – has gained overwhelming attention in the last two decades, because it enables the relatively easy production of correlated photon pairs. Interestingly, it cannot be derived with the classical nonlinear wave-equations. However, sometimes it is semi-classically interpreted as an optical parametric oscillation seeded by the (spontaneous) fluctuations of the vacuum field.

SPDC can be formally described using the following interaction Hamiltonian for three interacting modes – a pump mode  $p$  and two output modes 1 and 2 :

$$\hat{H}_I \propto \hat{a}_p \hat{a}_1^\dagger \hat{a}_2^\dagger + \hat{a}_p^\dagger \hat{a}_1 \hat{a}_2 \quad (2.17)$$

with the respective creation and annihilation operators  $\hat{a}_i^\dagger$  and  $\hat{a}_i$  for the three modes. Normally, now the pump field is treated classically and assumed to be non-depleted. In the limit of a weak interaction strength (which is typically justified by the low non-linearities involved) one relatively easily derives the resulting state for the down-conversion process:

$$|\psi_{\text{SPDC}}\rangle = |0\rangle|0\rangle + \gamma|1\rangle|1\rangle + \gamma^2|2\rangle|2\rangle + \dots \quad (2.18)$$

For generality, modes 1 and 2 can be treated non-degenerate – i.e. with different optical frequencies, but still fulfilling energy conservation:  $\omega_1 + \omega_2 = \omega_{\text{pump}}$  (In case of degenerate SPDC this state would represent a squeezed state in photon number – only even order photon number states are present). The small parameter  $\gamma$  is proportional to the pump field and also a function of



the non-linear interaction strength. For weak enough interaction strengths and pump fields ( $\gamma \ll 1$ ) all higher order terms can be neglected. Then the detection of a photon in the first mode heralds a single photon Fock state in the second mode, and vice versa. This can also be seen formally by dropping the higher order 2-photon terms of equation 2.18 and projecting on a single photon state in the first mode:

$${}_1\langle 1|(|0\rangle_1|0\rangle_2 + \gamma|1\rangle_1|1\rangle_2) = \gamma|1\rangle \quad (2.19)$$

Such a heralded production of single photon states is for obvious reasons very useful in many photonic quantum experiments and technologies. However, a significant disadvantage of using SPDC plays out, if more than two, but a certain higher number of photons (4 or 6 or more) need to be produced at the same time. Due to the inherent probabilistic character of SPDC the probability for a successful production of such a state scales unfavourably (exponential) with the number of photons to be created. Also, when trying to enhance the production rate by higher pump powers, higher order terms can become non-negligible, creating significant unwanted error terms.

An interesting case, which is rarely covered in the standard literature, is the *full quantum treatment of SPDC* with a single photon input. The full quantum Hamiltonian and the corresponding time evolution operator can be written as

$$\hat{H}_I = \gamma(\hat{a}_{pump}\hat{a}_1^\dagger\hat{a}_2^\dagger + h.c.) \quad (2.20)$$

$$\hat{U}(t) = e^{-i\hat{H}_I t/\hbar} = e^{-\frac{i\gamma t}{\hbar}(\hat{a}_{pump}\hat{a}_1^\dagger\hat{a}_2^\dagger + h.c.)} \quad (2.21)$$

Under this evolution (and without loss) the states  $|100\rangle$  and  $|011\rangle$  form a "closed system" – no states outside the Hilbert-space spanned by those two states can be created from them. This makes the derivation of the evolution of the system rather straight-forward. For an initial state with the pump field in a single photon Fock-state and empty signal and idler modes  $|\psi(0)\rangle = |1\rangle_{pump}|0\rangle_1|0\rangle_2 = |100\rangle$  and the convenient abbreviations  $\hat{a}_{DC}^\dagger = \hat{a}_{pump}\hat{a}_1^\dagger\hat{a}_2^\dagger$ ,  $\hat{a}_{DC} = \hat{a}_{pump}^\dagger\hat{a}_1\hat{a}_2$  and  $\frac{\gamma}{\hbar} = \Omega$  the state evolution is:

$$|\psi(t)\rangle = U(t)|\psi(0)\rangle = e^{-i\Omega t(\hat{a}_{DC}^\dagger + \hat{a}_{DC})}|100\rangle \quad (2.22)$$

$$|\psi(t)\rangle = \sum_{k=0}^{\infty} \frac{(-i\Omega t)^k}{k!} (\hat{a}_{DC}^\dagger + \hat{a}_{DC})^k |100\rangle \quad (2.23)$$

For each  $k$  in the sum there is always only one term in  $(\hat{a}_{DC}^\dagger + \hat{a}_{DC})^k |100\rangle$  that is non-zero, namely for even  $k$ :  $(\hat{a}_{DC} \hat{a}_{DC}^\dagger)^{k/2} |100\rangle = |100\rangle$  and for odd  $k$ :  $\hat{a}_{DC}^\dagger (\hat{a}_{DC} \hat{a}_{DC}^\dagger)^{(k-1)/2} |100\rangle = |011\rangle$ , yielding (after separating the sum for even and odd  $k$  and shifting the indices of the two sums accordingly):

$$|\psi(t)\rangle = \sum_{k=0}^{\infty} (-1)^k \frac{(\Omega t)^{2k}}{(2k)!} |100\rangle + i \sum_{k=0}^{\infty} (-1)^k \frac{(\Omega t)^{2k+1}}{(2k+1)!} |100\rangle \quad (2.24)$$

The first and second sum are just  $\sin()$  and  $\cos()$ , so that in the end the time evolution is:

$$|\psi(t)\rangle = \cos \Omega t |100\rangle - i \sin \Omega t |011\rangle \quad (2.25)$$

Note that this derivation is mathematically analogous to a two level atomic system driven by a resonant, coherent laser field giving rise to Rabi-oscillations, i.e. periodic oscillations in the probabilities for the two states.

There are several interesting points about these results. First, down-conversion can in principle be 100% efficient if one starts with a single photon Fock-State as the pump. The condition for this is  $\Omega t = \pi/2$  (or an odd multiple of  $\pi$ ). In practice, however, typically there are much lower efficiencies for non-linear crystals:  $\Omega t$  is determined by the crystal length and the effective non-linear coefficient  $d_{\text{eff}}$  and the highest reported values are for ppLN wave-guides with  $\Omega t$  in the order of  $10^{-3}$  yielding an efficiency of downconversion in the order of  $10^{-6}$  [37]. It is also worth noting that, starting with a state  $|011\rangle$ , for  $\Omega t = \pi$  a phase shift of  $\pi$  is acquired, which can be used to implement a deterministic entangling gate (see chapter 3). A possible way to significantly increase the achievable strength  $\Omega t$  of the parametric process is to use a pumped third order non-linearity. For more details see chapter 3 on higher order photonic conversion.

## Sum Frequency Generation and SPUC

Sum frequency generation (SFG) is a second order non-linear process describing the interaction of two electro-magnetic fields ( $\omega_1$  and  $\omega_p$ ) generating a third field, whose frequency is the sum of both of these fields:  $\omega_1 + \omega_p = \omega_2$ . This process is well known since decades, but has gained relevance in experiments with single photons only in the past few years. When a single photon is in the input mode, then this photon can be upconverted to the sum of its frequency and the pump frequency by SFG: single photon upconversion (SPUC).

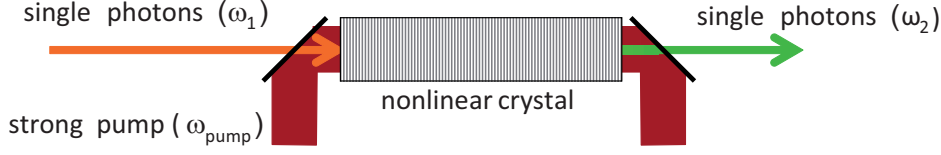


**Figure 2.1:** Basic principle of SPUC based on the nonlinear process of sum frequency generation (SFG): a pump and an input field are combined in a nonlinear medium (typically a crystal) generating an output field with the sum of the input frequencies:  $\omega_2 = \omega_1 + \omega_p$

The efficiency of the sum frequency conversion process is governed by the following coupled wave equations (derived for example in chapter 21.4. Saleh Teich):

$$\frac{dE_1}{dz} = i \frac{\omega_1 d_{\text{eff}}}{n_1 c} E_2 E_p^* e^{i\Delta k z} \quad (2.26)$$

$$\frac{dE_p}{dz} = i \frac{\omega_p d_{\text{eff}}}{n_p c} E_1 E_2^* e^{i\Delta k z} \quad (2.27)$$

$$\frac{dE_2}{dz} = i \frac{\omega_2 d_{\text{eff}}}{n_2 c} E_1 E_p e^{i\Delta k z} \quad (2.28)$$

where the  $E_i$ 's are the electric fields with corresponding frequencies  $\omega_i$  and indices of refraction  $n_i$  and  $d_{\text{eff}}$  the effective non-linear coefficient,  $c$  the speed of light and  $z$  the distance in the propagation direction. For perfect phase-matching the phase mismatch  $\Delta k$  is zero and also approximating the pump field to be non-depleted ( $\frac{dE_p}{dz} = 0$ ) and real valued, the starting condition  $E_2(0) = 0$  leads to the reduced equations:

$$\frac{dE_1}{dz} = i \frac{\omega_1 d_{\text{eff}}}{n_1 c} E_2 E_p \quad (2.29)$$

$$\frac{dE_2}{dz} = i \frac{\omega_2 d_{\text{eff}}}{n_2 c} E_1 E_p \quad (2.30)$$

which leads to:

$$\frac{d^2 E_1}{dz^2} = - \frac{\omega_1 \omega_2 d_{\text{eff}}^2}{n_1 n_2 c^2} E_p^2 E_2 \quad (2.31)$$

and yields the solution:

$$E_1(z) = E_1(0) \cos \sqrt{\frac{\omega_1 \omega_2 d_{\text{eff}}^2}{n_1 n_2 c^2} E_p^2} z \quad (2.32)$$

From this follows the upconversion efficiency  $\eta$  (normalized to photon number and using photon number conservation of the SFG process):

$$\eta = \sin^2 \sqrt{\frac{\omega_1 \omega_2 d_{\text{eff}}^2}{n_1 n_2 c^2} E_p^2 L} \quad (2.33)$$

Note that this efficiency calculation is also valid for single photon input, i.e. for SPUC, although a classical formalism is used. This is because the corresponding full quantum derivation turns out to yield fully equivalent results. The final formula, however, only represents a simplified model in the sense that plain waves are assumed. To accurately predict experimental conversion efficiencies one has to consider the parametric interaction of focussed Gaussian beams. Following [10, 3] and introducing an efficiency reduction factor  $h_m$  (that is close to 1 for optimum focussing conditions), one arrives at the final efficiency relation:

$$\eta = \sin^2(\pi/2 \sqrt{P_p/P_{\text{max}}}) \quad (2.34)$$

$$P_{\text{max}} = \frac{c \epsilon_0 n_1 n_2 \lambda_1 \lambda_2 \lambda_p}{128 d_{\text{eff}}^2 L h_m} \quad (2.35)$$

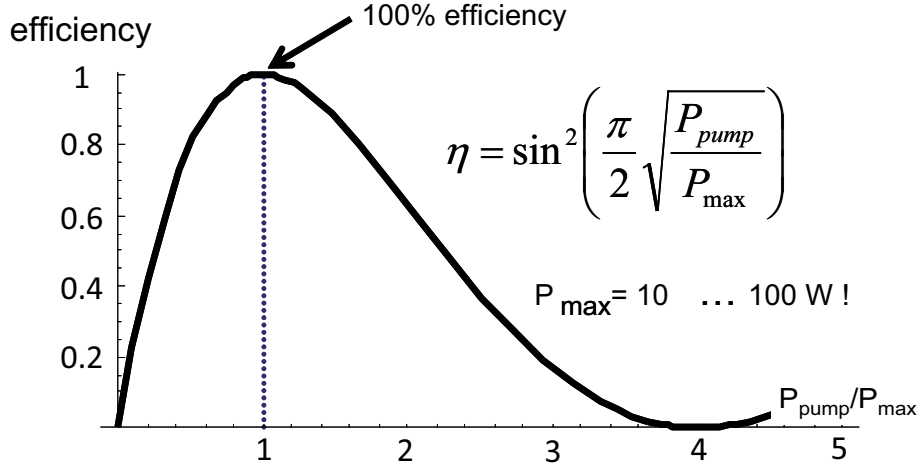


**Figure 2.2:** Plot of the upconversion efficiency as a function of the pump power. At a pump power of  $P = P_{\text{max}}$  100% efficient upconversion is predicted. For typical crystals and crystal length  $P_{\text{max}}$  is on the order of 10 to 100 W.

What is remarkable is that in principle single photons can be converted with unity efficiency from one wavelength to another. However, quite high pump

powers are necessary to achieve this operation point. This problem has been shown to be solvable in practice by various techniques: using high peak power pump lasers or enhancing the pump power by build-up cavities, as well as using highly nonlinear wave-guides instead of bulk crystals for the conversion. For more details see the previous section on state-of-the art photon conversion experiments.

### 2.2.3 Quasi-phase-matching

For all parametric processes not only energy conservation ( $\Delta\omega = \sum \omega_{\text{input}} - \sum \omega_{\text{generated}} = 0$ ) but also so called phase-matching has to be fulfilled to achieve high efficiencies. Phase-matching for example for parametric down-conversion and parametric upconversion imposes a restriction on the wave-vectors of the fields:

$$\text{SPDC} : \vec{k}_{\text{pump}} = \vec{k}_1 + \vec{k}_2 \quad (2.36)$$

$$\text{SPUC} : \vec{k}_1 + \vec{k}_{\text{pump}} = \vec{k}_2 \quad (2.37)$$

This can be seen as a form of momentum conservation from the viewpoint of single photons, when the momentum  $\vec{p}$  of a single photon is connected to the  $\vec{k}$ -vector by  $\vec{p} = \hbar\vec{k}$ . Another way to interpret phase-matching is to consider the case when phase-matching is not fulfilled. In this case the generated fields at different points of time would destructively interfere after a critical propagation length  $L_c$ . For a phase-matched interaction, all generated fields are "in phase", therefore the name of this condition. One can write the phase-matching condition in a very compact form as:

$$\Delta\vec{k} = \sum \vec{k}_{\text{input}} - \sum \vec{k}_{\text{generated}} = 0 \quad (2.38)$$

In vacuum, energy conservation would automatically lead to phase-matching, because of the linear (dispersion) relation between  $\omega$  and  $k$ :

$$k(\omega) = \frac{\omega}{c_0} \quad (2.39)$$

with  $c_0$  being the vacuum speed of light. However, in non-linear media – which in applications are typically non-linear crystals – energy conservation of the interacting field does in general not automatically lead to phase-matching

because of dispersion, i.e. the index of refraction depends on  $\omega$ , and  $c_0$  is replaced by  $c_0/n(\omega)$  which results in a nonlinear dispersion relation for  $k(\omega)$ .

$$k(\omega) = \frac{n(\omega)\omega}{c_0} = \frac{2\pi n(\lambda)}{\lambda} \quad (2.40)$$

There are different phase-matching techniques for bulk non-linear crystals. One widely used example is birefringent phase-matching with angle tuning. In this method the different refractive indices of the ordinary and extraordinary polarizations in birefringent crystals are used to achieve  $\Delta k = 0$ . This and other phase-matching techniques are comprehensively summarized for example in [70, 72].

A more recent development is quasi-phase-matching (QPM). A thorough introduction into quasi-phase-matching can be found in [70, 72]. The basic idea of this method is to periodically reverse the sign of the non-linear coefficient ( $d \rightarrow -d$ ) exactly after the interacting waves have acquired a phase-difference of  $\pi$ , which is after the critical interaction length  $L_c$ . Then the generated field will not destructively interfere with itself, but steadily build up over the propagation through the crystal. This build up is not as efficient as perfect phase-matching would allow, with an effective reduction of the nonlinear coefficient of  $d_{\text{QPM}} = \frac{2}{\pi}d$  leading to a reduction in efficiency of  $(\frac{2}{\pi})^2 \approx 40\%$ . Nevertheless, it is a big advantage of being able to flexibly design the phase-matching for all desired wavelength combinations allowed by the absorption properties of the used crystal. Therefore, QPM is one of the most important phase-matching techniques used today.

Although already proposed very early in the 60s [5] quasi-phase-matching has become technologically feasible and commercially available only in the last decade due to the typically very short critical lengths  $L_c$  on the order of a few to a few of tens of  $\mu\text{m}$ 's. This requirement could be realized technically by lithographically patterned electrodes on the crystal that with a strong electric field can permanently reverse the spontaneous polarisation direction of electro-optic crystals like lithium-niobate ( $\text{LiNbO}_3$ ) or potassium-titanyl-phosphate (KTP). The whole procedure is called periodic poling.

The main formula to calculate the necessary poling period is:

$$L_c = \left| \frac{\pi}{\Delta k} \right| \quad (2.41)$$

where  $\Delta k$  can be calculated from the dispersion  $n(\lambda)$  given by the correspond-

ing Sellmeier equations for the crystal:

$$\Delta k = \sum_{\lambda_{\text{input}}} \frac{2\pi n(\lambda)}{\lambda} - \sum_{\lambda_{\text{generated}}} \frac{2\pi n(\lambda)}{\lambda} \quad (2.42)$$

The relative efficiency  $I_{\text{rel}}$  of the parametric process in a crystal of length  $L$  with a certain poling period can then be calculated for example for varying wavelength and temperatures with:

$$I_{\text{rel}} = I_0 \text{sinc}(\Delta k L / 2)^2 \quad (2.43)$$

with

$$\Delta k = \sum_{\lambda_{\text{input}}} \frac{2\pi n(\lambda)}{\lambda} - \sum_{\lambda_{\text{generated}}} \frac{2\pi n(\lambda)}{\lambda} - \frac{2\pi}{L_c}. \quad (2.44)$$

This general equation together with the dispersion and thermal properties of the medium allows to easily calculate wavelength and temperature bandwidths for the desired quasi-phase-matched parametric processes for the specific crystals and crystal lengths that are used in the experiment.

## 2.3 Setup

In this section, the main experimental techniques and building blocks of the setup are explained in detail. It will point out the key challenges and how future implantations could be further improved.

### 2.3.1 Entangled photon source

Creating entangled photon pairs with spontaneous parametric downconversion (SPDC) tremendously advanced in the last decades. The ability to build continuous wave (cw) pumped, high brightness sources with very high degrees of entanglement is also the basis for the experiments being part of this thesis. The entangled photon source [25] used in the later described experiments is based on SPDC in ppKTP (periodically poled potassium titanyl phosphate). The crystal was quasi phase-matched for collinear type II generation of photon pairs at 810 nm with a pump laser at 405 nm. The entanglement of the created photon pairs is achieved by using a Sagnac-type configuration, in which the down conversion crystal is pumped bi-directionally. The details of the experimental arrangement are described in figure 2.3.

Beside the ease of alignment of this type of source due to the collinear beam paths of the pump laser and the down-conversion photon pairs, this type of source has several advantages, compared to other types of entangled photon sources such as BBO based "crossed ring" sources [47] or crossed crystal sources [48]:

- Long crystals can be used, therefore increasing the brightness and decreasing the bandwidth of the created photon pairs.
- Temporal walk-off effects are intrinsically auto-compensated by the Sagnac-design: the beam paths are automatically the same for the clock-wise and anti-clockwise arm for the ordinary, as well as the extra-ordinary beam. Note that due to the dual-wavelength HWP the ordinary downconversion photons are always sorted into arm 1 and vice versa the extra-ordinary into arm 2.
- Due to the design of the source the central wavelengths of the down-conversion photons can be continuously tuned away from degeneracy, by changing the temperature and thereby the phase-matching conditions of the ppKTP crystal. The very high degree of entanglement can be maintained up to a point (about 830 nm and 791 nm central wavelengths), where the polarization properties of the components – the



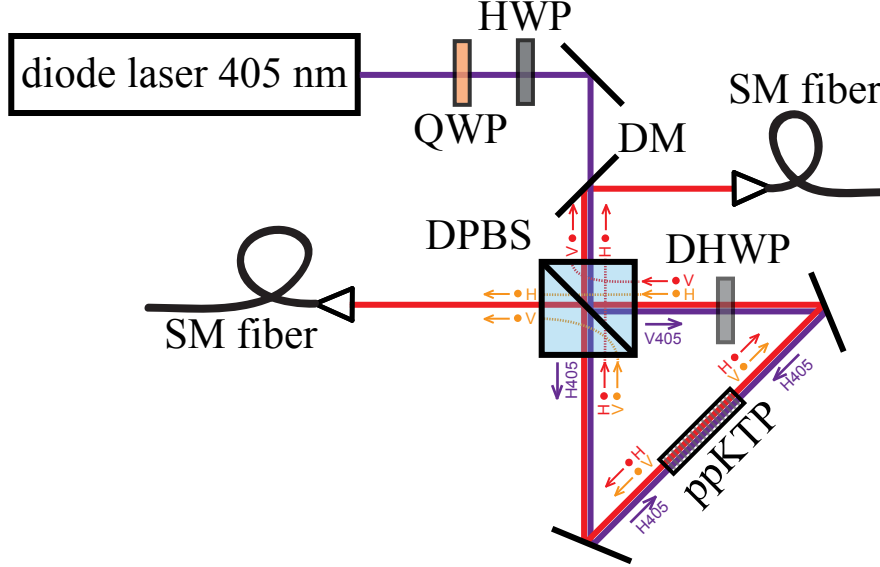


**Figure 2.3:** Scheme of the entangled photon source. A 405 nm laser beam is focused into a 10 mm ppKTP crystal inside a polarization Sagnac-loop. The dual-wavelength (405 and 810 nm) polarization beam splitter (DPBS), splits the pump beam into clockwise and anti-clockwise directions through the loop. The dual-wavelength half-wave plate (DHWP) rotates the polarization of the pump beam such that it is horizontally polarized when it enters the crystal from both sides. The crystal is quasi-phase-matched for type II spontaneous parametric down-conversion creating photon pairs around 810 nm with horizontal (H) polarisation for the first and vertical (V) for the second photon. After the polarizations of the photons are swapped by the DHWP in the anti-clockwise arm, it is overlapped again with clockwise arm on the DPBS. Its two output ports are coupled into to single mode fibers (SM fibers) by appropriate optics and opto-mechanics. A dichroic mirror (DM) separates the downconversion photons from the pump beam. Depending on the pump polarization and the internal phase of the Sagnac loop a two-photon polarization state of the form  $\alpha|HV\rangle + e^{i\phi}\beta|HV\rangle$  is produced. A Half-wave and quarter wave plate control the polarization of the pump beam - and can fully control the state that is created.

dual wavelength polarization beam splitter (DPBS) and the dual wavelength half-wave plate (DHWP) – are too far away from their design wavelengths, which leads to imperfect characteristics (extinction ratio of DWPS is decreased and the retardation of the DHWP is not precisely  $\lambda/2$  any more).

- The same crystal in both the clockwise and anti-clockwise path creates the photon pairs. This eliminates any possible sources of distinguishability of the photons due to the crystal properties compared to sources, where two crystals need to be used.

The entangled photon source was originally built up for long-distance, free-space quantum experiments [25, 26]. Since then, several further improvements on the source have been incorporated: A new pump laser (iWave, Toptica) with up to 50 mW of power was integrated into the source. A new lens system also improved the coupling ratio of the source. This led to a detected rate of around 280.000 pairs/s at 5 mW of nominal pump power (measured 4.3 mW after the Faraday isolator). The ratio between detected coincidences and singles was about 26% for both arms (see figure 2.5). With these numbers the calculated SPDC efficiency of created pairs is around  $5 \times 10^{-10}$  per 405 nm pump photon. Estimated for the full pump power of the laser this results in a detectable pair rate of 2.8 million pairs/s (corresponding to  $> 40$  million created pairs/s). Typical values for the fidelities of the entangled states produced by the source are around 98% to 99%. This high performance source was first used in another long-distance, free-space quantum experiments on the canary islands [74] before it was employed in the different experiments, that are part of this thesis.

In future experiments the following possible design improvements are planned:

- Using a combination of a QWP at  $45^\circ$ , a HWP, another QWP at  $45^\circ$  and another HWP (with each HWP in a high precision or even automated rotation mounts) should enhance the sensitivity of aligning the pump polarization and corresponding entangled state. Currently, the use of only a QWP and a HWP requires "walking" the waveplates to find the optimal setting. This walking would be made obsolete, because with the combination of the four waveplates, the degrees of freedom for the pump polarization state are ideally decoupled and the first HWP only controls the phase between H and V polarization of the pump and the second only the ratio.
- Switching to a dichroic mirror that is high reflective for 405 nm and high transmissive for 810 nm instead of the other way around would

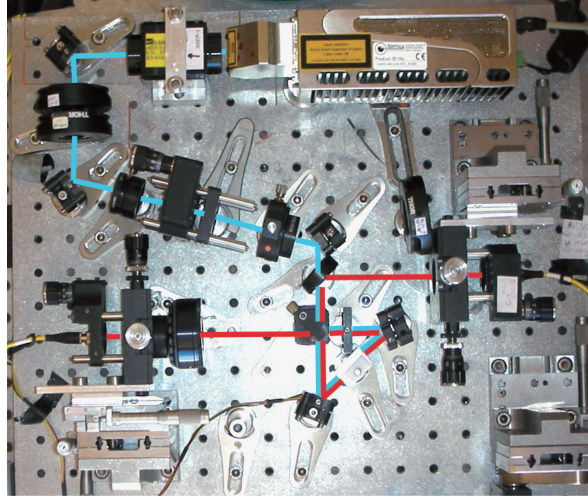


**Figure 2.4:** Photograph of the experimental setup of the described source. The paths of the pump laser and the downconversion photons are shown as coloured lines. It can be seen that the source is very compact fitting on a bread board of only  $500 \times 500$  mm.

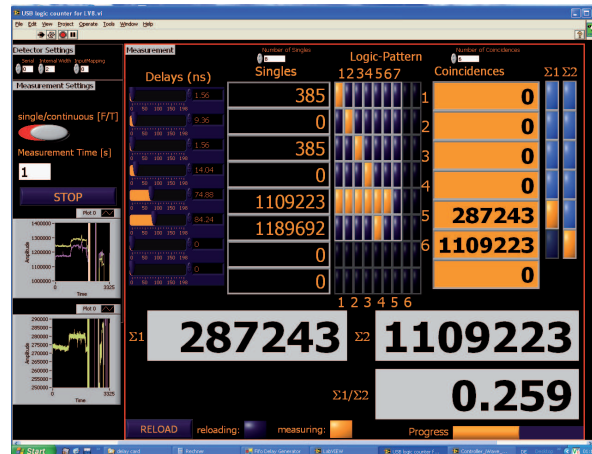


**Figure 2.5:** Screen-shot of the recorded singles and pairs rates. The two big numbers on the bottom represent the coincidence rate (left) and the singles rate of arm 1 (right) in counts per second. Also the ratio between those numbers is shown which gives the arm coupling efficiency (lower right).

give more space in the beam path of arm 2 and also make arm 1 and 2 more geometrically symmetric.

- The translation stages for the single mode couplers are on the edge of their sensitivity when aligning the source for maximum coincidences. Using more sensitive flexure stages can solve this problem.
- A crucial alignment procedure of the source involves the alignment of the mirrors inside the Sagnac loop. More sensitive and easier reachable Sagnac mirror mounts and an additional translation degree of freedom for one of the Sagnac mirrors can greatly improve the control. Currently this has been already implemented for another experiment in progress at the moment.

### 2.3.2 Optimal focussing for SPUC

In order to achieve the highest conversion efficiency in the upconversion process, one has to choose optimal focussing conditions inside the crystal for the pump and the single photon beam. For SHG optimal focussing conditions are well known for a long time [10]. This theory calculations by Boyd and Kleinman describe the parametric interaction of focussed Gaussian beams. In their final formula the efficiency is proportional to the so called efficiency reduction factor  $h_m$  which is dependent on the focussing parameters of the interacting beams. A useful parametrisation for the focussing of a Gaussian beam is the focussing parameter  $\xi = \frac{L}{2z_0}$ , where  $z_0$  represents the Rayleigh range of the focussed beam connected to the focus waist  $w_0$  by  $z_0 = \frac{\pi w_0^2}{\lambda}$  [72].

The analytical treatment in [10] gives the result, that an optimal  $h_m$  is achieved for a focus parameter of the interacting beams of  $\xi \approx 2.84$  with a value of  $h_m$  slightly above 1. However, the derivation in [10] is strictly true only for SHG. For a SFG interaction of fields with different wavelengths  $\lambda_1$  and  $\lambda_2$  a more detailed treatment can be found in [33]. Nevertheless, in the case of no walk-off the calculation yields the same number for the theoretically optimum focus parameter  $\xi_1(\text{for } \lambda_1) = \xi_2(\text{for } \lambda_2) \approx 2.84$  for both input beams, with an only marginally reduced  $h_m$  compared to the SHG case.

We performed a characterisation experiment [69] to verify this theoretic prediction for our situation. Two laser beams – a strong pump beam tunable between 1520 nm and 1570 nm at powers up to 1 W and a weak probe beam at 810 nm – were focussed with different focussing parameters into a 25 mm

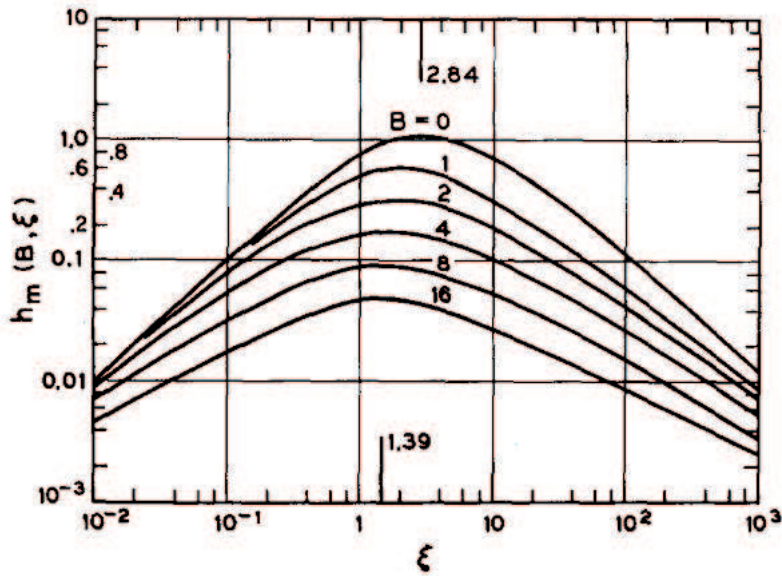


**Figure 2.6:** Plot of the efficiency reduction factor  $h_m$  vs. the focussing parameter  $\xi = \frac{L}{2z_0}$  (from [72]). The highest value - and therefore the highest efficiency - can be reached at  $\xi \approx 2.84$ . Curves are shown for different  $B$  which is a parameter characterizing double refraction in the crystal: For  $B \neq 0$  would lead to lateral walk-off. It can be also seen that the region of nearly optimal efficiency is rather insensitive on the focussing conditions: e.g. for  $B=0$  for a region between  $1.5 \leq \xi \leq 5.3$   $h_m$  is within 10% of the maximum value.

long ppKTP crystal, that was quasi-phase-matched for sum frequency generation of the two wavelengths converting 810 nm to 532 nm. For the different focussing parameters the efficiency of the conversion process was measured. The result is plotted in figure 2.7 and is in satisfactory agreement with the theoretical prediction.

### 2.3.3 Setup for polarization coherent upconversion

This section describes the central experimental setup that was used to polarization coherently convert single photons from 810 nm to 532 nm and conserves polarization entanglement between the input (output) photon to another spatially separated photon. The input source of polarization entangled photons described before was connected via polarization controlled single mode fibers to the input of the upconversion setup. Also the pump laser was fiber coupled and could therefore be easily connected to the pump input of the setup.

Because the parametric interaction in typical non-linear crystals allows SFG only for one specific polarization combination for the input beams, one basic strategy to up-convert single photons in a polarization preserving way is to convert each - horizontal and vertical - polarization individually. Than to combine them coherently and in such a way, that it becomes indistinguishable which polarization was converted. This can be achieved for example with various interferometer based designs, where in each path one of the polarizations is converted. These interferometers could be based on Michelson, Mach-Zehnder or Sagnac-type configurations (see for example [1]). The most simple geometry however, is to use two crossed crystals directly next to each other, where the first crystal converts horizontal and the second vertical polarization. A setup realizing this design was build up for this experiment. The experimental configuration is shown in detail in figure 2.8.

The SFG process takes place in two crossed ppKTP crystals with lengths of 4.3 mm that were triple anti-reflection coated for 532, 810 and 1550 nm and phase-matched by periodic poling for SFG of this wavelength combination. The pump laser system consists of a fiber-coupled tunable external cavity diode laser (New Focus 6427) – tunable from 1520 to 1570 nm – which is amplified from 4 mW to up to 1 W with an erbium-doped fiber amplifier (EDFA) (Pritel FA-30). For setting the polarization of the pump beam a fiber polarization controller (bat ears) was used. To align and characterize the setup an (attenuated) self-build grating stabilized external cavity diode laser at 810 nm was used. The pump and input beams were combined with a

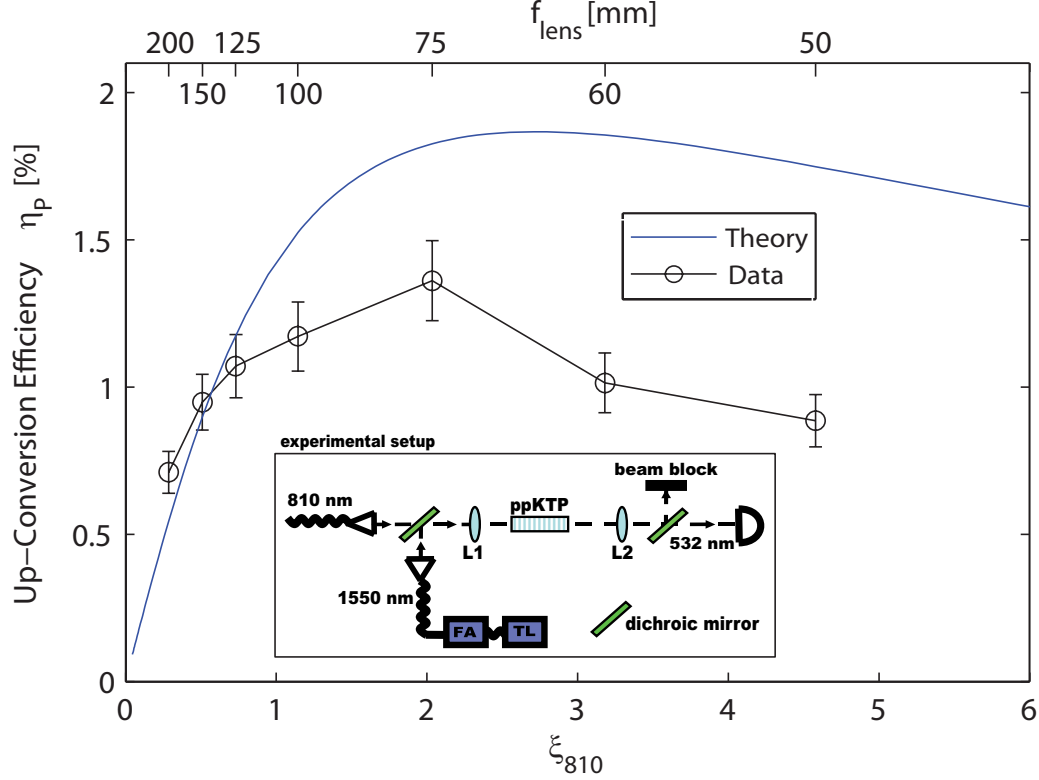


**Figure 2.7:** Plot of the measured upconversion efficiency vs. focussing parameter (from [69]). The inset shows the setup that was used for this characterization measurement. The pump beam at 1550 nm coming from an tunable laser (TL) and is amplified by an erbium doped fiber amplifier (FA) and overlapped with the probe beam at 810 nm with a dichroic mirror. They are focussed into the crystal by various lenses (L1) with different focal lengths (50 mm - 200 mm). The resulting intensity at 532 nm (after removing any pump and probe light with another dichroic mirror) is then measured for each lens and from that the photon conversion efficiency is calculated. The satisfactory agreement between the theoretic prediction and measurement can be extended by attributing the consistently lower absolute efficiency to a slightly lower effective non-linear coefficient of the ppKTP crystal ( $d_{eff}=9.5$  pm/V instead of that derived from the literature value of 11.1 pm/V [77]).

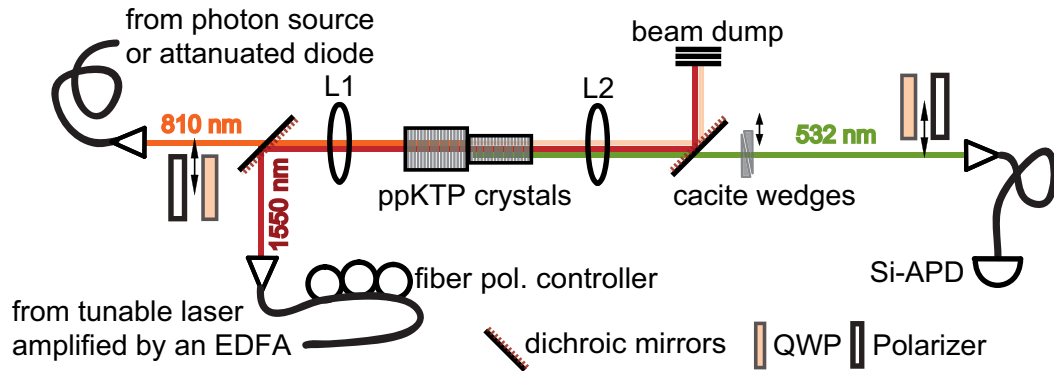


**Figure 2.8:** Scheme of the polarization coherent upconversion setup. The input photons at 810 nm either from the entangled photon source or from an attenuated diode laser are connected to the setup via a single mode fiber. The same way the pump laser light (from a tunable laser amplified by an erbium doped fiber amplifier) is connected to the setup. Both beams are combined with a dichroic mirror. A lens (L1) with focal length of 50 mm focusses both beams into the two ppKTP crystals. After that a second lens (L2) re-collimates the beam and the input and pump beams are separated from the up-converted photons (532 nm) with a dichroic mirror. Calcite wedges compensate the temporal walk-off. For detection the 532 nm photons are coupled into a single mode fiber that is connected to a silicon based avalanche photo-diode (Si-APD). For each - polarization preparation and analysis - a quarter wave plate (QWP) and a polarizers can be placed into the beam paths. The polarization of the pump is adjusted with a fiber polarization controller.



dichroic mirror, coated for high reflection at 1550 nm and high transmission at 810 nm. A plano-convex lens with a focal length of 50 mm was used to focus both beams into the two ppKTP crystal. This lens was not achromatic. To compensate this so that the spot positions in the direction of the beam propagation were the same, the divergence of the 1550 nm beam could be aligned with an adjustable collimation lens in the fiber out-coupling optics. After the crystals another plano-convex lens ( $f = 50$  mm) anti-reflection coated for 532 nm was used to re-collimate the 810, 1550 and the created 532 beam. A dichroic mirror then separated most of the 810 and 1550 nm light from the 532, and the 532 with then further cleaned up by being reflected 6 times on two high reflective mirrors for 532, that had high transmissions for the other wavelengths. For single photon detection the light was then coupled into single mode fiber with 30-50% efficiency. Note that this single mode coupling also has a mode cleaning effect, that later on enhances the fidelities of the polarization of the up-converted photons. In order to measure the polarization properties of the upconversion process suitable waveplates and polarizers can be inserted into the respective beam paths.

The collimated beam size and the focal length of 50 mm of the lens gave a focusing parameter of  $\xi \approx 0.8$  for both beams leading to an efficiency reduction factor of  $h_m \approx 0.6$  (see 2.3.2). With these numbers and using the equation (from chapter principles)

$$\eta = \sin^2(\pi/2\sqrt{P_p/P_{max}}) \quad (2.45)$$

$$P_{max} = \frac{c\epsilon_0 n_1 n_2 \lambda_1 \lambda_2 \lambda_p}{128 d_{eff}^2 L h_m} \quad (2.46)$$

with the full pump power of 1000 mW and only using one crystal a maximum efficiency of around 0.8% can be expected. Experimentally this intrinsic efficiency could be verified with good agreement in a measurement where 28 W of 810 nm was converted to 270 nW of 532 nm. Taking into account the energy ratio of the output and input photons of  $810/532 \approx 1.5$  and the additional loss introduced by optical components of around 18% this results in an efficiency of around 0.6%. The discrepancy the expected efficiency could be explained by a slightly lower effective non-linear coefficient for the ppKTP crystals than that calculated from literature value of 11.1 pm/V [77].

Another important issue is the chromatic and polarization dependent temporal walk-off between an up-converted 532 photon at horizontal and vertical polarization. The reason for that are the different group-velocities for 810 and 532 and their different polarizations. This is illustrated in figure 2.9. From the different group delays in KTP it can be calculated that for the two

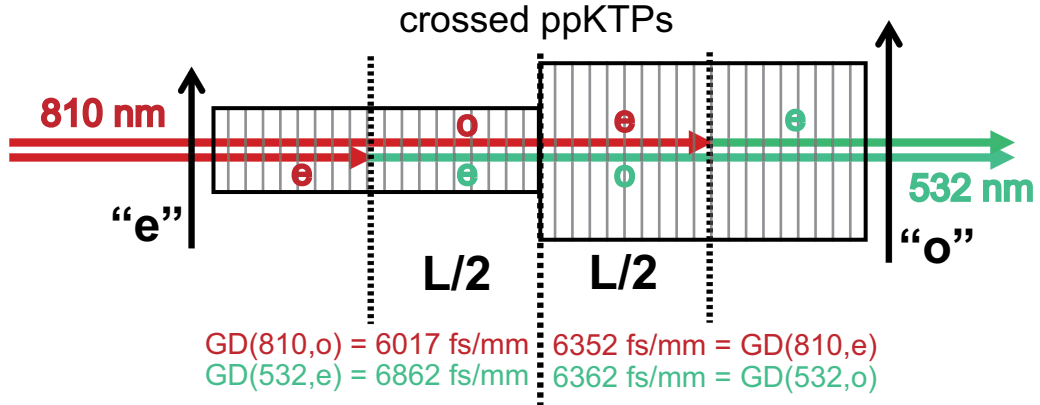


**Figure 2.9:** Illustration of the temporal walk-off between H and V polarized 532 nm photons in the two crossed ppKTP crystals of length  $L$ . The temporal walk-offs (group delays - GD) for the different wavelengths and polarizations are: 532 nm (ordinary) - 6362 fs/mm, 532 nm (extraordinary) - 6862 fs/mm, 810 nm (ordinary) - 6017 fs/mm, 810 (extraordinary) - 6352 fs/mm. There are two contributions to the walk-off - from the first crystal  $GD(532,e)-GD(810,o)$  and the second crystal  $GD(532,o)-GD(810,e)$  leading in total to 1.8 ps for the two 4.3 mm long crystals.

4.3 mm crystals a temporal walk-off of around 1.8 ps can be expected (see figure 2.9). This is in the same order of magnitude than the coherence length of the up-converted 810 nm photons of around 3 ps and would significantly effect the fidelity of the polarization coherence if uncompensated. To compensate the walk-off two wedges of calcite with a joined thickness of around 3 mm were used. The small wedge angle of  $0.5^\circ$  conveniently allows the fine-tuning of the introduced temporal walk-off. Calcite when cut orthogonal to the optical axis introduces a temporal walk-off of 629 fs/mm at 532 nm.

## 2.4 Results

### 2.4.1 Efficiency and background

The conversion efficiency for interacting Gaussian beams is given theoretically by :

$$\eta = \sin^2(\pi/2\sqrt{P_p/P_{max}}),$$

$$P_{max} = \frac{c\epsilon_0 n_1 n_2 \lambda_1 \lambda_2 \lambda_p}{128 d_{\text{eff}}^2 L h_m}, \quad (2.47)$$

where  $P_p$  is the power of the pump beam,  $\lambda_{1,2}$  the wavelength of the input and output,  $n_{1,2}$  the corresponding indices of refraction in the crystal,  $d_{\text{eff}}$  the effective nonlinearity,  $L$  the crystal length and  $h_m$  focussing factor for Gaussian beams. The spot sizes of  $\sim 70 \mu\text{m}$  (1550) and  $\sim 50 \mu\text{m}$  (810) corresponding to a focussing parameter  $\xi = \frac{L}{2z_R}$  (with Rayleigh length  $z_R$ ) of about 0.8 for both beams leads to  $h_m \sim 0.6$ .

For the maximally available pump power of 1 W and a single 4.3 mm long crystal an efficiency of  $\sim 0.8\%$  can be theoretically expected. Experimentally, we measured 270 nW of 532 nm light converted from an input of 28  $\mu\text{W}$  at 810 nm. Accounting for the wavelength difference and factoring out loss of 16% introduced by optical components, this implies an observed upconversion efficiency of  $\sim 0.6\%$ . We attribute the discrepancy to the theoretically expected efficiency to a slightly lower effective non-linear coefficient than that calculated from KTP data of 11.1 pm/V due to imperfect periodic poling.

For polarization-coherent operation this efficiency is further decreased by 50% as only half the pump power is available for each crystal, while focussing into the middle between the two crystals (end facet of each crystal) decreases it by another 82%. Adding also in the SM fiber coupling losses of 50%, this accounts for the finally, directly measured efficiency with entangled photon input of around 0.02%, which corresponds to an intrinsic conversion efficiency – directly after the crystals – of about 0.04%.

In contrast to most other single photon upconversion, no pump induced dark-counts could be observed. Similarly to what has been suggested before, we attribute this to our pump configuration with the pump wavelength being much longer than the input and output single photon wavelengths. In this way, Raman scattering from the pump wavelength into the input (or even output) wavelength is strongly suppressed, because their energies lie on the anti-Stokes side. Moreover, there have been no experiments on single photon conversion with ppKTP so far, so it is not clear if there would have been

Raman induced background counts even with a pump at a higher energy than the input wavelength. In fact, this would be an interesting question to be addressed in follow-up experiments.

## 2.4.2 Polarization coherent SPUC

In this subsection the results of the different kinds of measurements are presented that were carried out to determine how well the polarization of single up-converted photons (and their polarization entanglement to another photon) is conserved. The experimental data and results are shown and include: polarization fringes, process tomography measurements, state tomographies of the entangled states before and after the conversion as well as Bell violation measurements with the converted entangled state. The setup that was used for these measurements is in detail described in the previous section.

### Polarization fringes

The first and most straightforward approach to characterize the performance of the polarization coherent upconversion setup is to measure polarization fringes with horizontal, vertical,  $+45^\circ$  and  $-45^\circ$  linear polarization input states. The input here was an attenuated diode laser at 810 nm. With a polarizer and a half-wave (HWP) the different input states could be prepared with very high fidelity. The rate of output photons at 532 nm was then measured after being sent through an rotatable polarizer to project onto a range of linear polarization states. The outcome of this measurement can be seen in figure 2.10 and shows very high quality polarization fringes. Fits to the measured data with sinusoidal functions were carried out yielding the following visibilities for the 4 curves: H –  $99.2\% \pm 0.2\%$ , V –  $99.2\% \pm 0.2\%$ , D –  $98.7\% \pm 0.3\%$ , A –  $99.0\% \pm 0.2\%$  – totalling to an average visibility of  $99.0\% \pm 0.1\%$ . The visibility is defined as  $\frac{Maximum-Minimum}{Maximum+Minimum}$ . Slight wedging and retardation errors of the wave-plates, minimal misalignment of the axis of the ppKTP crystals and stray light are the most probable reasons for the residual deviations from a 100% visibility.

### Quantum process tomography

Extending the setup with 2 quarter-wave plates - one for the input state preparation at 810 nm and one for the out put analysis at 532 nm - allows to also access left-hand (L) and right-hand (R) circular polarization. The count rates for all combinations of input and output polarizations of the set (H, V,

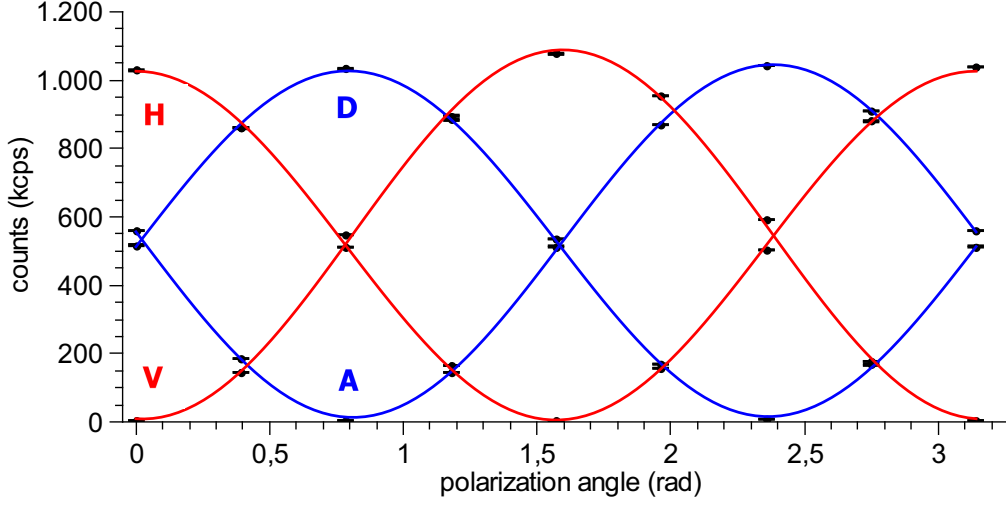


**Figure 2.10:** Polarization dependent count rates photons polarization-coherently upconverted to 532 nm from an 810 nm attenuated diode laser with different input polarizations. The count rates were averaged for 10 s integration time. Red lines represent sinusoidal fits to horizontal (H) and vertical (V) polarization inputs and blue lines are the fits for the  $+45^\circ$  (D) and  $-45^\circ$  (A) linear polarization inputs. The visibility of the fringes is very high with around 99% for all the 4 curves. The measurement uncertainties from Poissonian count statistics are smaller than the dots.

D, A, R, L) could now be measured. The following table lists the counted photons integrated for 10 s for the 36 corresponding combinations of input and output polarizations:

	H	V	D	A	R	L	Vis (%)
H	10777778	46883	5928379	5472043	5561798	5049212	99.134(4)
V	41054	10290901	5035933	5117344	5056333	4706893	99.205(4)
D	5131334	5593718	10428690	57627	5458093	4744330	98.901(5)
A	5346044	5171147	62928	10333076	5234882	4709559	98.789(5)
R	5159974	5794461	5395178	5606724	10451169	47125	99.102(4)
L	5543593	5320076	5203164	5520736	56135	10200428	98.905(5)

The last column of this table shows the visibility directly calculated from the number of counts with errors stemming from assumed poissonian count statistics. It very well supports the high visibilities calculated from the fits

of the polarization fringes with the average directly measured visibility being 99.0(1)%. As a more thorough analysis this data set can be used for a quantum process tomography [63, 13]. In general this reconstruction of the process matrix allows the calculation of the (mixed) output state for an arbitrary (mixed) input state and therefore yields the maximum information that is experimentally accessible. Here I used reconstruction techniques and numerical computer code based on convex optimization in detail developed and explained in [50].

The resulting reconstructed process matrix is shown in figure 2.11 and 2.12 in the Pauli-basis. For an ideal polarization preserving process one would expect only one matrix element - the  $Id \times Id$  element - to be 1 and all others to be zero. Indeed, the reconstructed matrix is very close to this. As a quantitative measure from this matrix the process fidelity to the target (identity) process and the process purity can be calculated [50]. They are:  $F = 99.23(1)\%$  and  $P = 98.54(1)\%$ . This again shows the very high quality of the polarization coherence that is observed experimentally. The error margins are deduced from Monte-Carlo simulations assuming errors in the counts stemming from Poissonian statistics. The distinct reduction in the process purity from the ideal value of 1 means that mixing is the main error contribution rather than residual (unitary) rotations, that could be easier compensated after the conversion. This mixing points to different origins for the deviations of the fidelity from 100%. A slight misalignment in the direction of the optical axis of the two ppKTP crystals seems to be likely. Also slight errors in the retardation of the wave-plates used for preparing the input states and for measuring the output states would lead to mixing in the resulting reconstructed process matrix. However, at the moment the polarization coherence is on a very high level, so that in experiments applying this conversion techniques other error sources will be dominant.

### Quantum state tomographies

As a next step, the performance of the polarization coherent setup for converting one photon of a polarization entangled photon pair at 810 nm to 532 nm is demonstrated and characterized. For this purpose, full quantum state tomographies of the 810-810 nm input state and the 532-810 nm output state were performed. The photon pairs were produced by the entangled photon source described in 2.3.1. One arm of the source was connected to the upconversion setup with a single mode fiber. The polarizer and QWP necessary for measuring the polarization of the not converted 810 nm photon

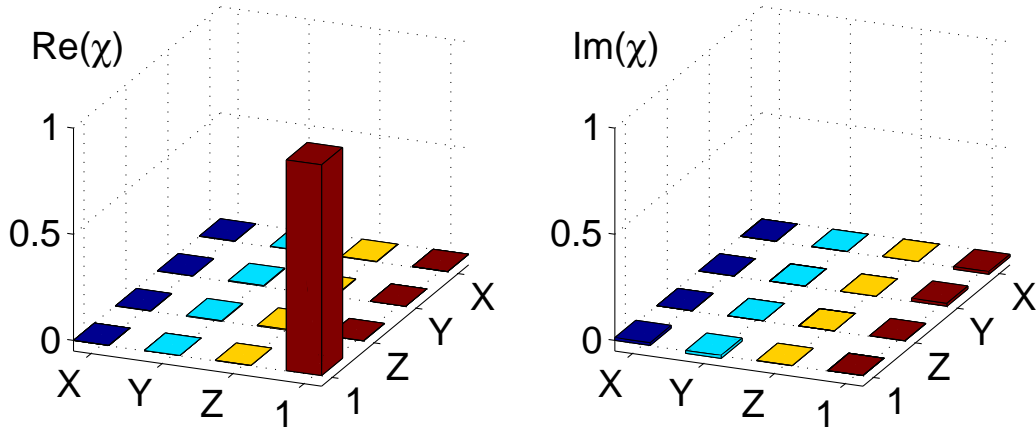


**Figure 2.11:** Reconstructed Process Matrix in the Pauli basis measured with an attenuated diode laser. The height of the (1,1) element of 0.992 corresponds to the process fidelity. The purity  $P$  of the process calculated from this matrix is 0.985(4).

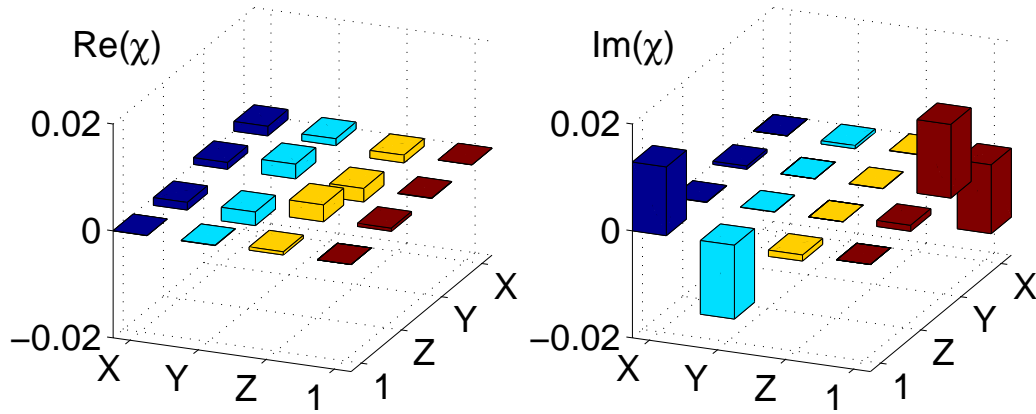


**Figure 2.12:** close up of the process matrix with out the (1,1) element

were placed directly in the source. For the state tomographies the coincidence rates for all combinations of polarizations (H,V,D,A,R,L) – in total 36 coincidence rates (CCs) – were measured for 100 s for the output state and for 1 s for the input state. The following tables give the recorded counts for the measurement of the input and the output state:

**INPUT**

(CCs in 1 s)	H	V	D	A	R	L
H	1861	69962	37711	38037	38914	34869
V	76020	1710	36816	40367	36386	40212
D	40375	33533	70333	2067	33395	38430
A	35988	35455	2187	69919	37789	33514
R	37598	34402	38622	34364	68289	2212
L	32764	35498	32267	36270	2308	68613

## ACCs

(CCs in 1 s)	H	V	D	A	R	L
H	1126	1144	1082	1144	1119	1086
V	1006	976	996	968	972	940
D	1052	1077	1076	981	1014	993
A	963	975	996	1027	939	1039
R	964	1031	981	988	995	919
L	955	1026	950	1041	1006	969

**OUTPUT**

(CCs in 100 s)	H	V	D	A	R	L
H	43	1738	1060	817	918	876
V	1247	61	615	753	679	771
D	778	723	1429	73	829	781
A	612	983	77	1582	741	728
R	644	828	944	735	1350	66
L	621	1002	753	441	90	1494

## ACCs

(CCs in 100 s)	H	V	D	A	R	L
H	29	37	32	36	33	41
V	31	33	35	30	36	40
D	34	21	34	39	28	28
A	35	20	41	39	21	26
R	31	34	30	29	24	43
L	40	14	34	37	35	35



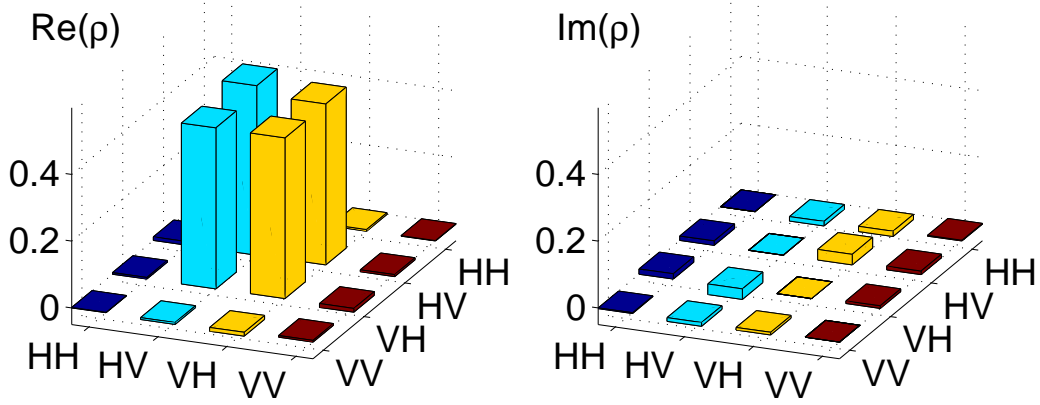


**Figure 2.13:** Reconstructed density matrix of the entangled (close to a  $\psi^+$ ) input state (two photons at 810 nm and 810 nm) with accidental correction. From this the calculated fidelity ( $F$ ), purity ( $P$ ) and tangle ( $T$ ) are:  $F = 97.93 \pm 0.03\%$ ,  $P = 95.96 \pm 0.06\%$  and  $T = 91.9 \pm 0.1\%$  (error margins estimated from Monte Carlo simulations based on Poissonian count statistics)

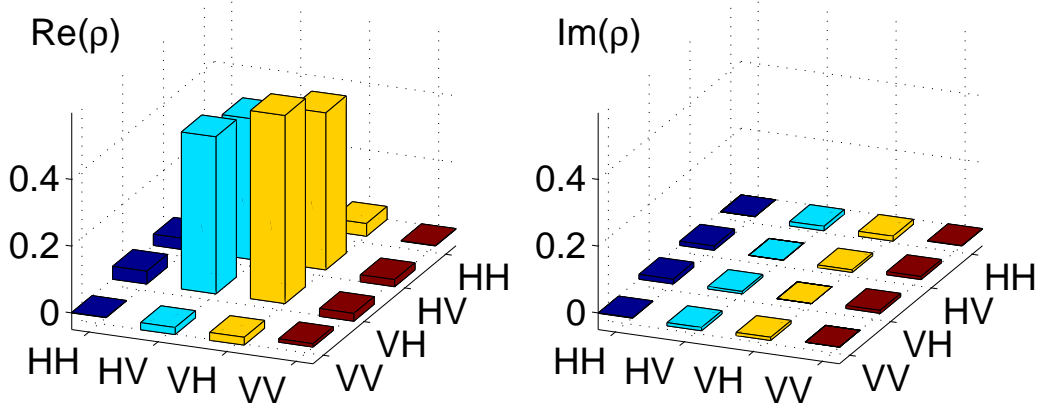


**Figure 2.14:** Reconstructed density matrix of the output two photon state (810 nm, 532 nm) after the polarization coherent conversion with accidental correction. The calculated fidelity ( $F$ ), purity ( $P$ ) and tangle ( $T$ ) are:  $F = 96.7 \pm 0.2\%$ ,  $P = 94.7 \pm 0.4\%$  and  $T = 88 \pm 1\%$  (error margins estimated from Monte Carlo simulations based on Poissonian count statistics)

The most distinct error contribution in these measurements are accidental coincidences (ACCs). These coincidences are measured when two photons are recorded (accidentally) within the coincidence window, although they do not originate from the same pair of photons but each from one of two unrelated pairs (double pair emission in negligible in this and most other cw pumps down-conversion experiments). In typical cw experiments like here this rate could in principle be made negligibly small by reducing the overall rate (accidental coincidences scale quadratically with the count rates) or by imposing a very narrow coincidence window as small as the coherence time of the photons. Unfortunately the latter is much shorter (order of ps) than the timing jitter of typical photon detectors (100s of ps). Also lowering the count rates is only practical to a certain point limited by the measurement time (that needs to be on a feasible time scale) that is needed to achieve a sufficient number of coincidences to be recorded for sufficient statistical certainty. To not only rely on estimates of the accidental rates they are measured independently in parallel for every combination of input and output polarization. The effective coincidence window ( $\tau_{CC}$ ) in these measurements was around 5 ns. The expected accidental rate given by  $R_{ACC} = R_{Singles1} * R_{Singles2} * \tau_{CC}$  agrees very well with the observed accidental rates.

For the numerical reconstruction of the density matrix of the input and output state techniques and code fully based on [50] are used. To access the "intrinsic" polarization coherence of the upconversion for the entangled state, the accidental coincidences need to be subtracted from the raw counts. The resulting density matrices (accidental corrected) can be seen in figures 2.13 and 2.14.

To sum up the results of the quantum state tomographies the fidelities (to the maximal entangled state), purities and tangle before and after the conversion are summarized in the following table:

	input	output	ratio
Fidelity	97.93(3)%	96.7(2)%	0.987(3)
Purity	95.96(6)%	94.7(4)%	0.987(4)
Tangle	91.9(1)%	88(1)%	0.96(1)
overlap fidelity		F	0.978(4)
trace distance		D	0.088(4)

It can be seen that the decrease in fidelity and purity is around 1% in best agreement with the 99% visibility and fidelity in the process tomography measurements with the attenuated diode laser input. It can also be seen that the tangle as a more sensitive measure for entanglement decreases slightly

more during the conversion process. To further confirm the high quality of polarization conversion, the trace distance  $D$  and overlap fidelity  $F$  of the input and output density matrix are calculated (see e.g. [58]):

$$D(\rho_{in}, \rho_{out}) = \frac{1}{2} \text{Tr}(|\rho_{in} - \rho_{out}|) \quad (2.48)$$

$$F(\rho_{in}, \rho_{out}) = (\text{Tr}(\sqrt{\sqrt{\rho_{in}}\rho_{out}\sqrt{\rho_{in}}}))^2 \quad (2.49)$$

The calculated distance measures are also shown in the above table with error margins calculated from Monte-Carlo simulations based on Poissonian count statistics. The overlap fidelity is close to 98% and also the small trace distance again underline the very good polarization coherence. Ideally one would expect the overlap fidelity to be close to the process fidelity. However there is an additional decrease of 1% from the 99% process fidelity to the 98% overlap fidelity. This can be most likely attributed to the much shorter coherence time of the downconversion photons (around 2 ps) compared to the attenuated diode laser (on the order of 1  $\mu$ s) together with non-perfect temporal walk-off compensation.

For completeness, also the density matrices without correcting for accidental coincidences have been calculated. The resulting matrices are shown in figures 2.15 and 2.16. They show decreased performance parameters due to the non-corrected accidental coincidences, which are more pronounced for the output, because here due to the low conversion efficiency the accidental rates are – relative to the real coincidences – one order of magnitude bigger than for the input state. The density matrix of the output state without accidental correction can be used to estimate the measured Bell value  $S$  (details and the actual measurement in the next paragraph), that can be achieved with this state. The  $S$  value estimated from this is  $S = 2.596(15)$ , where the error in this estimate stems again from Monte Carlo simulation assuming a Poissonian count statistics.

### Bell violation measurements

One of the most stringent demonstrations of the entanglement for the converted, polarization-entangled state (of the 532 nm - 810 nm photon pair) is the experimental violation of a Bell Inequality [8]. One of the most useful forms of a Bell inequality is the CHSH type [15]. Here we use it in the following form:

$$E(\alpha, \beta) - E(\alpha, \beta') + E(\alpha, \beta') + E(\alpha', \beta') \leq 2 \quad (2.50)$$

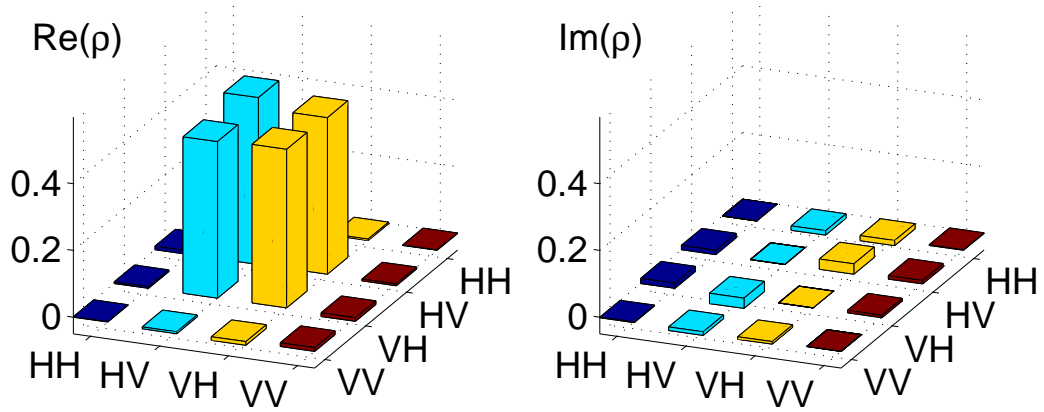


**Figure 2.15:** Reconstructed density matrix of the input two photon state (810 nm, 810 nm) without accidental correction,  $F = 95.91 \pm 0.04\%$ ,  $P = 92.09 \pm 0.07\%$  and  $T = 84.3 \pm 0.1\%$

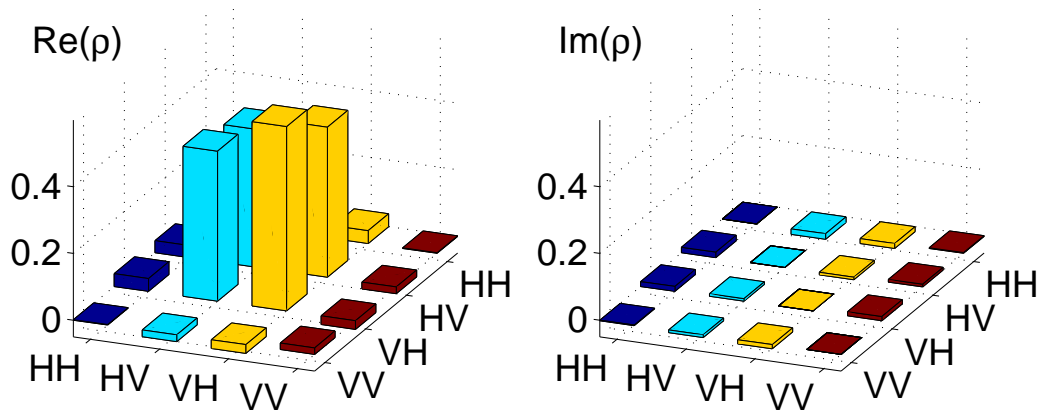


**Figure 2.16:** Reconstructed density matrix of the output two photon state (810 nm, 532 nm) without accidental correction,  $F = 93.8 \pm 0.3\%$ ,  $P = 89.1 \pm 0.6\%$  and  $T = 77 \pm 1\%$

where the  $E(\cdot, \cdot)$  are the correlations defined in our case with the angles  $\alpha = 0^\circ, \alpha' = 45^\circ, \beta = 22.5^\circ, \beta' = 67.5^\circ$ :

$$E(\alpha, \beta) = \frac{CC_{0^\circ, 22.5^\circ} + CC_{90^\circ, 112.5^\circ} - CC_{0^\circ, 112.5^\circ} - CC_{90^\circ, 22.5^\circ}}{CC_{0^\circ, 22.5^\circ} + CC_{90^\circ, 112.5^\circ} + CC_{0^\circ, 112.5^\circ} + CC_{90^\circ, 22.5^\circ}} \quad (2.51)$$

$$E(\alpha, \beta') = \frac{CC_{0^\circ, 67.5^\circ} + CC_{90^\circ, 157.5^\circ} - CC_{0^\circ, 157.5^\circ} - CC_{90^\circ, 67.5^\circ}}{CC_{0^\circ, 67.5^\circ} + CC_{90^\circ, 157.5^\circ} + CC_{0^\circ, 157.5^\circ} + CC_{90^\circ, 67.5^\circ}} \quad (2.52)$$

$$E(\alpha', \beta) = \frac{CC_{45^\circ, 22.5^\circ} + CC_{135^\circ, 112.5^\circ} - CC_{45^\circ, 112.5^\circ} - CC_{135^\circ, 22.5^\circ}}{CC_{45^\circ, 22.5^\circ} + CC_{135^\circ, 112.5^\circ} + CC_{45^\circ, 112.5^\circ} + CC_{135^\circ, 22.5^\circ}} \quad (2.53)$$

$$E(\alpha', \beta') = \frac{CC_{45^\circ, 67.5^\circ} + CC_{-45^\circ, 157.5^\circ} - CC_{45^\circ, 157.5^\circ} - CC_{-45^\circ, 67.5^\circ}}{CC_{45^\circ, 67.5^\circ} + CC_{-45^\circ, 157.5^\circ} + CC_{45^\circ, 157.5^\circ} + CC_{-45^\circ, 67.5^\circ}} \quad (2.54)$$

Using the same setup as for the characterisation measurements the following coincidences within 100 s for the different combinations of angles were measured:

	22.5°	112.5°	67.5°	157.5°
0°	1634	249	346	1475
90°	186	1241	1073	283
	<b>E<sub>1</sub></b>	<b>0.737(12)</b>	<b>E<sub>2</sub></b>	<b>-0.604(14)</b>
	22.5°	112.5°	67.5°	157.5°
45°	1181	282	1252	252
135°	431	1177	160	1480
	<b>E<sub>3</sub></b>	<b>0.536(15)</b>	<b>E<sub>4</sub></b>	<b>0.738(12)</b>

$$\mathbf{S} = \mathbf{2.615(27)} > 2 \quad (2.55)$$

Combining these measurement yields an S-value which drastically violates the classical bound of 2 (by more than 20 standard deviations) and therefore proves the high degree of entanglement that is present in the converted state. As emphasized before, no background subtraction whatsoever was used to obtain this result. The experimentally measured S-value also agrees very well, with the one theoretically deduced from the uncorrected density matrix of the output state (see above) of 2.596(15).

The ideal value predicted by quantum mechanics would be  $S = 2\sqrt{2} \approx 2.828$ . The main reason, why this was not experimentally observed are accidental coincidences which reduce the measured S value by  $\approx 5\%$ . The remaining 3% reduction are caused by the reduced entanglement of the state with a fidelity to the maximal-entangled state of around 97% (accidental corrected).

## 2.5 Conclusions and outlook

Our setup is flexible, compact and robust; it uses simple bulk nonlinear materials, requires no complex cryogenic or vacuum apparatus, and is compatible with standard integrated-fibre and waveguide technologies, and is thus well-suited for large-scale deployment in quantum networks and possibly other future quantum technologies benefiting from quantum frequency conversion.

For this work the experimental setup was designed for high-fidelity entanglement transfer without emphasis on efficiency. Using longer crystals and moving to bi-directionally pumped schemes (e.g. Sagnac-type, or Michelson-type interferometers [2]), which would solve the problem of the focus not being located in the crystal centre, could increase the efficiency by more than one order of magnitude.

Note that the wavelengths in the setup are interchangeable. Converting 810 nm to 532 nm, as demonstrated here, has its merits – custom 532 nm single-photon detectors can have up to 10 times lower timing jitter than their 810 nm counterparts and superconducting nano-wire detectors are more efficient at shorter wavelengths. Upconverting 1550 nm photons, however – particularly interesting for accessing fiber compatible wavelengths – can also be achieved by pumping with 810 nm, where powerful lasers are readily available.

As a side remark, we would like to stress that any polarization-coherent frequency conversion device using sum-frequency generation is equivalent to a polarization-entangled down-conversion pair source run in reverse. Therefore, most advantages of the designs and technologies for perfecting entanglement sources can be also used to optimise a quantum frequency-conversion experiment. For example one could think of an polarization coherent upconversion design, based on a polarization sagnac configuration in perfect analogy the sagnac-based polarization entanglement source. The resulting setup would benefit from the same advantages like auto-compensated phase, focus in the middle of the crystal for increased efficiency and perfect equivalence of the two arms (because the physically same crystal is used).

Finally, as an future challenge, we would like to raise the interesting possibility of simultaneously changing the photon bandwidth by suitably designed phase-matching at the same time as converting the wavelength. This could prove extremely useful, especially in the context of interfacing photons with bandwidth-limited quantum memories.

## **2.6 Publication arXiv:1106.1867**

# Polarization-entanglement conserving frequency conversion of photons

S. Ramelow<sup>1,2</sup>, A. Fedrizzi<sup>2,\*</sup>, A. Poppe<sup>1,3</sup>, N. K. Langford<sup>1,2,†</sup>, and A. Zeilinger<sup>1,2</sup>

<sup>1</sup>*Vienna Center for Quantum Science and Technology (VCQ), Faculty of Physics,  
University of Vienna, Boltzmannngasse 5, A-1090 Vienna, Austria*

<sup>2</sup>*Institute for Quantum Optics and Quantum Information,  
Austrian Academy of Sciences, Boltzmannngasse 3, A-1090 Vienna, Austria*

<sup>3</sup>*Austrian Institute of Technology (AIT), Donau-City-Straße 1, 1220 Vienna, Austria*

Entangled photons play a pivotal role in the distribution of quantum information in quantum networks. However, the frequency bands for optimal transmission and storage of photons are often not the same. Here, we experimentally demonstrate the coherent frequency conversion of photons entangled in their polarization, a widely used degree of freedom in photonic quantum information processing. We verify the successful entanglement conversion by violating a Clauser-Horne-Shimony-Holt (CHSH) Bell inequality and fully characterise our near-perfect entanglement transfer using both state and process tomography. Our implementation is robust and flexible, making it a practical building block for future quantum networks.

Quantum frequency conversion of single photons offers an elegant way to avoid the often difficult trade-offs associated with choosing one wavelength which is optimal for all parts of a connected quantum system. Quantum networks [1], for example, will facilitate the large-scale deployment of secure quantum communication [2]. They require the distribution of entanglement using flying qubits (photons) between quantum repeater nodes which can coherently store entanglement in quantum memories and concatenate it by entanglement swapping [3]. However, the standard wavelength for optical fiber transmission is 1550 nm, where loss is minimised, whereas the highest efficiencies for coherent optical memories suitable for quantum information applications have to date been achieved in Rubidium vapour at around 800 nm [4]. Such issues also arise in many other contexts, connected with, e.g., detector performance (for 1550 nm photons), general transmission and dispersion properties of materials used or the availability of suitable laser sources. Coherent frequency conversion of flying qubits can sidestep this type of problem altogether.

The basic process underlying optical frequency conversion is nonlinear sum frequency generation (SFG), where a pump and an input field are combined in a nonlinear medium to generate an output field with the sum of the input frequencies. A major experimental motivation for this has been to solve the detection problem for telecom-band single photons, by converting them to the visible regime and using, instead of InGaAs-based photodetectors, the better performing Silicon detectors [5–8]. In the single-photon regime, where the input field is much weaker than the pump, near-100% conversion efficiencies can be achieved by optimising interaction nonlinearities (e.g., by using waveguides [7, 8]) or by using high pump intensities (e.g. with cavities [5], or pulsed pump lasers [6]). Critically, the SFG process can also conserve the quantum properties of the input light [9] and fulfil the fundamental requirements for universal photonic quantum interfaces: firstly, the conversion process must

preserve the photons' indistinguishability [10, 11] and single-photon character [12]; secondly, it must also preserve quantum information, and in particular entanglement, stored in the photons. Polarization entanglement is widely used in an array of quantum optics applications because of the remarkable precision and ease with which it can be generated, controlled and measured. While phase- and polarization-maintaining conversion has been shown for classical fields [13–15] and conservation of entanglement has been reported for time-bin-entangled photons [16], entanglement-preserving conversion in the widely used and easily controlled polarization degree of freedom has so far been achieved with highly narrow-band photons using four-wave mixing in cold Rb vapour in high-vacuum environments [17].

Here, we demonstrate coherent conversion of *polarization-entangled* photons. Our architecture is compatible with integrated photonics technology by using a compact, robust and simple design based on bulk crystal nonlinearities and off-the-shelf components. We stringently verified the entanglement transfer by violating a *Clauser-Horne-Shimony-Holt* (CHSH) [18] Bell inequality and fully characterised the near-perfect entanglement conversion using quantum state and process tomography. Coherent single-photon frequency conversion which preserves polarisation entanglement will be a key enabling step for future quantum optical technologies, and devices like ours with flexible wavelength tuning and robust designs will be critical to making these practical in any realistic scenario.

In our experiment, figure 1, the polarization-coherent up-conversion takes place in two orthogonally oriented, periodically-poled KTiOPO<sub>4</sub> (ppKTP) crystals. The crystals are designed for type-I quasi-phase-matching for 810 nm + 1550 nm → 532 nm, and oriented such that the horizontally (H) polarized component of the input at 810 nm is converted to 532 nm (also H) in the first crystal, and the vertical (V) component is converted in the second. The crystals are placed close to each



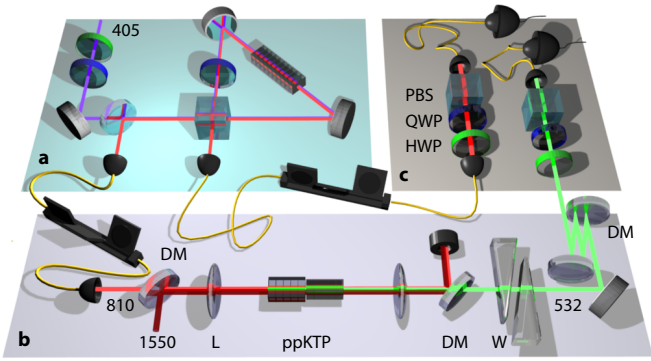


FIG. 1: Experimental scheme. (a) Polarization-entangled photon source. Photon pairs are created by spontaneous parametric downconversion in a periodically poled KTiOPO<sub>4</sub> (ppKTP) crystal which is bi-directionally pumped by a 405 nm diode laser in a polarization-Sagnac loop [19, 20]. (b) Polarization coherent up-conversion setup. Signal (810 nm) and pump (1550 nm), are combined with a dichroic mirror (DM) and focussed into the setup with a  $f = 50$  mm lens (L). The two polarization components of the input are up-converted to 532 nm in one of two 4.3 mm long, orthogonally oriented ppKTP crystals. The remaining 810 nm photons and 1550 nm pump light are separated from the 532 nm photons with dichroic mirrors: one in transmission and two in a z-configuration for multiple reflections. Two adjustable calcite wedges (W) compensate temporal walk-off. (c) The polarization analysis (and preparation for the process tomography) is implemented with a quarter-wave plate (QWP), half wave plate (HWP) and a polarizing element (PBS). The 532 nm photons are then coupled into a single-mode fiber and detected by a silicon avalanche photo-diode (Si-APD). The coincidences with the second 810 nm photon are identified by home-built coincidence logic.

other to maximize conversion efficiency as well as stability, and to minimize potential sources of mode distinguishability, which would decrease the polarization coherence. Chromatic dispersion and crystal birefringence cause a combined temporal walkoff of  $\sim 1.8$  ps between the orthogonal polarization components, similar to the photon coherence time [20]. To render the output photons indistinguishable, we compensate this walk-off with a pair of birefringent  $CaCO_3$  (calcite) wedges with a combined thickness of  $\sim 3$  mm. Thus, an input state  $\phi_{\text{in}}^+ = (|H_{810}H_{810}\rangle + |V_{810}V_{810}\rangle)/\sqrt{2}$  is converted into:

$$\psi_{\text{out}} = \eta_H |H_{810}H_{532}\rangle + e^{-i\theta} \eta_V |V_{810}V_{532}\rangle. \quad (1)$$

The phase  $\theta$ , as well as the relative conversion efficiency  $\eta_H/\eta_V$  between the two crystals can be controlled through the polarization state of the 1550 nm pump laser beam, which we adjust with fiber-polarization controllers. The pump laser system consists of a tunable, fiber-coupled external-cavity diode laser amplified to 1 W with a high-power erbium-doped fiber amplifier. The pump field and the entangled photons were combined with a dichroic mirror and focused to spot sizes of

$\sim 70 \mu\text{m}$  (1550) and  $\sim 50 \mu\text{m}$  (810). After recollimation, the 532 nm light was separated from both the 1550 nm pump and the 810 nm photons via multiple reflections off three dichroic mirrors, suppressing the unconverted 810 nm photons by at least 100 dB. The up-converted 532 nm photon and its entangled 810 nm partner photon were then subjected to polarization analysis and detected by single-photon avalanche photo diodes, with a detection efficiency of around 50% both at 532 nm and 810 nm.

In our experiment, the optical conversion bandwidth - an important parameter in frequency conversion setups - is determined by the phase-matching properties and the length of the crystals used. The 4.3 mm long ppKTP crystals provide an up-conversion bandwidth for the 810 nm photons of 410 GHz FWHM (0.9 nm). By comparison, the spectral bandwidth of photons used in the experiment was 250 GHz FWHM (0.55 nm), well below this, thus excluding any significant reduction of the conversion efficiency.

The conversion efficiency of this setup for Gaussian beams is theoretically given by [5]:

$$\eta = \sin^2(\pi/2\sqrt{P_p/P_{max}}),$$

$$P_{max} = \frac{c\epsilon_0 n_1 n_2 \lambda_1 \lambda_2 \lambda_p}{128 d_{\text{eff}}^2 L h_m}, \quad (2)$$

with pump beam power  $P_p$ , input and output wavelengths  $\lambda_{1,2}$ , the corresponding crystal refraction indices  $n_{1,2}$ , the effective nonlinearity  $d_{\text{eff}}$ , crystal length  $L$  and the focussing factor  $h_m$  (for Gaussian beams). The spot sizes of  $\sim 70 \mu\text{m}$  (1550) and  $\sim 50 \mu\text{m}$  (810), corresponding to a focussing parameter  $\xi = \frac{L}{2z_R}$  (with Rayleigh length  $z_R$ ) of about 0.8 for both beams, yield  $h_m \sim 0.6$ . For the maximally available pump power of 1 W and a single 4.3 mm long crystal we thus expect an efficiency of  $\sim 0.8\%$ . Experimentally, calibration measurements with a 810 nm laser diode resulted in 270 nW of 532 nm light converted from an input of 28  $\mu\text{W}$  at 810 nm. Accounting for the wavelength difference and  $\sim 16\%$  optical loss, this implies an observed up-conversion efficiency of  $\sim 0.6\%$ . The discrepancy between theory and measurement is likely due to a slightly lower effective non-linear coefficient caused by non-perfect periodic poling.

For polarization-coherent operation we convert one photon of an entangled 810 nm/810 nm pair in the  $\phi^+$  state created by our entangled photon source. From  $7.3 \times 10^4$  counts per second (cps) input photon pairs, we detected 15 cps pairs after conversion, yielding an effective up-conversion efficiency of  $\sim 2 \times 10^{-4}$ . Considering fiber coupling losses of 50% this corresponds to an intrinsic conversion efficiency—directly after the crystals—of about 0.04%. After accounting for the reduction by 50% because each crystal is pumped at half the pump power and another  $\sim 82\%$  because the beam focus is located between the two crystals instead of the crystal centers, this number is in good agreement to the the-

oretical efficiency—primarily limited by available pump power—and our auxiliary laser diode measurements.

A stringent way to demonstrate that polarization entanglement is preserved in the conversion process is the violation of a Bell inequality [21], in our case the CHSH inequality [18] for the converted, 532 nm/810 nm polarization state:

$$S = E(\alpha, \beta) - E(\alpha, \beta') + E(\alpha', \beta) + E(\alpha', \beta') \leq 2, \quad (3)$$

where  $E(\cdot, \cdot)$  are the correlations for joint polarization measurements on two photons along the angles  $\alpha = 0^\circ, \alpha' = 45^\circ, \beta = 22.5^\circ, \beta' = 67.5^\circ$ . A Bell value above the classical bound of 2 implies that the measured state is incompatible with a local realistic model [18, 21] and is thus entangled. With about 15 cps coincidence rate and integrating over 100 seconds for each measurement, we recorded the coincidences for the 16 combinations of measurement angles which includes the combinations with the additional 4 angles rotated by 90 degrees from the above mentioned angles which is necessary to evaluate the bell parameter when using only one detector on each side with polarization filters. We obtained an experimental Bell parameter of

$$S_{\text{exp}} = 2.615 \pm 0.027, \quad (4)$$

which violates the classical bound by more than 20 standard deviations. The observation of entanglement in the output state is striking, because the original 810 nm photon has been annihilated and created again in the 532 nm mode—a rather invasive interaction.

To assess the quantum nature of the up-conversion process, we characterized it using tomographic techniques. We first performed process tomography [22, 23] with a strongly attenuated laser diode to assess the *intrinsic*, i.e. independent of non-perfect detector-performance, dynamics of the entanglement transfer. We prepared the input states  $\{|H\rangle, |V\rangle, |D\rangle, |A\rangle, |R\rangle, |L\rangle\}$  and, for each input, measured the same set of 6 observables for the up-converted 532 nm single-photon output, where  $|D\rangle = (|H\rangle + |V\rangle)/\sqrt{2}$ ,  $|A\rangle = (|H\rangle - |V\rangle)/\sqrt{2}$ ,  $|R\rangle = (|H\rangle + i|V\rangle)/\sqrt{2}$  and  $|L\rangle = (|H\rangle - i|V\rangle)/\sqrt{2}$ . According to Eq. 1, for  $\theta=0$  and balanced conversion,  $\eta_H=\eta_V$ , the ideal process matrix  $\chi_{\text{ideal}}$  has a single non-zero element  $(I, I)$  in the Pauli basis representation. This is very close to the reconstructed process matrix, figure 2 which has a process fidelity [24] to the ideal case of  $\mathcal{F} = 99.23 \pm 0.01\%$ . This indicates that the conversion process has excellent polarization coherence.

We subsequently characterized in detail the entanglement transfer: we performed two-qubit quantum state tomography [24] on both the entangled photon input state and the entangled photon output state and compared the two (see figure 3). For this we measured a total of 36 combinations of the 6 single-qubit observables  $\{|H\rangle, |V\rangle, |D\rangle, |A\rangle, |R\rangle, |L\rangle\}$ , for a measurement time of

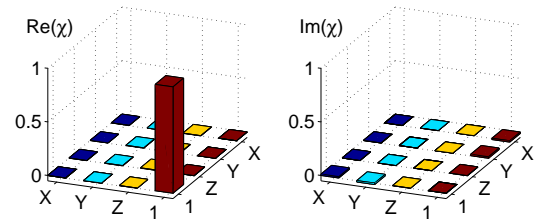


FIG. 2: Process matrix  $\chi$  (Pauli-basis representation) for polarization-coherent up-conversion, characterised with an attenuated 810 nm diode laser. The different elements of  $\chi$  access what kind of operation—decomposed into the Pauli-operations—an input state is subject to, with the dominating element denoting the identity operation. The calculated process fidelity  $\mathcal{F}$  and purity ( $P$ ) are  $\mathcal{F} = 99.23 \pm 0.01\%$  and  $P = 98.54 \pm 0.01\%$ . Error margins for  $\mathcal{F}$  and ( $P$ ) are determined assuming from Poissonian count statistics.

1 second for the 810 nm/810 nm polarization-entangled input state and 100 seconds for the 810 nm/532 nm output state in which the first 810 nm photon remained unchanged. We used maximum-likelihood optimization to reconstruct the two-qubit density matrices from these measurements, and calculated several key diagnostic parameters: the input state fidelity (with the maximally entangled Bell state  $\phi^+$ ) is  $\mathcal{F}_{\rho_{\text{in}}} = 95.91 \pm 0.04\%$  and tangle is  $\mathcal{T}_{\rho_{\text{in}}} = 84.3 \pm 0.1\%$ . These values decrease to  $\mathcal{F}_{\rho_{\text{out}}} = 93.8 \pm 0.3\%$  and  $\mathcal{T}_{\rho_{\text{out}}} = 77 \pm 1\%$  for the (partially) up-converted states.

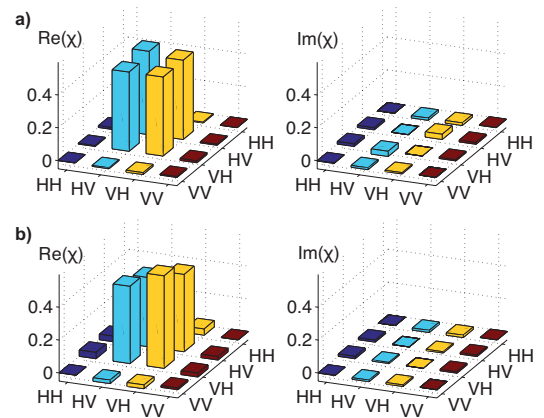


FIG. 3: Reconstructed (accidental-corrected) two-qubit density matrices of entangled input states and output states a) Input state (810 nm/810 nm) with a corresponding fidelity with respect to the  $\psi^+$  state of  $F_{\text{in}} = 97.93 \pm 0.03\%$  b) Output state (810 nm/532 nm) with  $F_{\text{out}} = 96.7 \pm 0.2\%$ . The fidelities as well as the values for the purities ( $P$ ) and tangles ( $T$ ) of the input and output states are summarized in figure 4. Error margins follow from Monte-Carlo simulations assuming errors from Poissonian count statistics.

An error analysis shows that the most significant error contribution was caused by accidental coincidence counts, which occur when two photons from unrelated

pairs are recorded within the coincidence time window. Double-pair emissions were negligible and we did not observe any statistically significant pump-induced background counts. We estimated the accidental coincidence rates for every input and output measurement configuration by splitting one of the detector signals and measuring the coincidences with a relative time delay between the channels.

An error analysis shows that the most significant error contribution for both tomographic and Bell-test results was caused by accidental coincidence counts, which occur when two photons from unrelated pairs are recorded within the coincidence time window. These cannot be fully distinguished from the correlated pairs, because the limited timing resolution of the single photon detectors ( $\approx 1$  ns) is much longer than the photon's coherence time ( $\approx 3$  ps). However, compared with the total coincidence count rate, the accidental count rates were mostly much lower, only reaching comparable levels for the polarization combinations exhibiting minima in the coincidences due to the high-fidelity entanglement. Note that this is itself an indication of the high quality of the polarization-preserving process. We did not observe any statistically significant pump-induced background counts. We estimated the accidental coincidence rates for every input and output measurement configuration by splitting one of the detector signals and measuring the coincidences with an additional relative time delay between the channels. We now subtract these accidentals from the raw coincidence counts in reconstructing our output states to probe the intrinsic quality of the up-conversion process.

The resulting density matrices are shown in figure 3. The parameters for the corrected output states are  $\mathcal{F}_{\rho_{\text{out}}} = 96.7 \pm 0.2\%$ ,  $\mathcal{P}_{\psi_{\text{out}}} = 94.7 \pm 0.4\%$  and  $\mathcal{T}_{\rho_{\text{out}}} = 88 \pm 1\%$ . These and the corresponding values calculated from the accidental-corrected (as explained above) input state are summarized in figure 4. The exceptional quality of the polarization entanglement transfer is further highlighted by the overlap fidelity between the entangled input and output states of  $\mathcal{F}_{\rho_{\text{in}}, \rho_{\text{out}}} = 97.8 \pm 0.4\%$ .

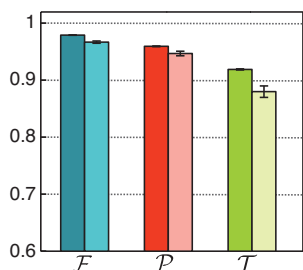


FIG. 4: Summary of the quality parameters for the accidental corrected input states  $\rho_{\text{in}}$  (dark) and output states  $\rho_{\text{out}}$  (light): Fidelities  $\mathcal{F}$ , purities  $\mathcal{P}$  and tangle  $\mathcal{T}$ . Error bars were obtained from Monte-Carlo runs of the tomographic reconstruction with assumed Poissonian count statistics.

To conclude, we have shown and verified the conversion of polarization entanglement with intrinsically near unity fidelity using quantum state and process tomography. We furthermore violated a Bell inequality for the converted state. Our setup is flexible, compact and robust; it uses simple bulk nonlinear materials, requires no cryogenic or vacuum apparatus and is compatible with standard integrated-fibre and waveguide technologies. It is thus well suited for large-scale deployment in quantum networks and other quantum technologies where wavelength conversion is essential. Our conversion efficiencies are close to the theoretically calculated limit imposed by the available pump power and can be straightforwardly enhanced by known techniques to achieve near unity single-photon efficiencies [5–8]. Specifically, for our polarization coherent design the efficiency can be significantly increased by using longer crystals and moving to bidirectionally pumped schemes (e.g. Sagnac-, or Michelson-type interferometers [14]). Importantly, with pump schemes like ours where the pump has a lower frequency than the converted photons [25, 26] the conversion can remain free of pump-induced noise even at the required high pump power.

Converting 810 nm to 532 nm, as demonstrated here, can be important for various reasons; for example custom 532 nm single-photon detectors can have up to 10 times lower timing jitter than their 810 nm counterparts and superconducting nanowire detectors as well as CCD-based imaging systems are more efficient at shorter wavelengths. The quasi-phasematched interaction allows very flexible wavelength tuning (by temperature tuning of the crystal or adjusting the pump wavelength) Moreover, the wavelengths in our setup are interchangeable. Up-converting 1550 nm photons can be achieved by pumping with 810 nm, where powerful lasers are readily available. Coherent frequency conversion also opens up avenues in fundamental physics, such as enabling access to superposition bases for color qubits [27]. Finally, a future interesting challenge will be to also change the photons' spectral bandwidth during frequency conversion via suitably designed phase matching similar to [28]. This could prove useful for interfacing photons with narrow-bandwidth quantum memories.

We thank M. Hentschel and T. Jennewein for valuable discussions. This work has been supported by the Austrian Science Fund within SFB 015 P06, P20 and CoQuS (W1210), by the ERC (Advanced Grant QIT4QAD) and the European Commission project QESSENCE.

\* Present address: ARC Centre for Engineered Quantum Systems, ARC Centre for Quantum Computer and Communication Technology, School of Mathematics and Physics, University of Queensland, Brisbane 4072, Australia

- † Present address:: Clarendon Laboratory, Department of Physics, University of Oxford, Parks Road, Oxford OX1 3PU, UK
- [1] L. Duan, M. D. Lukin, J. I. Cirac, and P. Zoller, *Nature (London)* **414**, 413 (2001).
  - [2] V. Scarani, H. Bechmann-Pasquinucci, N. J. Cerf, M. Duscарonek, N. Lütkenhaus, and M. Peev, *Rev. Mod. Phys.* **81**, 1301 (2009).
  - [3] J.W. Pan, D. Bouwmeester, H. Weinfurter, and A. Zeilinger, *Phys. Rev. Lett.* **80**, 3891 (1998).
  - [4] M. Hosseini, B. Sparkes, G. Campbell, P. Lam, and B. Buchler, *Nat Commun* **2**, 174 (2011).
  - [5] M. Albota and F. Wong, *Optics letters* **29**, 1449 (2004).
  - [6] A. Vandevender and P. Kwiat, *Journal of Modern Optics* **51**, 1433 (2004).
  - [7] C. Langrock, E. Diamanti, R. Roussev, Y. Yamamoto, M. Fejer, and H. Takesue, *Optics Letters* **30**, 1725 (2005).
  - [8] R. Thew, S. Tanzilli, L. Krainer, S. Zeller, A. Rochas, I. Rech, S. Cova, H. Zbinden, and N. Gisin, *New Journal of Physics* **8**, 32 (2006).
  - [9] P. Kumar, *Optics Letters* **15**, 1476 (1990).
  - [10] H. Takesue, *Phys. Rev. Lett.* **101**, 173901 (2008).
  - [11] K.A. O'Donnell and A.B. U'Ren, *Phys. Rev. Lett.* **103**, 123602 (2009).
  - [12] M. T. Rakher, L. Ma, O. Slattery, X. Tang, and K. Srinivasan, *Nature Photonics* **4**, 786 (2010).
  - [13] G. Giorgi, P. Mataloni, and F. DeMartini, *Phys. Rev. Lett.* **90**, 027902 (2003).
  - [14] M. A. Albota, F. N. C. Wong, and J. H. Shapiro, *JOSA B* **23**, 918 (2006).
  - [15] A. P. VanDevender and P. G. Kwiat, *JOSA B* **24**, 295 (2007).
  - [16] S. Tanzilli, W. Tittel, M. Halder, O. Alibart, P. Baldi, N. Gisin, and H. Zbinden, *Nature (London)* **437**, 116 (2005).
  - [17] Y. O. Dudin, A. G. Radnaev, R. Zhao, J. Z. Blumoff, T. A. B. Kennedy, and A. Kuzmich, *Phys. Rev. Lett.* **105**, 260502 (2010).
  - [18] J. F. Clauser, M. A. Horne, A. Shimony, and R. A. Holt, *Phys. Rev. Lett.* **23**, 880 (1969).
  - [19] T. Kim, M. Fiorentino, and F. N. C. Wong, *Physical Review A* **73**, 012316 (2006).
  - [20] A. Fedrizzi, T. Herbst, A. Poppe, T. Jennewein, and A. Zeilinger, *Optics Express* **15**, 15377 (2007).
  - [21] J. S. Bell, *Physics* **1**, 195 (1964), published in Long Island City (NY) by Physics Publishing Co.
  - [22] J. F. Poyatos, J. I. Cirac, and P. Zoller, *Phys. Rev. Lett.* **78**, 390 (1997).
  - [23] I. Chuang and M. Nielsen, *Journal of Modern Optics* **44**, 2455 (1997).
  - [24] D. F. V. James, P. G. Kwiat, W. J. Munro, and A. G. White, *Phys. Rev. A* **64**, 52312 (2001).
  - [25] H. Dong, H. Pan, Y. Li, E. Wu, and H. Zeng, *Applied Physics Letters* **93**, 071101 (2008).
  - [26] H. Kamada, M. Asobe, T. Honjo, H. Takesue, Y. Tokura, Y. Nishida, O. Tadanaga, and H. Miyazawa, *Optics Letters* **33**, 639 (2008).
  - [27] S. Ramelow, L. Ratschbacher, A. Fedrizzi, N. K. Langford, and A. Zeilinger, *Phys. Rev. Lett.* **103**, 253601 (2009).
  - [28] D. Kielpinski, J. F. Corney, and H. M. Wiseman, *Phys. Rev. Lett.* **106**, 130501 (2011).

## Chapter 3

# Coherent photon conversion (CPC)

In this chapter the novel scheme of coherent photon conversion (CPC) is introduced and the results of a first proof of principle experiment are presented. The chapter is divided into different sections: the first giving an overview of the motivation and state-of-the-art, followed by an outline of the principles and main applications related to CPC and some principles related the experiment. In the next section, the experimental setup is described. Finally, the experimental results are shown and analyzed and the conclusions from these and an outlook are presented.

The presented project, which resulted in the attached publication [cite] was undertaken in a strongly collaborative way, involving all co-authors of this publication, but especially Nathan Langford. Particularly, much of the material of this publication has also been adopted for parts of this chapter.

### 3.1 Introduction

Encoding quantum information in single photons has been used with huge success in the last decades in quantum experiments. For example, photonic qubits were used in the earliest fundamental quantum experiments demonstrating entanglement[14] and also to produce the highest-quality entanglement reported to date[7, 25]. In general, photons offer remarkable advantages for experimental implementations: they show virtually no decoherence because they do not couple to the environment. Also single qubit manipulations are very easy to accomplish leading to robust and compact experiments usually without any vacuum or cryogenic requirements. Consequently, photons have been suggested very early as promising candidates for the physical implementation of quantum information processing (QIP) including universal quantum computation[58]. Universal quantum computers would lead to potentially revolutionary applications because they promise to greatly increase the efficiency of solving computational problems not tractable by classical computers such as factoring large integers or search and optimisation problems as well as combinatorial optimization or the simulation of otherwise too complex quantum physical systems.

However, one of the key challenges for photonic QIP is to induce strong interactions between individual photons, which cannot be realised with standard linear optical components. The seminal proposal by Knill, Laflamme and Milburn for linear optics quantum computing[41, 42] (LOQC) could sidestep this problem by using the inherent nonlinearity of photodetection and non-classical interference to induce effective nonlinear photon interactions non-deterministically.

One important necessary criterion for universal quantum computation is the availability of two-qubit entangling gates. Linear optical entangling gates for two photons implemented so far[62, 59] are, however, non-deterministic and based on post-selection. This has the consequence that they are not easily concatenateable, which would be necessary for building up quantum circuits with many gates. Another challenge of implementing LOQC are deterministic sources of indistinguishable single photons. Spontaneous parametric downconversion (SPDC) has been an overwhelmingly successful technique for the creation of heralded single photons and entangled photon pairs as well as multi-photon entangled states[89]. Despite this, due to the intrinsically probabilistic emission of photons in this process and also the significant error contributions from higher order terms SPDC alone is not suited well for scaling the number of photons up to high numbers. Alternative sources of single photons – for example based on semiconductor quantum dots – currently also have significant limitations like low collection efficiencies or poor quality of the spectral characteristics that make them not yet viable solutions for the problem of the scalable creation of many single photons.

A third major obstacle to reach universal quantum computing with photons is the non-unity detection efficiency of currently available detectors. However, recent progress in the development of so called transition edge detectors (TES)[54] based on superconducting bolometers and close to 100% detection efficiency promises to solve this issue in the near future. A drawback there is that TESes require very low temperatures to operate (<100mK) and very sophisticated electronics is necessary to operate and read out this type of detector.

In contrast to LOQC, nonlinear optics quantum computing (NLOQC) takes a different approach by directly using intrinsic nonlinearities to implement multiphoton interactions. NLOQC schemes have been proposed using different types of optical nonlinearities, including cross-Kerr coupling[57] and two-photon absorption[27]. Since then, more complete multimode analyses of the cross-Kerr NLOQC schemes suggest that they cannot in fact produce phase shifts large enough for NLOQC because of spectral correlations created between the interacting fields[76], but these difficulties can be circumvented in the related case of strong  $\chi^{(2)}$  interactions by carefully engineering the phase-matching conditions[53].

In this work, we introduce a general process –*coherent photon conversion* (CPC). We show that this is an extremely versatile process which provides a range of useful photonic QIP tools. Remarkably, this includes solving the mentioned three main obstacles for photonic quantum computing with a *single process*: by enabling high-quality heralded sources of multiphoton

states (scalable source of many single photons), enhancing robust and efficient single-photon detection and most importantly a novel deterministic two-qubit entangling gates can be realized by harnessing a new type of deterministic photon-photon-interaction provided by the CPC process.

CPC itself is based on an effective quadratic (three-wave mixing) nonlinearity which is created by pumping higher-order nonlinear interactions with one or more bright classical fields. In our proof-of-principle experiment we specifically use a  $\chi^{(3)}$  nonlinearity pumped by one strong pump field using a photonic crystal fiber (PCF). Such fibers have show high nonlinearities in experiments creating photon pairs with very high brightness[67, 4]. In those experiments the two degenerate input modes of the four-wave-mixing interaction are pumped by single laser realizing photon pair creation by spontaneous four-wave-mixing. The crucial experimental difference and novelty of our scheme is that we only pump *one* of the input modes of the four-wave-mixing interaction resulting in an effective  $\chi^{(2)}$  non-linearity for the remaining three modes.



## 3.2 Principles

In this chapter the basic concepts describing the general coherent photon conversion (CPC) process are laid out starting from introducing the general process for a  $k$ th-order nonlinearity with  $n$  quantum and  $m$  pump fields. This is followed by deriving the timing evolution for the here considered and implemented special case of a CPC interaction using a 3rd-order non-linearity with one pump and 3 quantum fields. It further includes a derivation of the approximate interaction strength for the parameters of our experiment. Following this, it will be explained how CPC in the deterministic regime can enable a number of very important building blocks in quantum information technologies. This includes optical quantum computing, whose three main open problems CPC offers to solve: scalable multi-photon sources, near unity detection efficiency and most importantly a deterministic photon-photon interaction enabling a deterministic two-qubit entangling gate. The last subsection is dedicated to spontaneous four-wave-mixing, which is important for an intermediate result in our measurements.

### 3.2.1 Coherent photon conversion

Nonlinear optics with classical (laser) fields is well known and studied extensively for many decades both theoretically and experimental. A more recent impact on the field of quantum optics has been using non-linear optics involving quantum fields with processes like spontaneous parametric down-conversion (SPDC) or spontaneous four-wave-mixing (SFWM) where pairs of (entangled) photons can be created as well single photon conversion based on sum frequency generation or four-wave mixing with two pumps, where single photons can be coherently converted between different wavelengths.

With CPC we now want to introduce a more general concept: Consider the nonlinear interaction of  $k$  different light fields mediated by a  $(k-1)$ -th order optical nonlinearity. Of these  $k$  light fields  $n$  fields are quantum fields and  $m$  strong classical pump fields ( $k=m+n$ ). The concept of " $nm$ -CPC" describes now the situation in which the  $m$  strong classical pump fields create an effective  $n$ th-order linearity for the  $n$  quantum fields. The strength of such an effective non-linearity can be controlled (and enhanced) with the  $m$  classical pumps. Such a scheme is very general and in fact would include the above mentioned processes like SPDC ( $n=2$ ,  $m=1$ ) or SFWM ( $n=2$ ,  $m=2$ ) as a special case. However, the first novel and non-trivial special case, which has very interesting special properties with a vast potential for application in quantum optics is the case with  $n=3$  and  $m=1$ . This special case – (3,1)-

CPC – is the one that is mostly concentrated on in the following and is therefore more simply referred to as "CPC".

The such considered CPC process is a four-wave mixing interaction created by a third-order non-linearity  $\chi^{(3)}$ . The fully quantized interaction Hamiltonian for the 4 non-degenerate modes is then given by:

$$H = \gamma ab^\dagger c^\dagger d + \gamma^* a^\dagger bcd^\dagger, \quad (3.1)$$

where  $\gamma$  is the strength of the interaction arising from the third-order ( $\chi^{(3)}$ ) nonlinearity of the medium. Mode d is now pumped by a strong, non-depleted laser field (pump laser) which can be treated classically. This leads to an interaction Hamiltonian that is an effective  $\chi^{(2)}$ -interaction, but with an interaction strength that can now be tuned and enhanced with intensity of the pump laser in mode d:

$$H = \tilde{\gamma} ab^\dagger c^\dagger + \tilde{\gamma}^* a^\dagger bc \quad (3.2)$$

where  $\tilde{\gamma} \propto \gamma E_p$ , the electric field strength of the pump.

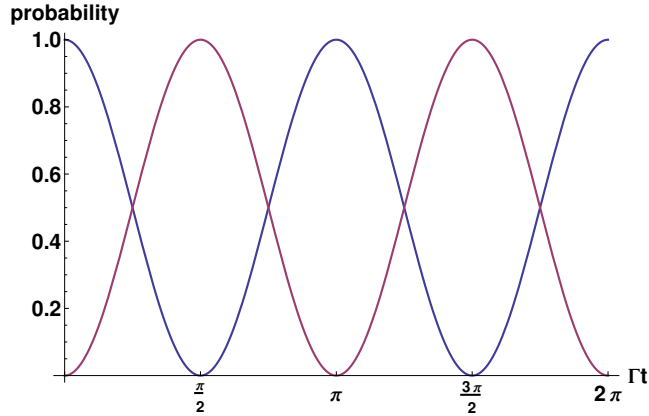


**Figure 3.1:** Timing evolution of the CPC-process according to equation 3.3 starting from the input state  $|100\rangle$ . It shows the resulting Rabi-like oscillations for the probabilities of the two basis states  $|100\rangle$  (blue curve) and  $|011\rangle$  (red curve) as a function of the interaction parameter  $\Gamma t$ .

To explain the basic CPC operation, here we use a simple single-mode “time-evolution” model where the modes satisfy energy conservation –  $\Delta\omega = \omega_a - \omega_b - \omega_c + \omega_d = 0$  – and we further assume for the moment perfect phase-matching. The key to understand the basic properties of the process is to look at its effect on input Fock states of the form  $|n_a n_b n_c\rangle$ . In particular, the

Hilbert space defined by the set of states  $H^j|n_a n_b n_c\rangle$  (for all  $j$ ) is a greatly restricted subspace of dimension  $(n_a + \min(n_b, n_c) + 1)$ . Consequently, if the quantum state starts in a product number state, it will evolve entirely within a finite subspace and will therefore exhibit the collapses and revivals in individual population elements which are characteristic of coherent quantum processes. The most important example of this for our scheme is the case which evolves within the two-dimensional subspace,  $\{|100\rangle, |011\rangle\}$  because  $H|100\rangle \propto |011\rangle$  and  $H^2|100\rangle \propto |100\rangle$ . Thus, the coupling induced by the Hamiltonian then drives Rabi-like oscillations between the two basis states. This can easily be seen by directly solving the Schroedinger equation. Given  $|100\rangle$  as an input, the output state then evolves as:

$$|\psi(t)\rangle = \cos(\Gamma t) |100\rangle + i \frac{\tilde{\gamma}}{|\tilde{\gamma}|} \sin(\Gamma t) |011\rangle, \quad (3.3)$$

where  $\Gamma = |\tilde{\gamma}|/\hbar$  and which is plotted in figure ???. There are two important characteristics of this evolution that are crucial to understand the potential CPC offers. First, for an interaction parameter of  $\pi/2$  starting from a single photon in mode a exactly 2 photons are created one each in mode b and c – which represents deterministic *photon doubling*. Second, starting the interaction with a input state of two photons one in each mode b and c  $|011\rangle$  will after a full oscillation ( $\Gamma t = \pi$ ) yield the state  $-|011\rangle$ . A Berry like phase of “-” is acquired! This represents a novel type of *deterministic photon-photon interaction* and enables a deterministic two-qubit entangling gate. The full implications and usefulness of this will now in detailed be explained in the following subsection.

### 3.2.2 Applications of efficient CPC

#### Deterministic entangling gates and photon doubling

The DiVincenzo criteria describe the basic conditions for a viable implementation of quantum computing[19]. For photonic quantum information processing there are three main unresolved challenges: good multi-photon sources, reliable multi-qubit interactions, and robust, high-efficiency single-photon detection. We show here that CPC provides tools to solve all three of these issues with a single process (figures 3.2 and 3.4) just by choosing different interaction strengths.

Figure 3.2a illustrates how CPC directly implements a two-qubit controlled-Z (CZ) gate between the photons in the two modes  $b$  and  $c$ . The key insight is that CPC, like any coherent process which cycles between two orthogonal

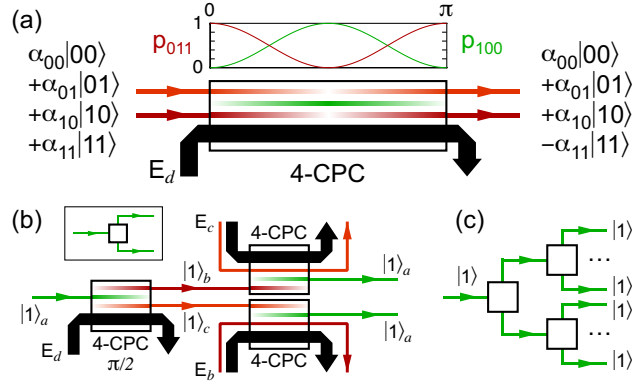


**Figure 3.2:** Solving the DiVincenzo criteria with 4-CPC. (a) Deterministic controlled-phase gate. A “ $\pi$ ” CPC interaction implements an entangling CZ gate between two logical states of frequency non-degenerate photons (e.g., polarisation or spatial encoding). (b) Scalable, deterministic photon doubler. A “ $\pi/2$ ” CPC interaction ( $\tau=\pi/2\Gamma$ ) can be used both to convert any single-photon source into a good source of multiphoton states and to perform high-efficiency, low-noise detection at any wavelength. (c) Deterministic photon doubling cascade. The scalable photon doubler from (b) (depicted by the symbol shown in the inset) can be directly chained to create a deterministic cascade for either multiphoton state preparation or detection enhancement.

states, exhibits geometric (Berry’s) phase effects[9] (cf. the all-optical switch demonstrated in Ref.[84]). Therefore, for  $t = \pi/\Gamma$ , an input state  $|011\rangle$  will undergo a full oscillation and pick up a  $\pi$  phase shift, giving the final state  $-|011\rangle$ . Because this phase shift only occurs when *two* single photons are present, this *controlled* phase shift can be used to implement a maximally entangling CZ gate with 100% efficiency. Note that this is a truly non-classical geometric phase which has no equivalent with classical input states. This CZ gate can also be switched very fast optically (by switching the bright classical pump beam in and out, cf.[84]), allowing the fast, real-time “rewiring” of optical quantum circuits. This may have application in various adaptive quantum schemes such as quantum phase estimation or adaptive quantum algorithms and might be particularly useful in wave-guide and integrated-optics architectures.

The second important case is, when the input undergoes exactly half an oscillation ( $t = \pi/2\Gamma$ ). Then a single photon is converted *coherently and*

*deterministically* (i.e. with 100% efficiency) into two single photons: a deterministic photon doubler[43]. Note that this can be also used in the reverse direction as deterministic two-photon absorber. Figure 3.2b illustrates one method for implementing a scalable photon doubler, allowing them to be chained together to create an arbitrary number of photons. This efficient photon doubling cascade (Fig. 3.2c) can be used to create a good source of multi-photon states from any source of genuine single photons (on-demand or heralded). Also note that the photon doubler can be used in conjunction with existing methods to create arbitrary, heralded (perhaps also non-locally prepared) entangled Bell-type two-photon and GHZ-type three-photon states. Indeed, these tools can be used directly to perform the encoding step for a simple 9-qubit error-correction scheme[78].

### Efficient detectors

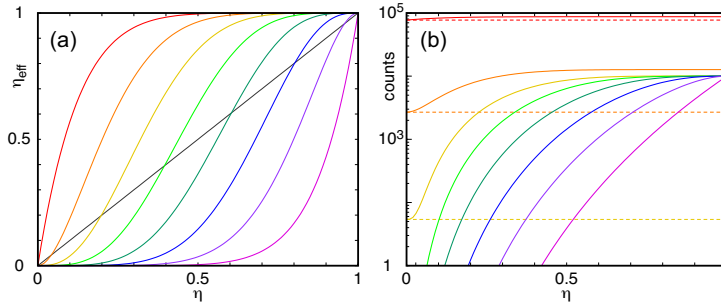


**Figure 3.3:** Efficient detection via a photon-doubling cascade. (a) Effective efficiency  $\eta_{eff}$  as a function of the individual detector efficiency  $\eta$  for a detector cascade with 3 cascade steps ( $n=8$  output photons) and a  $k$ -fold coincidences. It is plotted for different  $k$  between  $k=1$  (red) and  $k=8$  (violet). (b) Predicted counts for a simulated probabilistic experiment with  $10^6$  rep. rate,  $10^{-2}$  incident photon probability and  $10^{-2}$  (individual detector) dark count probability (i.e., SNR=1), using the same doubling cascade with  $n=8$  and  $k$ 's between 1 (red) and 8 (violet).

The idea to enhance single photon detection with CPC is relatively straight forward: Prior to the detection of the photon it is repeatedly doubled (in a cascade as in figure 3.2c). Then as many detectors as output modes can be employed with a greatly enhanced effective detection efficiency (at even enhanced signal to noise ratios, if coincidence detection of two or more de-

tectors is used). Figure ?? shows the effective detector efficiency for a 3-step cascade, which produces 8 ( $2^3$ ) photons, and various  $k$ . When  $k = 1$ , it is clear that the detector efficiency can be greatly increased, although there is naturally some trade-off when coincidence detection is used to suppress the dark counts. Figure ?? illustrates how this scheme would improve both count rates and signal-to-noise ratio in an example where the single-detector dark counts are as large as the signal. Interestingly, without using coincidence detection to suppress it, the effective dark count noise is actually higher for the cascade than for an individual detector. This effect is quite obvious in the example shown, because we deliberately chose an extremely high dark count rate, but it is already overcome with  $k=2$  only. In many cases, however, the raw dark count probability is much less than the signal rate and this effect is not significant.

### Scaling up for multi-photon sources

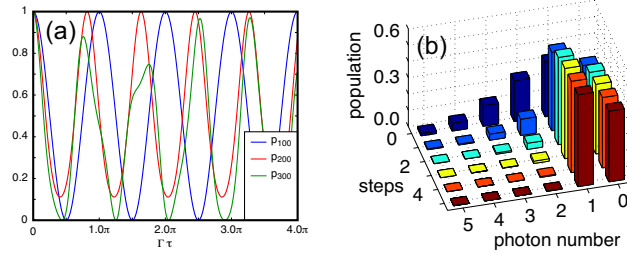


**Figure 3.4:** Heralded single-photon source. (a) Evolution of  $|n_a 00\rangle$  populations under the CPC interaction for  $n_a=1, 2$  &  $3$ . (b) Number-state populations after each filtering step for  $t=\pi/\Gamma$ , giving  $|1\rangle_a$ . Combined with a single photon-doubling step and given only a weak coherent state with  $|\alpha|^2 = 1.5$  as input, this scheme gives a heralded single-photon source with heralding efficiencies of  $\sim 56\%$  and virtually no higher-order photon-number terms ( $<0.3\%$ ) in only 5 steps.

In order to achieve scalable operation, we need a small number of basic units which can be simply connected together in an appropriately designed network. For example, the wavelengths of the photons at the outputs of each unit should be compatible with the input modes of the next unit. Here, we suggest two different approaches to achieve this goal. Both methods use entirely processes that use the same type of CPC interaction and can in principle be made 100% efficient. Finally, both methods can also operate

with four near-degenerate frequency modes and are therefore compatible with the enormous standard telecommunications toolbox.

*Method 1* which is illustrated in Fig. 3.2(a), builds the photon-doubling units from two stages, both of which utilise the same CPC interaction. The first stage uses the basic CPC interaction to take a single photon at  $\omega_a$  and creates single photons at  $\omega_b$  and  $\omega_c$ . The next stage modifies the same interaction simply by adding an extra pump beam at either  $\omega_b$  or  $\omega_c$ , thus creating a process which implements single-photon frequency conversion between the remaining mode ( $c$  or  $b$ ) and the original mode,  $a$ . Thus, using the same CPC interaction and the same high-power pump at  $\omega_d$ , with the addition of two relatively low-power pumps at  $\omega_b$  and  $\omega_c$ , the output photons from the photon doubler can be individually converted back into photons at the original frequency,  $\omega_a$ . The required resources for this process scale linearly with the number of output photons (one CPC photon doubler and two CPC frequency converters per extra photon). The controlled-phase gate illustrated in Fig. 3.2(b), which takes input photons at frequencies  $\omega_b$  and  $\omega_c$ , can be modified in a similar way using frequency conversion to build a unit which implements a controlled-phase gate between input photons at  $\omega_a$ . Of course, in any network of such units, a number of these frequency conversion stages will be able to be avoided to minimise the total number of nonlinear interaction steps used.

*Method 2* takes a slightly different approach (Fig. 3.5). So far, we have considered only the CPC process involving four distinct frequency modes (described by the Hamiltonians  $H = \gamma ab^\dagger c^\dagger d^\dagger + \gamma^* a^\dagger bcd$  or  $H = \gamma ab^\dagger c^\dagger d + \gamma^* a^\dagger bcd^\dagger$ ), but it is also possible to implement a special case of this process when the two modes  $b$  and  $c$  have the same frequency (i.e. they are completely *indistinguishable* modes). In this case, the full Hamiltonian is, e.g.,  $H = \gamma ab^{\dagger 2} d + \gamma^* a^\dagger b^2 d^\dagger$ , and when mode  $d$  is pumped by a bright classical laser beam,  $E$ , the effective Hamiltonian reduces to  $H = \tilde{\gamma} ab^{\dagger 2} + \tilde{\gamma}^* a^\dagger b^2$ . This modified form of CPC also implements a photon doubling process, but takes a single-photon input at  $\omega_a$  and produces a two-photon Fock-state in  $\omega_b$ . Then, by embedding this in two arms of an interferometer, the two degenerate and indistinguishable photons can be deterministically separated into different modes via a ‘‘reverse Hong-Ou-Mandel’’-type interaction at a beam splitter ( $|2, 0\rangle + |0, 2\rangle \rightarrow |1, 1\rangle$ ). Each of these photons (at  $\omega_b$ ) can then in turn be converted in a similar way into two photons at  $\omega_a$  using the same CPC interaction with a different high-power pump frequency. By alternating between these two processes, the photon doubling cascade can therefore be scaled up to larger systems. As with Method 1, this approach is built using units with the same type of CPC interaction, this time simply with two different pump frequencies. Once

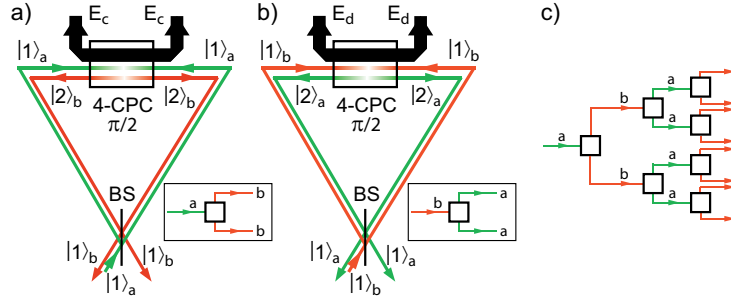


**Figure 3.5:** Method 2: a) Doubling of mode  $a$  into two photons in the degenerate mode  $b$ . The separation of the two photons into different modes is achieved via a “reverse Hong-Ou-Mandel”-type interaction at a beam splitter ( $|2, 0\rangle + |0, 2\rangle \rightarrow |1, 1\rangle$ ). With the pump field  $E_c$  energy conservation is given by  $\omega_a + \omega_c = 2\omega_b$ . b) Analogue doubling but with modes  $a$  and  $b$  swap their roles with now mode  $a$  being degenerate. With a different pump field  $E_d$  Now energy conservation is given by  $\omega_b + \omega_d = 2\omega_a$ . c) Cascaded concatenation of a) and b) to achieve scaling up to high number of photons.

again, this scaled process requires only linear resources to create  $n$ -photon states (three CPC photon doublers per extra 3 photons).

### Entanglement sources

The cascaded photon-doubling technique for efficiently generating multi-photon states is not limited to generating simple pure product states. Figures 3.6(a) and 3.6(b) illustrate CPC circuits for generating both bipartite and genuine tripartite entanglement. For example, if two polarisation states of an input single photon are split up in a polarisation-sensitive interferometer (e.g., a Mach-Zender interferometer using polarising beam displacers, or a Sagnac loop) and if a photon doubling interaction is applied to both polarisations, then the same process can be used as a source of polarisation-entangled photons [Fig. 3.6(a)]. The same result could also be achieved using a “crystal-sandwich” arrangement. Existing experiments have already repeatedly demonstrated that these techniques produce extremely high-quality entanglement with spontaneous parametric down-conversion. Note that, by tuning the polarisation of the input single photon, we can generate different (both maximally and non-maximally) entangled states. These states can even be prepared non-locally [Fig. 3.6(c)]. Finally, Fig. 3.6(d) illustrates



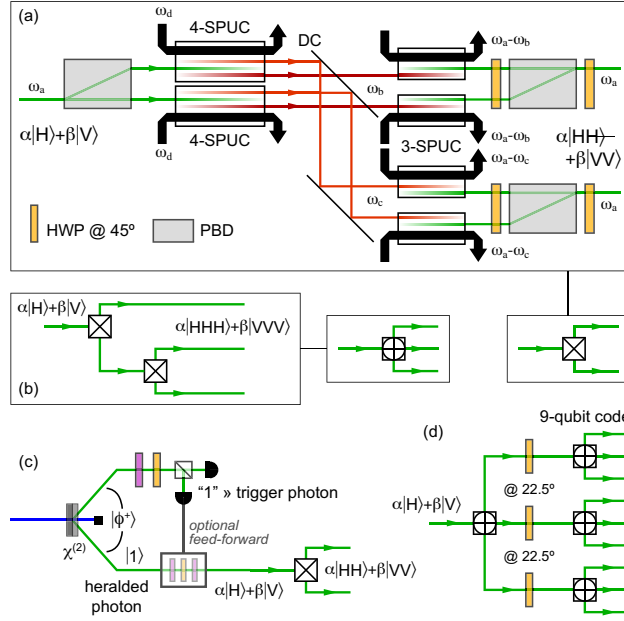


**Figure 3.6:** CPC circuits for creating (a) bipartite and (b) tripartite entanglement. (c) A CPC circuit for generating arbitrary, non-locally prepared, non-maximally entangled states. (d) A direct implementation of the error-correction encoding step for a simple 9-qubit code.

how these basic building blocks can be combined to directly implement the encoding step of an error-correction protocol using a simple 9-qubit code.

### Higher-order applications: Fock-state preparation

Table 3.1 shows interaction lengths and target-state transmission probabilities for some early “revival” peaks from different photon-number input states, which have the potential to be used for Fock-state filtration. Because of the complexity of higher-order eigenvalues, longer interactions are generally required before a significant revival occurs, which is even then generally not 100% efficient. This lowers the success probability of the Fock-state preparation for higher-order states, but for lower orders, quite pure Fock states can be prepared non-deterministically with relatively few interaction steps and quite high probability. For example, as mentioned in the main text, with  $\sim 56\%$  probability, a single-photon state can be prepared with fidelity and purity greater than 99.6% using a weak coherent input state ( $|\alpha|^2 = 1.5$ ) with only 5 steps [Fig. 3.4(b)].

target state	interaction $\Gamma\tau (\times\pi)$	target transmission
$ 1\rangle$	1	1.000
$ 2\rangle$	$2/\sqrt{6}$	1.000
$ 3\rangle$	5.805	$> 0.9998$
$ 4\rangle$	2.154	$> 0.9999$
$ 5\rangle$	21.278	$> 0.990$
$ 6\rangle$	11.100	$> 0.996$
$ 7\rangle$	9.390 68.972	$> 0.986$ $> 0.995$
$ 8\rangle$	20.024	$> 0.93$

**Table 3.1:** Revival peaks for higher-order input states.

### Higher-order applications: better down-conversion

We now briefly outline how the CPC interaction can be used to implement a “better” form of down-conversion. Specifically, consider an input state to mode  $a$  that contains higher-order Fock states, such as a weak coherent state or the heralded single-photon state created by triggering from a down-conversion pair, and assume that the interaction time corresponds to an integral number of complete oscillations of the  $|200\rangle$  input state (i.e.,  $\Gamma\tau=2m\pi/\sqrt{6}$ ). In such a situation, the  $|100\rangle$  term will have converted to  $|011\rangle$  with some finite probability, but the  $|200\rangle$  will have remained unconverted with 100% probability, allowing the creation of correlated “down-conversion-like” photon pairs, with no  $|022\rangle$  term. Figure 3.7 shows the output of this process after each of the first three  $|200\rangle$  oscillation periods, given weak coherent input states with a range of average photon numbers. For both two and three periods [Figs 3.7(b,c)], the CPC process produces substantially higher pair-emission probabilities with much higher fidelity than a standard down-conversion source with comparable emission rates. This technique can also provide improved higher-order characteristics using a heralded single photon from standard down-conversion as the input.

### 3.2.3 Coherent photon conversion efficiency

In the following calculation we aim at theoretically estimating the interaction strength of our target four-wave-mixing process for a range of experimental parameters. We start with an ansatz similar to [4], that relates the interaction Hamiltonian of the four-wave-mixing process to the  $\chi^{(3)}$  non-linearity of the material and the energy density  $U$  associated with the four coupled fields  $E_p$ ,

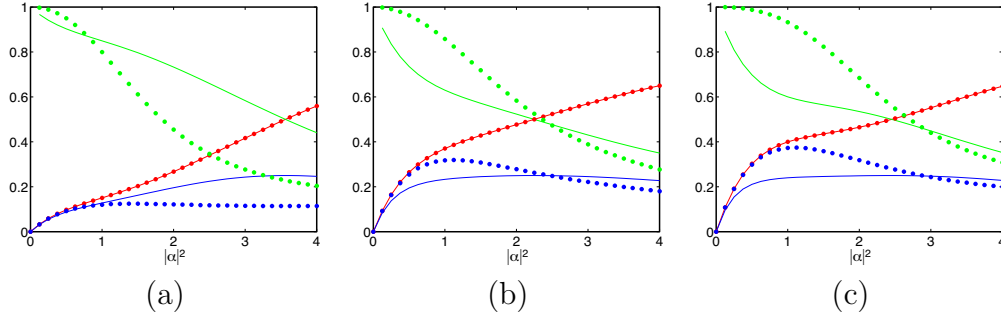


**Figure 3.7:** Better down-conversion using the CPC interaction. Overall one-pair detection probability per pulse (blue) and fidelity of a “heralded” state with the one-pair state (green) for a particular total photon-emission probability per pulse (red). Solid circles show the results for interaction times: (a)  $\Gamma\tau=2\pi/\sqrt{6}$ , (b)  $\Gamma\tau=4\pi/\sqrt{6}$  and (c)  $\Gamma\tau=6\pi/\sqrt{6}$ . For comparison, the lines show the results for standard down-conversion with the same herald detection probability.

$E_a$ ,  $E_b$ , and  $E_c$ .

From:

$$\hat{H} = \int dV \hat{U} \quad (3.4)$$

$$\hat{U} = \epsilon_0 \chi^{(3)} (\hat{E}_p \hat{E}_a \hat{E}_b \hat{E}_c + \text{h.c.}) \quad (3.5)$$

with  $\epsilon_0$  the vacuum permittivity and the integral taken over the quantization volume, it follows:

$$\hat{H} = \int dV (\epsilon_0 \chi^{(3)} \hat{E}_p \hat{E}_a \hat{E}_b \hat{E}_c + \text{h.c.}). \quad (3.6)$$

For the further derivation we now need to quantize the electric fields of all modes but the pump which is treated as a strong classical and undepleted field:

$$\hat{E}_i = \sqrt{\frac{\hbar\omega_i}{2\epsilon_0}} (\hat{a}_i^\dagger + \hat{a}_i) u_i(r) \quad (3.7)$$

Here  $\omega_i$  represents the optical frequency of the associated mode and  $\hat{a}_i^\dagger$  and  $\hat{a}_i$  the respective creation and annihilation operators. The mode functions  $u_i$

need to be normalized by:

$$\int dV u(r)u^*(r) = \frac{1}{n_0} \quad (3.8)$$

where  $n_0$  is the refractive index of the medium the interaction takes place in. At this point we use an approximation for the mode functions of the interacting modes including the pump mode. We assume they are Gaussian wave packets with extensions given by the pulse duration  $\tau_p$  of our pump laser (6 ps) and the effective mode field diameter  $2w_0$  of our PCF (1.8  $\mu\text{m}$ ). As a further approximation we for the moment treat all of the modes as single spectral modes. We also approximate that the mode field diameters are the same for all modes, irrespective of their different wavelengths. The correctly normalized mode function for all modes can then be written (in cylindrical coordinates) as:

$$u(r, z) = c_N e^{-\frac{1}{2}\frac{r^2}{2w_0^2}} e^{-\frac{1}{2}\frac{z^2}{2l_0^2}} \quad (3.9)$$

$$c_N = (2\pi)^{-\frac{3}{4}} (w_0^2 l_0 n_0)^{-\frac{1}{2}} \quad (3.10)$$

The normalization constant was  $c_N$  determined by integration of the unnormalized  $u(r, z)$ . The pulse length  $l_0$  is given by  $2l_0 = \frac{n_0 \tau_p}{c}$ . After inserting everything into equation 3.6 and leaving out all terms with combinations of creation and annihilation operators that violate energy conservation ( $\omega_p + \omega_a = \omega_b + \omega_c$ ) we arrive at:

$$\hat{H} = \epsilon_0 \chi^{(3)} | E_p | \sqrt{\frac{\hbar\omega_a}{2\epsilon_0}} \sqrt{\frac{\hbar\omega_b}{2\epsilon_0}} \sqrt{\frac{\hbar\omega_c}{2\epsilon_0}} (\hat{a}_a \hat{a}_b^\dagger \hat{a}_c^\dagger + h.c.) \int dV c_N^4 u(\vec{r})^4 \quad (3.11)$$

The last integral can actually be evaluate for our approximated mode functions resulting in a "mode overlap factor"  $I_{MF}$  of:

$$I_{MF} = \int dV c_N^4 u(\vec{r})^4 = \frac{1}{8} \pi^{-\frac{3}{2}} \frac{1}{n_0 w_0^2 l_0} \quad (3.12)$$

The pulse length of 6 ps and the mode-field radius of 0.9  $\mu\text{m}$  of our PCF gives a value for this constant of  $I_{MF} \sim 9.1 \times 10^{-12} \text{m}^{-3}$ .

For the pulsed laser the classical electric field strength in a pulse is given by:

$$| E_p | = \sqrt{\frac{2P_{av}}{\tau_p R_{Rep} A_{eff} c \epsilon_0 n_0}} \quad (3.13)$$

which for our laser with  $\tau_p = 6$  ps and  $R_{Rep} = 76$  MHz at 1 W average power equals  $|E_p| = 3.3 \times 10^8 \frac{V}{m}$ .

For the wavelengths of the modes a, b and c of our four-wave-mixing process of 710 nm, 504 nm and 766 nm we can also evaluate the term:

$$\sqrt{\frac{\hbar\omega_a}{2\epsilon_0}} \sqrt{\frac{\hbar\omega_b}{2\epsilon_0}} \sqrt{\frac{\hbar\omega_c}{2\epsilon_0}} \approx 2.3 \times 10^{-12} V^{-\frac{1}{2}} m^{-2} \quad (3.14)$$

The value of  $\chi^{(3)}$  can be calculated from the more commonly used nonlinear refractive index  $n_2$  related to it by [4]:

$$n_2 = \frac{3\chi^{(3)}}{4\epsilon_0 c n_0^2} \quad (3.15)$$

$n_0$  is the refractive index and  $c$  the vacuum speed of light.

Using the value of  $n_2$  for silica of  $3.2 \times 10^{-20}$  [23]  $\chi^{(3)}$  has the value:

$$\chi^{(3)} = \frac{4}{3} n_2 \epsilon_0 n_0^2 = 4.78 \times 10^{-31} m^2 V^{-2} \quad (3.16)$$

Note that for other glasses, especially chalcogenide glasses, this value can be up to 3 orders of magnitude higher than that for silica [23].

We are now able to multiply all terms of equation 3.6 to arrive at the final value of  $\Gamma$  for the simplified Hamiltonian  $\hat{H} = \hbar\Gamma(\hat{a}_a\hat{a}_b^\dagger\hat{a}_c^\dagger + h.c.)$  for 1 W of average pump power:

$$\Gamma = \frac{1}{\hbar} \epsilon_0 |E_p| \sqrt{\frac{\hbar\omega_a}{2\epsilon_0}} \sqrt{\frac{\hbar\omega_b}{2\epsilon_0}} \sqrt{\frac{\hbar\omega_c}{2\epsilon_0}} I_{MF} = 273 \text{ s}^{-1} \quad (3.17)$$

This final interaction parameter  $\Gamma t$  can now be calculated from the interaction time given by  $t = \frac{L}{c} = 2.5 \text{ ns}$  for the fiber length  $L$  of 0.5 m:

$$\Gamma t = 6.8 \times 10^{-7} \quad (3.18)$$

At this point we like to stress, that the approximation that allowed the relatively easy calculation of the interaction strength is strictly only valid, when the output bandwidth given by the phase-matching is so narrow that it is effectively monochromatic. However, realistically the phase-matching in our PCF allows a much broader bandwidth - or in other words a big number of different monochromatic output modes. This will in practice result in a significant enhancement of the interaction parameter, because all these spectral modes contribute to the final interaction strength.

In order to find an approximate estimate of this enhancement factor we first calculate the bandwidth  $\Delta\nu_0$  of one quasi-monochromatic mode given by our fiber length of  $L = 0.5$  m:

$$\Delta\nu_0 = \frac{c}{n_0 L} \sim 400 \text{ MHz} \quad (3.19)$$

From the phase matching calculation for the fiber we get a bandwidth  $\Delta\nu_{phm}$  of around 500 GHz for the used fiber length (0.5 m). The ratio of these two bandwidths should now give us an effective number of spectral output modes  $N_{sp}$ :

$$N_{sp} = \frac{\Delta\nu_{phm}}{\Delta\nu_0} = 1.2 \times 10^3 \quad (3.20)$$

Note that this number does not depend on the fiber length  $L$ . This is because both  $\Delta\nu_{phm}$  and  $\Delta\nu_0$  depend inversely linear on  $L$ , so that it cancels out. Therefore  $N_{sp}$  is given solely by the dispersion properties of the fiber and the resulting phase matching conditions that determine the output mode's bandwidths.

Taking this enhancement factor now into account we arrive at our final theoretical estimate of the interaction parameter in our PCF for 1 W of average pump power:

$$(\Gamma t)_{enhanced} = 8.2 \times 10^{-4} \quad (3.21)$$

This estimate does not consider any effects stemming from the finite bandwidth of the pump laser. Also other effects like temporal walk-off due to different group velocities of the involved modes are not included. However, because we use a cw laser as the second input and in the regime of low interaction strength the resulting corrections – at least for the latter effect – should be small. In general, in future more detailed theoretical calculations one could fully decompose all modes into their monochromatic spectral components – similar to the calculation in [4] – including taking into account the specific phase-matching conditions, walk-off effects and pump pulse shape. However, such a calculation is beyond the scope of this current analysis for the first proof-of-principle experiment demonstrating the feasibility of our specific four-wave-mixing process.

### 3.2.4 Pair creation from four-wave mixing

The generation of photon pairs, that is typically achieved by spontaneous parametric down-conversion, is also possible in materials with third order non-linearities. Using such spontaneous four-wave-mixing (SFWM) processes for pair-creation – for example in silica glass fibers – has gained recent attention, due to its potentially high brightness and flexibility in addition to the advantage of the possibility for using standard optical fibers as the non-linear medium [4, 67].

The SFWM process can be described (in a full quantum treatment) by the following interaction Hamiltonian for the degenerate pump mode  $p$  and the two modes 1 and 2 that obey energy conservation ( $2\omega_p = \omega_1 + \omega_2$ ) and are phase-matched for this interaction:

$$\hat{H}_i = \gamma(\hat{a}_p\hat{a}_p\hat{a}_1^\dagger\hat{a}_2^\dagger + \hat{a}_p^\dagger\hat{a}_p^\dagger\hat{a}_1\hat{a}_2) \quad (3.22)$$

The strength of the interaction  $\gamma$  is proportional to the  $\chi^{(3)}$  nonlinearity as well as dependent on other constants and conditions (see section on coherent photon conversion efficiency 3.2.3).

Assuming a bright classical and non-depleted pump field the effective Hamiltonian can be written as:

$$\hat{H}_i = \tilde{\gamma}E_p^2(\hat{a}_1^\dagger\hat{a}_2^\dagger + \hat{a}_1\hat{a}_2) \quad (3.23)$$

Note that the only difference to the effective Hamiltonian for  $\chi^{(2)}$ -based SPDC is that the interaction strength does not any more scale linear with the pump electric field strength but quadratically.

The output of this interaction acting on the vacuum is the well-known two mode squeezed vacuum. It can be derived in the photon number basis explicitly [29]:

$$|\psi\rangle = \frac{1}{\cosh(r)} \sum_{n=0}^{\infty} (-1)^n e^{in\theta} (\tanh(r))^n |n, n\rangle \quad (3.24)$$

with  $r$  scaling quadratically with the pump electric field (linear for SPDC). This is an exact solution for an non-depleted classical pump field and is normalised for all  $r$ .

The  $r$ -parameter is linear proportional to the pump power  $P_{pump}$  (and to the  $\sqrt{P_{pump}}$  for SPDC) and given by:

$$r = \frac{\tilde{\gamma}}{\hbar} E_p^2 = \kappa P_{pump} \quad (3.25)$$

with  $\kappa$  being the product of all constants and parameters including  $\tilde{\gamma}$  – but also for example the pulse length and repetition rate of the pump laser which are parameter that relate  $E_p$  to the pump power.

There are some interesting features of the two mode squeezed vacuum state, that rarely mentioned in text books or publications, which is why they are pointed out here:

Firstly, the probability for creating a single photon pair  $|1, 1\rangle$  is straightforwardly given from equ. 3.24 by:  $P_{11} = (\tanh(r)/\cosh(r))^2$ . It has its maximum of 0.25 at  $r=1$  decreasing exponentially for large  $r$ 's with higher-order terms dominating. This means the probability the create a *single* pair per pump pulse can in general not be bigger that 25% for either SFWM and SPDC.

Secondly, using equ. 3.24 the overall mean photon number (including all higher order contributions) in one mode can be calculated to be:  $\langle \hat{n} \rangle_1 = \langle \hat{n}_2 \rangle = \sinh^2(r)$ [29]. This has two interesting limits: for  $r \ll 1$  – where the dominating contribution are single pairs of photons – the number of these pairs scales quadratically with  $r$  (and linear for SPDC). That means for the SFWM process scales quadratically with the pump power (compared to linear in the case of SPDC). However, for  $r \gg 1$  the  $\sinh^2(r)$  is asymptotically equal to  $\frac{1}{4}e^{2r}$ . This means an exponential increase of the intensity in the modes with the pump power. Correspondingly for SPDC there is an increase with the exponential of the square root of the pump power. Summing up all these cases gives the following relations:

$$SPDC(r \ll 1) : \langle \hat{n}_i \rangle \propto P_{pump} \quad (3.26)$$

$$SFWM(r \ll 1) : \langle \hat{n}_i \rangle \propto P_{pump}^2 \quad (3.27)$$

$$SPDC(r \gg 1) : \langle \hat{n}_i \rangle \propto e^{2\sqrt{\kappa P_{pump}}} \quad (3.28)$$

$$SFWM(r \gg 1) : \langle \hat{n}_i \rangle \propto e^{2\kappa P_{pump}} \quad (3.29)$$

$$(3.30)$$

We could not find any reference where this exponential regime has been directly observed and analysed for neither SPDC nor SFWM experiments. However, it is the working principle for a so called optical parametric generator (which is an optical parametric oscillator without any enhancement cavity). There, by using very high peak pump powers even a regime is reached, where the pump field starts to be depleted and also loss effects start to influence the dynamics of the interaction.

Yet another interesting feature of the two-mode squeezed vacuum state is



the photon statistics of its modes. When only one of the modes is considered (with the other mode traced out) one can show, that it will always have a thermal distribution. To illustrate this one can for example calculate the second order correlation function ( $g^{(2)}(0)$ ) which is given by:

$$g^{(2)}(0) = \frac{\langle \hat{a}_i^\dagger \hat{a}_i^\dagger \hat{a}_i \hat{a}_i \rangle}{\langle \hat{a}_i^\dagger \hat{a}_i \rangle \langle \hat{a}_i^\dagger \hat{a}_i \rangle} \quad (3.31)$$

Applied to equ. 3.24 with the creation and annihilation operators yielding the corresponding factors gives:

$$g^{(2)}(0) = \frac{1}{\cosh^2(r) \sinh^4(r)} \sum_{n=0}^{\infty} n(n-1) (\tanh(r))^{(2n)} = 2 \quad (3.32)$$

This means that irrespective of  $r$  – even for  $r \gg 1$  – the photon statistics will show photon bunching with the thermal value for  $g^{(2)}(0)$  of 2.

### 3.3 Experimental Setup

In this section the experimental setup and experimental tools are described that are used for a proof-of-principle experiment for CPC. Starting from an overview of the setup with the different building blocks (lasers, input beam combining, nonlinear fiber, output analysis stage) the following subsection is then dedicated to details about the nonlinear fiber and its phase-matching properties.

#### 3.3.1 Coherent photon conversion setup

The objective of our experiment is to demonstrate the four-mode interaction that underlies the CPC process using a silica photonic crystal fiber (PCF) as the  $\chi^{(3)}$  nonlinear medium. This includes verifying the spectral and polarization properties that are expected theoretically for the process. It further aims at quantitatively characterising the interaction strength that is experimentally reached and show its linear scaling with the pump power.

The experimental setup consists of different building blocks. An overview of the setup can be seen in figure 3.8. Our pump wavelength is 532 nm which is provided by a frequency-doubled pulsed neodymium vanadate laser with a pulse length of 7.5 ps and a repetition rate of 76 MHz. The second input for the CPC process – the probe laser whose photons are doubled into one photon in each of the output modes – has a wavelength of 710 nm. We used a self-build fiber-coupled external cavity diode laser with a cw average power of up to around 10 mW.

The choice of these wavelengths was partly due to the availability of a strong pump laser at 532 nm. But more importantly, by in detail studying the phasematching solutions that are possible for our specific PCF (see 3.3.2) and choosing 710 nm as the probe wavelength, we could achieve wavelengths for the output modes that as far as possible away from the strong pump laser at 532 nm. This is essential to reduce Raman scattering induced by the strong pump field that would otherwise inevitably swamp any signal from the actual CPC process.

After the input lasers, the next stage of the experimental setup is combining and coupling them into the PFC and also controlling their polarization state (see beam prep. in figure 3.8). One challenge to couple high optical power into a PCF is to avoid burning the facets of the fiber. Because the mode coming directly from the 532 nm is not optimal we spatially filtered it by coupling it through a SM fiber, which acts as a good Gaussian mode filter.

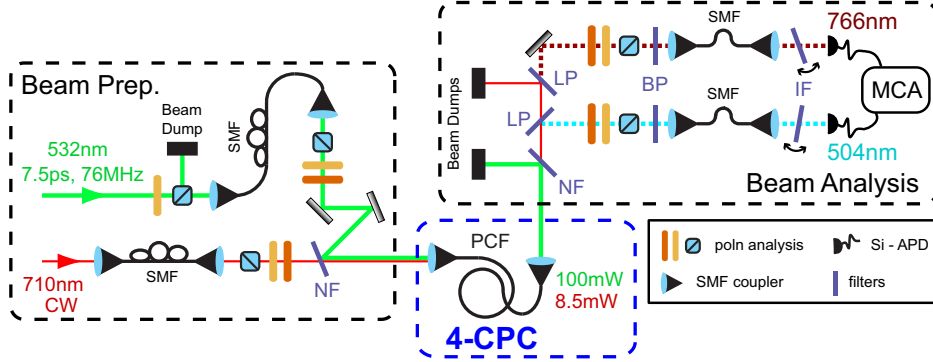


**Figure 3.8:** Schematic of the experiment. The nonlinear medium is a commercial polarisation-maintaining photonic crystal fibre (PCF) ( $1.8 \mu\text{m}$  core, nonlinearity  $\sim 95 (\text{W km})^{-1}$ ). The  $\chi^{(3)}$  nonlinearity is pumped by a frequency-doubled pulsed neodymium vanadate laser (Nd:YVO<sub>4</sub>: 532 nm, 7.5 ps, 76 MHz) to create the desired tunable effective  $\chi^{(2)}$  nonlinearity. A continuous-wave (cw), external-cavity diode laser (710 nm,  $\sim 2 \times 10^5$  photons per pulse) provides the input state in mode  $a$  which we use to characterise the strength of the 4-CPC interaction. From the estimated dispersion for the PCF, birefringent phase matching is satisfied for the following four-mode interaction: 532 nm (H) + 710 nm (H)  $\rightarrow$  504 nm (V) + 766 nm (V), where H denotes horizontal and V vertical polarization. The 532 nm and 710 nm input beams are spatially filtered with single-mode fibres (SMF) before being combined on a notch filter (NF) and coupled into the PCF. The beams emerging from the output are then spectrally separated using a range of filters (NF, LP: long-pass, BP: band-pass) and a tunable spectral filter (a rotating interference filter, IF), passed through polarisation analysers, and finally analysed in coincidence using time-to-amplitude conversion and a multichannel analyser (MCA).

With this we achieved high coupling efficiencies into the PFC exceeding 80% for the strong pump beam. Nevertheless, over time we did observe degradation of the fiber facets – especially for the mode filtering SM fiber, which burned so much that we had to replace this fiber after an effective running time for the experiment of couple of days. Combining the input lasers was achieved with a notch filter (NF), that reflects (a narrow band around) 532 nm and transmits the 710 nm beam. Polarization control was achieved with fiber polarization controllers for the SM fibers that connect the lasers with

the setup as well as with polarizers and wave-plates directly before the NF. The nonlinear medium in which the interaction takes place was a glass (silica) photonic crystal fiber. It is the central element of our experiment and is therefore separately described in more detail (including phasematching) in the next subsection.

The final building block of our experiment is the beam analysis stage (see figure 3.8). Its purpose is to separate and filter the two output modes at 504 nm and 766 nm and suppress any noise photons coming either from the input lasers themselves or from induced broad-band Raman scattering inside the PCF. The filtering and separation of the modes was accomplished with various spectral filters – notch filters, long-pass and short-pass filters as well as bandpass filters. Importantly we employed as the last step of filtering two tunable, relatively narrow band (around 3 nm FWHM) interference filters. The tunability was achieved by mounting those on tilting mirror mounts with micro-meter actuators. Once calibrated with a white light source and a spectrometer the central wavelengths of the filters could then be precisely set (with an accuracy of around 0.2 nm) to the desired value or controllably tuned for spectral measurements. The polarization of the output modes was analyzed with combinations of polarizers and waveplates. This is crucial, because due to the birefringent phasematching pairs are generated only for the right output polarizations (vertical for both output modes) which we confirmed in the experiment.

Finally, the two output modes are coupled into multimode fibers and detected with single photon detectors based on silicon avalanche photon diodes (Si-APDs, PerkinElmer). We aim at demonstrating the generation of photon pairs by the 4 mode interaction of our process – doubling of 710 nm photons into two photons with one in each of the output modes. Therefore, we need to analyze the (relative) timing of the photon detections for both output modes. For this purpose we used a high timing resolution time-to-amplitude-converter (TAC, Canberra) that generates voltage pulses proportional to the time-differences of two detection events for both modes. The distribution of the heights of these pulses (and therefore time-differences) was then recorded with a digital multi-channel analyzer (Toivel) that was connected to a computer via USB. We then identified the coincidences arising from the generated pairs as a sharp peak in the resulting histograms which allowed us to also quantify the number (rate) of coincidences by further analysing these histograms (see section on experimental results 3.4)

### 3.3.2 Photonic crystal fibers and phase-matching

The nonlinear medium used in our experiments is a glass (silica) photonic crystal fiber. Normally glass does not have a particularly high intrinsic third order nonlinearity. However, by using an optical fiber and making its mode-field area very small high effective nonlinearities can be achieved. A way to manufacture such fibers with very small mode field area is by making the lower refractive index cladding around the core out of tiny holes with air. This type of fiber is called photonic crystal fiber (sometimes also "holey fibers") and their manufacturing has been optimised and made commercially available in the last decade.

The specific photonic crystal fiber used in our experiments is a polarization maintaining, highly nonlinear PCF with a zero dispersion wave length at 750 nm and a very small mode field diameter of around 1.8  $\mu\text{m}$ . The fiber is commercially available from NKT Photonics (NL-PM-750). The use of a polarization maintaining fiber has the big advantage that there are phase matching solutions (birefringent phasematching) with a big separation for all the interacting wavelength, which can in this form not be achieved with normal, non-polarization maintaining fibers. A wide separation of the interacting wavelengths in general makes it easier to combine and separate the different modes. More importantly, Raman scattering in silicon induced by the strong pump laser has its maximum around 12 THz away from the pump and extends up to approximately 40 THz frequency separation. This means, that for the phase-matched output wavelengths being more than 40 THz away from the pump has significant advantages regarding unwanted background noise.

For the process where the one input mode  $k_i$  is converted into two modes  $k_1$  and  $k_2$  (photon-doubled) induced and amplified by a strong pump laser  $k_p$  the phase-matching condition is given by:

$$k_1 + k_2 - k_i - k_p + \gamma P_p = 0. \quad (3.33)$$

The last term of the left hand side describes the cross-phase modulation induced by the strong pump field with optical power  $P_p$  and depends on the non-linear coefficient in the fiber  $\gamma = \frac{2\pi n_2}{\lambda_p A_{eff}}$ .  $A_{eff}$  denotes the effective mode field area of the fiber,  $\lambda_p$  the pump wavelength and  $n_2$  is the non-linear refractive index of the material used – in our case silica with  $n_2 = 2 \times 10^{-20} \text{m}^2/\text{W}$ . However, at the moderate pump powers below 200 W peak power, the correction this gives for the phase-matching condition is rather

small.

Of course also energy conservation of the interacting modes needs to be preserved as well:

$$\omega_1 + \omega_2 - \omega_{in} - \omega_p = 0 \quad (3.34)$$

The last missing ingredient to calculate at which wavelengths at which the process is phase-matched is the dispersion in the fiber for the different polarization modes. Fortunately, the company our PCF was bought from could provide us with dispersion data of the fiber which is plotted in figure ??.

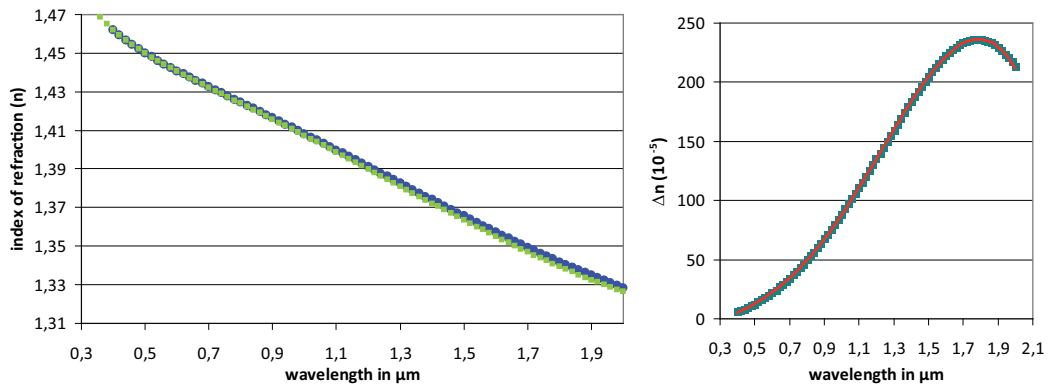


**Figure 3.9:** Dispersion data of the PCF (NL-PM-750) provided by the manufacturer. The left plot shows the index of refraction  $n_o$  and  $n_e$  for the two different polarization modes (green and blue). The right plot shows the difference of the two with a polynomial fit (red solid line)

For a convenient incorporation of the dispersion data into the phase-matching calculations polynomial fits (4th order) to the data for  $n_o$  and  $\Delta n$  were made giving in total 10 parameters that describe the dispersion of our fiber for both polarization modes.

The main aim of the phase-matching calculation was then to correctly predict the wavelength of the photon pairs produced with our pump wavelength of 532 nm and input wavelength of 710 nm. This can be achieved by numerically determine the wavelength pair  $\lambda_1$  and  $\lambda_2$  that fulfils both energy conservation (equ. 3.3.2) and phasematching (equ. 3.3.2). The resulting predicted the wavelengths are:  $\lambda_1 = 507.9$  and  $\lambda_2 = 757.5$ . However, these predictions are highly sensitive on the precision of the dispersion data – a couple of percent difference in  $\Delta n$  would lead to a shift of several nanometers.

Fortunately, we were able to observe another phase-matched process in our PCF – namely pair creation from spontaneous four-wave-mixing (see principles and results section). The process was very bright – even entering the exponential gain regime – so that we could precisely measure (with a sensitive spectrometer) the wavelength of one of the created modes to be 490.5 nm. The theoretically expected wavelengths from the phasematching calculation would have been 495 nm. By comparing the predicted wavelength to the observed we were able to "calibrate" our calculation by slightly modifying the dispersion data by adding a constant of  $4.1 \times 10^{-5}$  to  $\Delta n$ . We estimate that such a small error in the dispersion data – that was given to us by the company – is not unlikely. Using this procedure we were able to predict the wavelengths of the four-wave-mixing process to be:  $\lambda_1 = 504.8$  and  $\lambda_2 = 764.6$ . This is quite close to the actually observed wavelengths at  $\lambda_1 = 503.7$  and  $\lambda_2 = 765.7$  (see results) in contrast to the values from the uncorrected dispersion data above.

In conclusion, we were able to accurately predict the central wavelengths of the desired process with the phase-matching calculation based on adapted dispersion data for the used fiber. In general, this calculations appears to be crucially sensitive on the precision of the input data for the dispersion, which highlights the high requirements, when trying to actively design dispersion properties of PCFs.

## 3.4 Results

### 3.4.1 Pair creation in the PFC

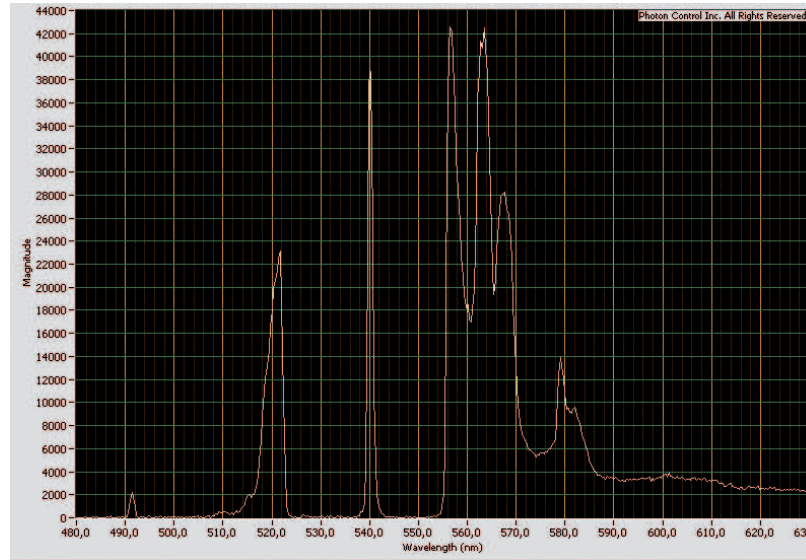


**Figure 3.10:** Spectrum of the output of the PCF when pumped with 532 nm pulses with vertical polarisation with an average pump power of around 10 mW. A clear peak at 491.0 nm is visible - a recalibration of the spectrometer yields 490.5 nm for the central wavelength of this peak. It stems from one of the output modes of a spontaneous four-wave-mixing process (SFWM,  $2 \times 532 \text{ nm} \rightarrow 490.5 \text{ nm} + 581.5 \text{ nm}$ ). The spike at 540 is a left over from Raman scattering by the pump not fully blocked by an edge filter. One can also see light from (higher order) Raman scattering, both on the Stokes and anti-Stokes side of the pump. A peak from the partner photon at around 579 nm (581.5 nm after recalibration) can also be identified - but sits on top of a broader higher order Raman peak.

Apart from the aimed for process, there are also phase-matched solutions for the creation of photon pairs by spontaneous four wave mixing (SFWM), when the fiber is only pumped with 532 nm pump pulses (see 3.2.4). In this parametric process the annihilation of two pump photons creates a pair of photons - similar to spontaneous parametric down-conversion. Experimentally, such a process has been employed for very efficient pair sources using silica fibers - e.g. [67, 4].



The phase-matching calculations for our PCF predict for a pump wavelength of 532 nm (with horizontal polarization) the generation of photon pairs around 490 nm and 580 nm (see 3.3.2). When only the 532 nm laser was launched into the PCF and we were able to observe this process: figure ?? shows a measurement with a standard spectrometer when approximately 10 mW of 532 nm pump light was launched into the fiber. The pump laser produced 6 ps pulses at a rate of 76 MHz and therefore had a peak power of about 20 W. This high peak power and the fact that the SFWM pair-creation process increases non-linear with the pump-power (see 3.2.4) explain why it is so bright that it can be observed with a standard spectrometer. In the spectrum one can clearly observe a peak with a central wavelength (after recalibration) of 490.5 nm. We successfully used this value to correct our dispersion data for the fiber that originally predicted a value of 495 nm, to get more reliable predictions for the wavelengths produced by the photon doubling.

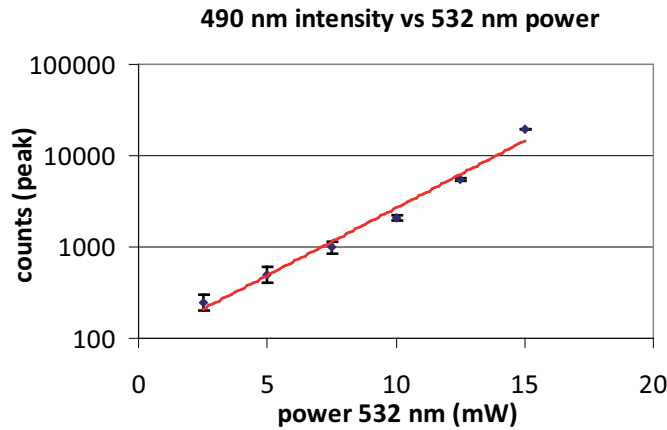


**Figure 3.11:** Plot of the maximum counts of the 490.5 nm signal from different spectrometer measurements for various average pump power. The dependence that is close to an exponential relation. The red solid line is an exponential fit to the data.

We also took spectra at different pump power levels ranging from 2.5 to 15 mW. For each of these spectra we then determined the heights of the peak at 490.5 nm and plotted them as a function of the average pump power. Figure ?? shows the resulting graph. The dependence of the intensity on the pump power follows closely an exponential increase. At first sight this seems surprising, as the pair production rate should theoretically follow a quadratic behaviour in the weak limit  $r \ll 1$  (see 3.2.4). However, in the

strong interaction regime ( $r \gg 1$ ) when higher-order terms dominate, an exponential increase of the average photon number is theoretically predicted. This exponential behaviour can here be clearly seen in our data and shows that for our high power levels, the parametric interaction is already very strong entering the exponential regime.

To sum up, we were able to observe SFWM pair-creation in our PCF pumped with 532 nm ps-pulsed light. The high brightness of this process – entering the strong interaction regime with an exponential increase with pump power – enabled us to determine the exact central wavelengths of the created pairs with a normal spectrometer. We then successfully used these wavelengths to correct the dispersion data for our fiber. This allowed more reliable predictions from the phase matching calculation for our actual target process as will be described in the next section.

### 3.4.2 Coherent photon conversion in PCF

#### Coincidences and background

In our target four-wave-mixing process input photons at 710 nm and the strong pulsed pump laser at 532 nm generate photon pairs at 504 nm ('green' arm) and 766 nm ('red' arm) realising photon-doubling of the 710 nm mode enhanced by the pump. The separation and filtering of the two modes and their detection and analysis is in detailed explained in the section about the experimental setup. In the following the results for identifying and characterising the rates of the photon pairs created by our target process are described. The analysis of the results is aimed at the stringent verification of the process as well as the quantitative characterisation of the interaction strength and how it depends on the pump power.

The main experimental data results from the start-stop histograms taken by our timing electronics that correlates the detection events in the two output modes in time. Figure ?? shows such a histogram for our first measurement in which we observed a coincidence signal from our process. The 532 nm pulsed pump with an average power of  $\approx 100$  mW and the weak input at 710 nm with  $\approx 8.5$  mW were launched into our PFC both with horizontal polarization. The two output modes are analysed in vertical polarization, as predicted by the phase-matching. Because the created photon pairs are strongly correlated in their creation – and therefore detection times – they can be identified as a sharp peak in the histogram. Such a peak can be clearly seen in figure ?. Its width is mainly determined by the combined timing jitter of the two detectors which is around 1 ns. The observation of

this coincidence peak shows the presence of photon pairs tightly correlated in time. The right polarization combinations and moreover the filters in the two output modes at the wavelengths expected from the phase-matching indicate very strongly, that the observed pairs indeed stem from the target process.

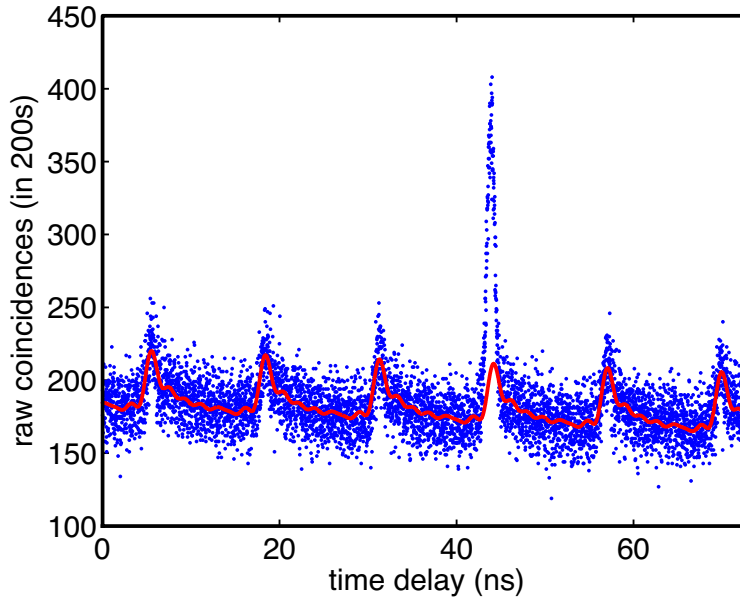


**Figure 3.12:** Plot of the raw data (blue dots) for the start-stop measurement integrated for 200 s of the two output modes at 504 nm and 766 nm. The Polarizations of the pump (532 nm) and input (710 nm) were both H and had average powers of  $\approx 100$  mW and  $\approx 8.5$  mW and that of the outputs V. The sharp coincidence peak at the offset of around 42 ns shows the creation of strongly time-correlated photon pairs. The red line represents a fit of the background with harmonics of the pulsed pump laser repetition rate of 76 MHz. It was derived from the data excluding a region around the coincidence peak.

One can also identify a relatively large background for this measurements. This background mainly stems from Raman scattering from the strong pump laser at 532 nm creating noise photons in both arms, but also from light caused by the 710 nm laser – only the 'red' output arm – also via Raman scattering. The first creates a periodic background pattern with the repetition rate of the pulses. In addition, the noise counts from the 710 nm laser in the 'red' arm together with the Raman noise in the 'green' arm from the 532 nm pulses will create a constant background. Nevertheless, we can precisely

measure and correct for this to accurately quantify number of pairs that are detected from the target process. For this the background in the histogram has been fitted for the region of the histogram excluding the part around sharp coincidence peak. To account for the periodic structure this fit uses a linear combination of a constant and a set of sinusoidal functions with a frequency equal to the pulse repetition rate and higher harmonics of it. When subtracted from the raw data the resulting histogram – shown in figure ?? – shows now only the signal from the target interaction. Adding up the counts in the bin belonging to the peak gives the total number of detected coincidences. For the data shown in figure ?? this procedure yields a rate of detected pairs of around  $1.5 \times 10^4$  counts per 200 second (or 75 cps). As shown later, this number is already affected by saturation effects of the detector and timing electronics and therefore not ideally suited for estimating the number of actually created pairs in the fiber. However, we can use this relatively strong signal to conclusively verify, that the detected coincidences indeed stem from the target interaction as explained in the following.

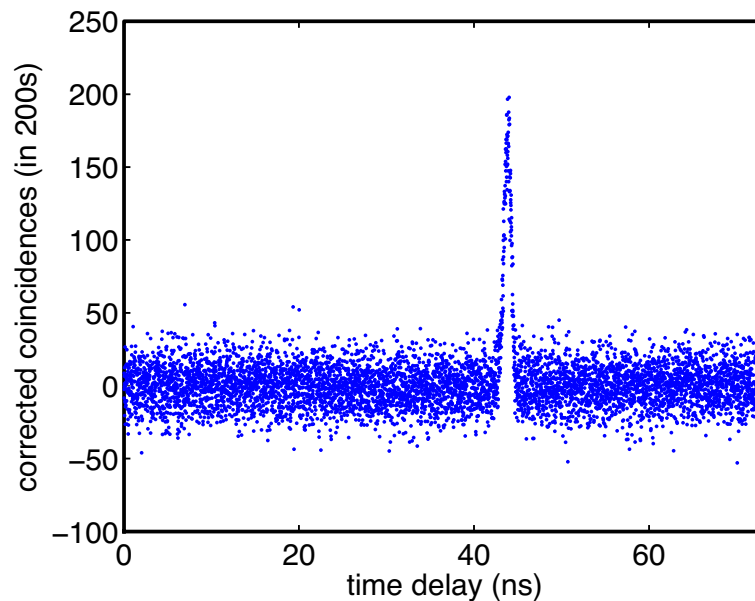


**Figure 3.13:** Result of the corrected raw data after subtraction of the background. The high scatter is a result of the big number of bins the whole interval was divided into with relative high Poissonian counting noise for each bin. Summing up over the coincidence peak yields  $14300 \pm 300$  counts per 200 s

A straightforward way to show, that the observed coincidences are genuinely

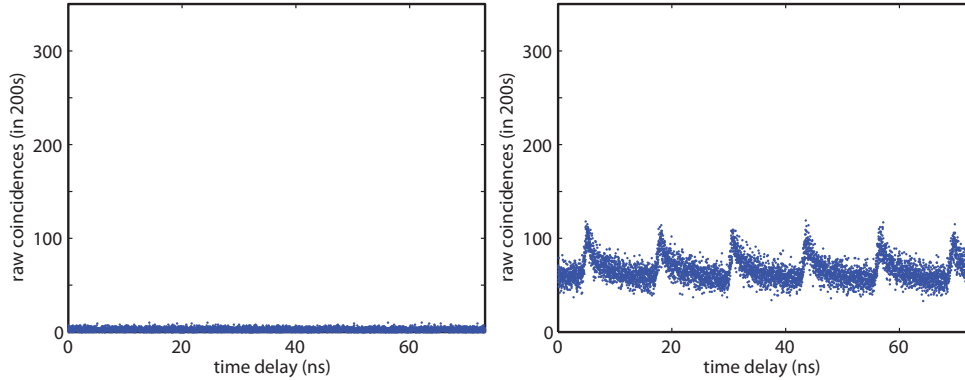


**Figure 3.14:** Plots of the raw data for the start-stop measurement for the cases with only the 710 nm light in the fiber – on the left – and when only the 532 nm pump was present – on the right. The power levels were same as for figure ???. For the 710 nm input only, there is a very low level. The pulsed structure on the right is a result of the background created from the 532 nm strong pump pulsed pump. No coincidence peak is present in either of the data sets which shows the the signal observed with both inputs is a genuinely combined effect.

a combined effect of the two different input, is presented in figure ??. Here, we measured the histograms for the two configurations where the 710 nm and 532 nm pump are launched separately into the PCF. One can clearly see, that no coincidence peak is present in either of the data sets. Interestingly, adding up the two histograms gives a smaller periodic background, than actually observed in the above measurement. The reason for this is that – as explained above – an additional constant background level is generated by the combination of noise counts from the 710 nm input and the 532 nm pump laser, which consequently cannot be present when both inputs are separately launched into the fiber.

### Polarization dependence

Another feature of our target interaction is its polarisation dependence. The phase-matching in the PCF is such that ideally only for the right polarization combination the process can take place. We therefore recorded the histograms for several different polarization combinations for the input and output modes. For each we applied the same procedure as before of precisely subtracting the background and evaluating the coincidence rate of the

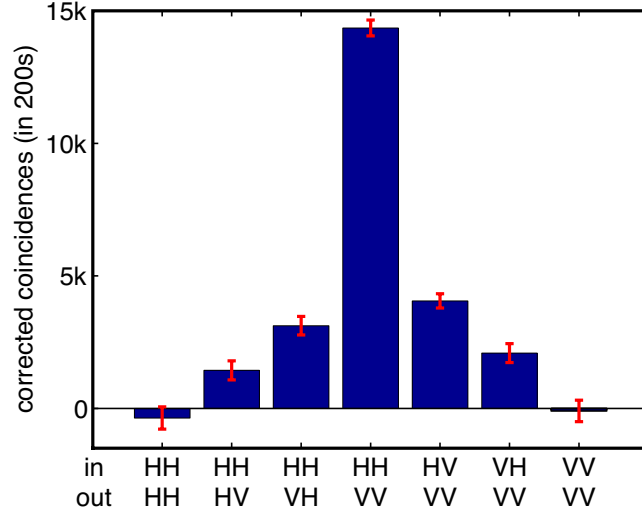


**Figure 3.15:** Number of measured coincidences for different combinations of input and output combinations. For the correct polarization combination (HHVV) the highest coincidence signal is observed. For combinations with an odd number of modes having horizontal (H) and vertical (V) polarization the corresponding element of the  $\chi^{(3)}$  tensor should be strictly zero because of the full rotational the symmetry of glass. We believe that those coincidences are actually created by the target process with the polarizations of the modes slightly changed before or after the interaction because of non-ideal fiber properties.

target process. The results are shown in figure ???. In the correct polarisation combination HHVV (inputs both H polarized, outputs both analysed in V) by far the most coincidences are detected. For combinations with equal polarizations (HHHH and VVVV) for all modes within statistical error no coincidences are detected. As an example, in figure ??? the resulting raw and corrected data is shown. There is no indication of any coincidence signal being present. This also further corroborates that the observed features in the main measurement genuinely result from our target interaction.

Theoretically all other combinations of polarizations beside the correct one should also yield no coincidences. This is because for all combinations with an odd number of modes being H and V polarized the corresponding element of the  $\chi^{(3)}$ -tensor for the four-wave-mixing interaction should be zero because of symmetry reasons [11]. Although, these symmetries of the material might be broken when in the form of a polarization maintaining photonic crystal

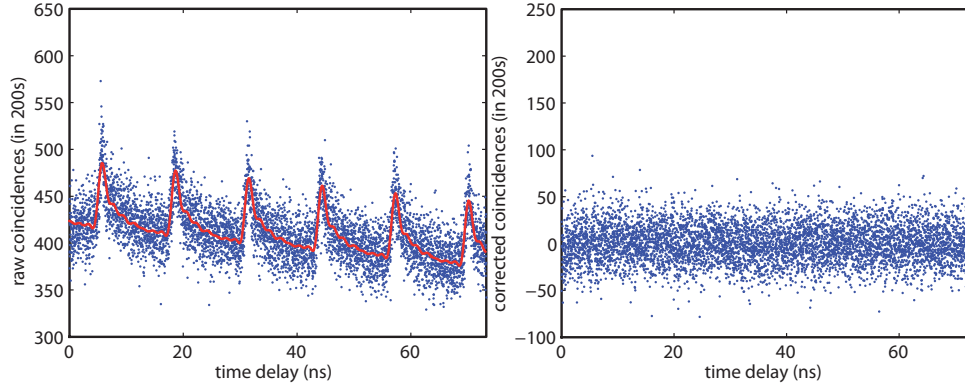


**Figure 3.16:** Results for the start stop measurement all modes being vertically polarised. Left the raw histogram and left the corresponding background corrected data. For this polarization combination, there is no phase matching for the target process, and as expected, no coincidence peak can be seen.

fiber by induced stress also the phase-matching would strongly suppress the interaction for these polarization combination. Nevertheless, experimentally for combinations with one polarization different than in the target process lower but not vanishing rates of coincidences were detected. We believe several different reason – or combinations of them – are responsible, for this deviation from the ideal: First, the orientation of the connectors for the polarisation maintaining fiber relative to the optical axis of have an accuracy of only a couple of degrees. This changes the input and output polarizations to a certain small degree. Second, the cut-off wavelength of our PCF is around 690 nm according to the manufactures specification. This means that at the pump wavelength (532 nm) as well as at the output wavelength of the 'green' arm (504 nm) the fiber is already bi-modal. If these higher modes were excited and mode coupling occurred, this could lead to a significant decrease in the polarization maintaining properties of the fiber. We therefore believe, that the observed coincidences, are most likely from the actual target process but with the input and output polarization altered inside the fiber before or after the interaction. This would explain the observed result qualitatively.

### Spectral dependence

We also *spectrally* characterised the two modes modes in which we create the photon pairs by our pumped four-wave-mixing process. For this we employed a combination of narrow bandpass filters (2 for each arm) that we angle-

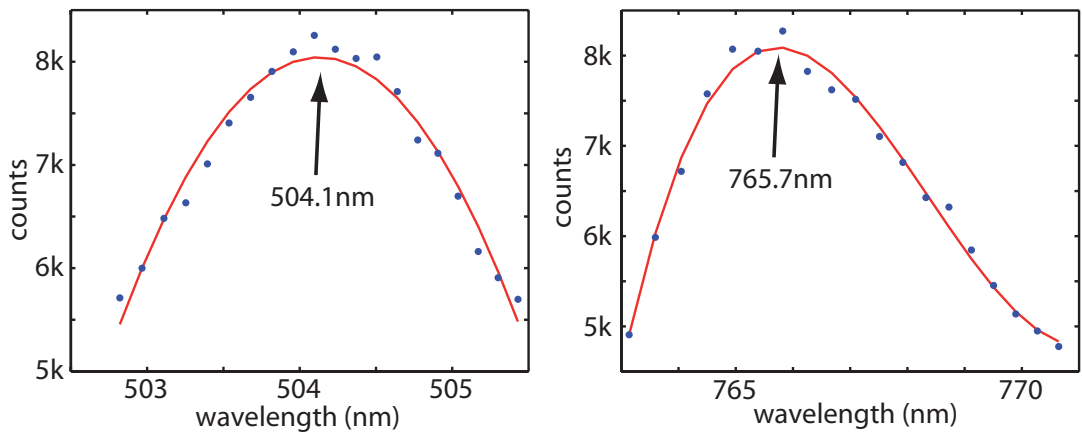


**Figure 3.17:** Result for of the spectral properties of photon pairs. Plots show the coincidence rates for 100 s integration and directly measured rates (with a single channel analyzer) with no background correction. In the left plot the bandpass filter in the "green" arm is set to 504 nm central wavelength and the "red" arm is scanned and the coincidences are recorded. In the plot on the right side the "red" arm is fixed at 766 nm and the "green" arm is scanned. The combination of two band-pass filters for each arm had a spectral width of around 2 and 3 nm FWHM for the "green" arm and "red" arm, respectively. For both spectra, the observed peaks appear to be broader than this.

tuned in a controlled and calibrated way (see section about the experimental setup). We also – instead of the timing histograms - we we used a single channel analyser to analyse the photon pairs. This allowed us to directly count the coincidences by correctly setting the delay and choosing a narrow coincidence window on the order of the coincidence peak that we saw in the histograms. Figure ?? shows the correspondingly measured spectra where we integrated for 100 s for each point. Note, however, that the such measured pair rates contain the previously observed background, which we could now not precisely correct for.

We first used this data the determine the central wavelengths for the peaks in both spectra by fitting to a polynomial and determining the maximum. The resulting central wavelengths of 504.1 nm and 765.7 nm closely agree with our phase-matching calculation. After correcting the slight error in the spectrometer calibration they also obey energy conservation, in the sense that the sum of their energies per photon matches that of the sum of the photon energies of the input photons at 532 nm and 710 nm. This fact adds



a final piece of evidence that the observed pairs are created by our target four-wave-mixing process.

Because of the limited tuning range for which we measured the spectra and also the high uncertainty about the level of background coincidences, that therefore could not be subtracted reliably, it is very hard to make precise statements about the width of the observed peaks in the spectra. In future experiments, higher resolution correlated single photon spectroscopy would be surely a valuable extended characterisation method. Nevertheless, the spectra indicated that the bandwidth of both of the created mode seems to be significantly broader than the combined bandwidth of the two filters in each arm (around 2-3 nm FWHM). Theoretically we would expect intrinsic bandwidths much smaller than that of 0.4 nm and 0.9 nm for the 'green' and 'red' arm, respectively. We believe, that inhomogeneities in the PFC leading to varying dispersion along the fiber could be responsible for the qualitatively observed broadening. In future experiments it will be interesting to analyse the broadening effect and how it, for example depends on the fiber length.

### Power dependence

An essential feature of our coherent photon conversion process is, that its interaction strength can be tuned and enhanced linearly with the pump power. The ultimate aim would be enhancing and setting the interaction to a level where unity conversion efficiencies could be achieved. This regime, characterised by the interaction parameter  $\Gamma t > 1$ , would enable the full potential of all the deterministic non-linear photon interactions outlined in the principles section of this chapter.

Here, we experimentally demonstrate the linear enhancement of the effective  $\chi^{(2)}$ -nonlinearity in the low-efficiency regime of our photon doubling process. For that we recorded the start-stop histograms for different pump powers with a fixed weak power of the cw 710 nm input light. We then used the same procedure as before to correct for the background and calculated the measured pair rates. A plot of these pair rates as a function of pump power is shown in figure ???. In the beginning the curve shows an almost perfect linear increase with the pump power. However, for higher powers (above 20 mW) a significant sub-linear behaviour can be observed. This is an artefact of the detection setup: for higher pump powers the single photon detectors as well as the start-stop timing electronics start to saturate. A simple model for the saturation is in very good quantitative agreement with the observed strength of the saturation effect. We therefore excluded the points above 20 mW for the fitting of the curve to a linear function, which is shown as the

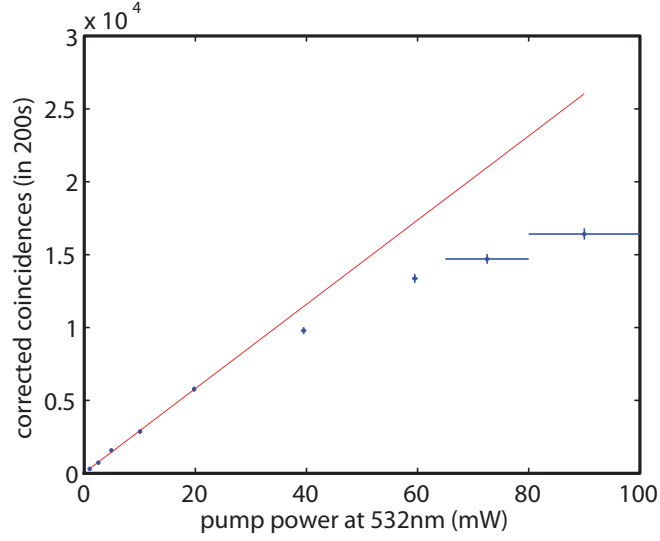


**Figure 3.18:** Dependence of the detected pair rates (corrected for background) of the target process on the pump power. The input intensity for the 710 nm mode was 8.5 mW as for the the previous Plots. The red line is a linear to the first 5 points yielding a rate  $1.45 \pm 0.02$  detected pairs per second per mW. At higher pump powers is below the linear increase, mainly by saturation in the detection system (detectors and logic) as well as reduced coupling efficiency of the high power 532 nm laser due to beam quality degradation

red line in the plot. From the fit, we can deduce the detected pair rate to be  $1.45 \pm 0.02$  pairs per second per mW and it is indeed linearly dependent on the 532 nm pump power.

To reliably quantify the nonlinear interaction parameter *inside* the PCF, we now need to account for the losses in our setup. These losses come from different contributions: the maximum transmission values for our bandpass filters and quantum efficiencies of the detectors for the respective wavelengths, could be taken from the specifications of the manufactures. In addition, we separately measured the remaining loss contributions. The following table summarizes these losses separately listed for the two arms:

Losses	Transm. 504 arm	Transm. 760 arm
PCF to SM coupling with various filters	$\sim 10\%$	$\sim 40\%$
SM to MM coupling in bandpass filter bridge	$\sim 90\%$	$\sim 90\%$
2× narrow bandpass filter	$\sim 90\%$	$\sim 90\%$
Fresnel losses at uncoated fiber tips	$\sim 90\%$	$\sim 90\%$
detector efficiency	$\sim 50\%$	$\sim 40\%$
total	$\sim 3.6\%$	$\sim 11.7\%$
total both arms	$\sim 0.4\%$	

Note that the high band-pass filter transmission is a conservative estimate (too high), because it assumes that the bandwidths of both created modes are much narrower than the filter bandwidth. The latter seems not to be the case – nevertheless, because we cannot reliably quantify how big the resulting additional loss would be, we use this upper bound, to not overestimate the generated pair rate.

The estimate of final total transmission of the arms adds up to about 0.4% – or in other words  $\frac{1}{235}$  of the created pairs in the PFC are detected in the end.

The 8.5 mW power of the cw input light at 710 nm corresponds to effectively 3.9  $\mu$ W or  $1.4 \times 10^{13}$  photons per second during the 6 ps pump pulse duration with a repetition rate of 76 MHz. From these numbers with the measured rate of  $1.45 \pm 0.02$  pairs per second per mW we conclude an efficiency  $\eta$  of the photon doubling inside the PCF of  $\sim 2.4 \times 10^{-11}$  per mW. For 20 mW – the highest pump power that does not lead to saturation effects of our detection system – we conclude a photon doubling efficiency of  $\sim 4.8 \times 10^{-10}$ . The corresponding interaction parameter extrapolated for 1 W of average pump power is then:

$$(\Gamma t)_{1W} = \sqrt{\eta_{1W}} \sim 1.5 \times 10^{-4} \quad (3.35)$$

From our approximate efficiency calculation we would expect an interaction parameter  $\Gamma t = 8.2 \times 10^{-4}$ . This is a bit more than 5 times higher than what we experimentally observe. Beside the approximations in the efficiency calculation itself, we believe that several experimental factors may contribute to the decrease in the experimentally observed value.

One effect is group velocity mismatches between the pump wave length and the input at 710 nm and the created wavelengths of 504 nm and 766 nm. For

pulsed input this would result in a finite interaction length of around 25 cm after which pulses of 6 ps would have walked off by 6 ps. However, by using a cw input at 710 this effect would only slightly influence the observed pair rates.

We also suspect that there are inhomogeneities along the fiber leading to variations in the dispersion properties. This would lead to a significantly broader bandwidth than what one would ideally expect. Our spectral measurements indeed indicate such a broadening. This would result in an additional loss for both arms and – accounting for that – to a higher interaction parameter. However, as explained above, it is difficult to quantify this with the current measurements. Measuring the spectrum of the output modes with a better spectral resolution and wider range than with our bandpass-filter arrangement would be necessary for that. Nevertheless, an effect leading to a correction of a factor of 5 seems not unlikely.

### 3.5 Conclusions and Outlook

Coherent photon conversion is a single pumped four-wave mixing process that provides a versatile array of tools which could have significant impact as building blocks for many quantum technologies, including quantum computing. In particular, we show that two of these building blocks are already sufficient to define a new CPC-based approach for photonic quantum computing that fulfils all of the DiVincenzo criteria, including providing heralded multi-photon sources with almost no higher-order terms, efficient and low-noise single-photon detection using real-world detectors and deterministic two-qubit entangling gates.

With our experiments we provide a proof-of-principle demonstration of the four-mode process underlying CPC, demonstrating that an effective  $\chi^{(2)}$  nonlinearity can be produced and tuned in a material where such a nonlinearity is otherwise unavailable. We stringently verify that we indeed observed the target four-mode process by polarization and spectral measurements, and by further showing the linear dependence of the strength of the interaction on the pump power. Furthermore, we experimentally determine the effective interaction strength  $((\Gamma t)_{1W} \approx 1.5 \times 10^{-4})$  and find a reasonable agreement with a simplified theoretical derivation of this parameter. By interpolating this result for chalcogenide glasses, that possess a  $10^3$  times higher third order nonlinearity we conclude that operation efficiencies near 100% could be achieved by using current, albeit sophisticated PCF technology, based on these highly nonlinear glasses. At the same time this represents a road

for future experiments with the ultimate aim of reaching the deterministic regime of CPC.

The availability of such nonlinearities in the optical regime would open the possibility of large-scale QIP with single and entangled photons. Furthermore, since CPC is derived from a  $\chi^{(3)}$  nonlinear interaction where near-degenerate operation is possible, this process is therefore compatible with telecom technology (unlike normal  $\chi^{(2)}$  processes) because all wavelength – including the pump wavelength – could be in the telecom band around 1550 nm. Consequently, CPC is furthermore ideally suited to integrated optics and waveguide applications which would open up a pathway for scaling this scheme up using standard techniques of integrated photonics. Finally, since our scheme is based only on interacting bosonic fields, it should also find application in optomechanical, electromechanical and superconducting systems where strong, intrinsic non-linearities are also readily available.

### **3.6 Publication Nature 478, 360-363 (2011)**

# Efficient quantum computing using coherent photon conversion

N. K. Langford<sup>1,2,3</sup>, S. Ramelow<sup>1,2</sup>, R. Prevedel<sup>1,4</sup>, W. J. Munro<sup>5,6</sup>, G. J. Milburn<sup>7,1</sup> & A. Zeilinger<sup>1,2</sup>

Single photons are excellent quantum information carriers: they were used in the earliest demonstrations of entanglement<sup>1</sup> and in the production of the highest-quality entanglement reported so far<sup>2,3</sup>. However, current schemes for preparing, processing and measuring them are inefficient. For example, down-conversion provides heralded, but randomly timed, single photons<sup>4</sup>, and linear optics gates are inherently probabilistic<sup>5</sup>. Here we introduce a deterministic process—coherent photon conversion (CPC)—that provides a new way to generate and process complex, multiquanta states for photonic quantum information applications. The technique uses classically pumped nonlinearities to induce coherent oscillations between orthogonal states of multiple quantum excitations. One example of CPC, based on a pumped four-wave-mixing interaction, is shown to yield a single, versatile process that provides a full set of photonic quantum processing tools. This set satisfies the DiVincenzo criteria for a scalable quantum computing architecture<sup>6</sup>, including deterministic multiqubit entanglement gates (based on a novel form of photon–photon interaction), high-quality heralded single- and multiphoton states free from higher-order imperfections, and robust, high-efficiency detection. It can also be used to produce heralded multiphoton entanglement, create optically switchable quantum circuits and implement an improved form of down-conversion with reduced higher-order effects. Such tools are valuable building blocks for many quantum-enabled technologies. Finally, using photonic crystal fibres we experimentally demonstrate quantum correlations arising from a four-colour nonlinear process suitable for CPC and use these measurements to study the feasibility of reaching the deterministic regime with current technology<sup>4,7</sup>. Our scheme, which is based on interacting bosonic fields, is not restricted to optical systems but could also be implemented in optomechanical, electromechanical and superconducting systems<sup>8–12</sup> with extremely strong intrinsic nonlinearities. Furthermore, exploiting higher-order nonlinearities with multiple pump fields yields a mechanism for multiparty mediation of the complex, coherent dynamics.

One of the key challenges for photonic quantum information processing is to induce strong, deterministic interactions between individual photons, which cannot be done using standard linear optical components. The scheme proposed for linear optics quantum computing in refs 5, 13 avoided this problem by using the inherent nonlinearity of photodetection and non-classical interference to induce effective nonlinear photon interactions non-deterministically. Alternatively, in the one-way picture of quantum computing, the required nonlinearities are replaced by offline probabilistic preparation of special entangled states followed by detection and feed-forward<sup>14–16</sup>.

Nonlinear optics quantum computing (NLOQC) takes a different approach, by directly using intrinsic nonlinearities to implement multiphoton interactions. NLOQC schemes using different types of optical nonlinearity, including cross-Kerr coupling<sup>17,18</sup> and two-photon absorption<sup>19</sup>, have been put forward. Since those proposals were made, more-complete multimode analyses of the cross-Kerr NLOQC schemes

have suggested that they cannot in fact produce phase shifts large enough for NLOQC because of spectral correlations created between the interacting fields<sup>20</sup>. Other work, however, shows that these difficulties can be circumvented in the related case of strong, second-order nonlinear ( $\chi^{(2)}$ ) interactions by carefully engineering the phase-matching conditions<sup>21</sup>.

Coherent photon conversion is an alternative nonlinear approach that uses coherent oscillations between different multi-excitation states. The underlying process is a nonlinear interaction between  $m$  bosonic modes that coherently converts single excitations in some of the modes (depending on the precise form of the interaction) into single excitations in the remaining modes. A key principle of CPC is that this basic nonlinearity can in turn be generated by pumping some modes of a higher-order nonlinearity with strong classical fields. This induces an effective coupling between the quantum modes that can be tuned and enhanced by the classical pumps, even to the point where the effective interaction is stronger than naturally occurring couplings of the same form. A similar effect is achieved in photon-pair sources based on four-wave mixing in photonic crystal fibres. Such systems have produced some of the highest-brightness photon-pair sources with very low pump powers<sup>7</sup>, and precise dispersion engineering and fibre-structuring technologies have allowed optimization of these sources to produce ultrabright, high-purity, heralded single photons<sup>4</sup>.

To illustrate the potential of CPC, here we focus on a novel case that has very interesting properties for quantum optics applications and which is based on the following standard four-wave-mixing interaction involving four distinct frequency modes ( $a$ ,  $b$ ,  $c$  and  $d$ ):

$$H = \gamma ab^\dagger c^\dagger d + \gamma^* a^\dagger bcd^\dagger \quad (1)$$

Here the coupling strength,  $\gamma$ , arises from the third-order ( $\chi^{(3)}$ ) nonlinearity, an asterisk denotes complex conjugate and a dagger denotes operator adjoint. Pumping mode  $d$  with a bright classical beam with electric field amplitude  $E$  yields the effective second-order interaction

$$\tilde{H} = \tilde{\gamma} ab^\dagger c^\dagger + \tilde{\gamma}^* a^\dagger bc \quad (2)$$

where  $\tilde{\gamma} \propto \gamma E$ . This now resembles a standard three-wave-mixing Hamiltonian with an enhanced, tunable, nonlinear coupling.

The key to understanding how this CPC process works, and its potential, is to note that an input Fock state,  $|n_a n_b n_c\rangle$ , will evolve within a well-defined, restricted Hilbert space,  $\{\tilde{H}^j |n_a n_b n_c\rangle | \forall \text{ integers } j\}$ , of dimension  $n_a + \min(n_b, n_c) + 1$ . Consequently, it will exhibit the collapses and revivals of individual population elements that are characteristic of coherent quantum processes. Most importantly for our scheme, for the two-dimensional subspace  $\{|100\rangle, |011\rangle\}$  ( $\tilde{H}|100\rangle \propto |011\rangle$  and  $\tilde{H}^2|100\rangle \propto |100\rangle$ ), the induced coupling drives Rabi-like oscillations between the two basis states. Given the input state  $|100\rangle$ , the output is

$$|\psi(t)\rangle = \cos(\Gamma t)|100\rangle + i \frac{\tilde{\gamma}}{|\tilde{\gamma}|} \sin(\Gamma t)|011\rangle \quad (3)$$

where  $\Gamma = |\tilde{\gamma}|/\hbar$  ( $\hbar$  being Planck's constant divided by  $2\pi$ ).

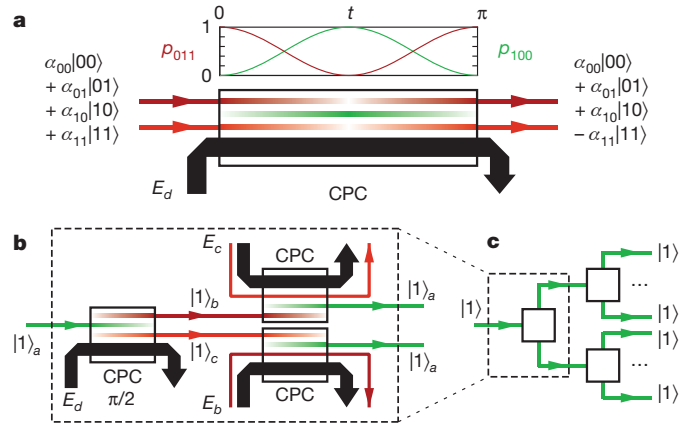
<sup>1</sup>Vienna Center for Quantum Science and Technology, Faculty of Physics, University of Vienna, Boltzmanngasse 5, A-1090 Vienna, Austria. <sup>2</sup>Institute for Quantum Optics and Quantum Information, Austrian Academy of Sciences, Boltzmanngasse 3, A-1090 Vienna, Austria. <sup>3</sup>Clarendon Laboratory, Department of Physics, University of Oxford, Parks Road, Oxford OX1 3PU, UK. <sup>4</sup>Institute for Quantum Computing, University of Waterloo, Waterloo, Ontario N2L 3G1, Canada. <sup>5</sup>National Institute of Informatics, 2-1-2 Hitotsubashi, Chiyoda-ku, Tokyo 101-8430, Japan. <sup>6</sup>NTT Basic Research Laboratories, NTT Corporation, 3-1 Morinosato-Wakamiya, Atsugi, Kanagawa 243-0198, Japan. <sup>7</sup>Centre for Engineered Quantum Systems, University of Queensland, St Lucia, 4072 Queensland, Australia.

Notably, standard single-photon up-conversion, a special case of CPC (indeed the simplest case), is one of the small subset of CPC processes with purely classical analogues. If a classical input field is used, then, provided that this ‘pump’ field remains undepleted throughout, the input field will undergo complete coherent oscillations between the two frequency modes. By contrast, if a classical input is used in the above example, then no coherent oscillations will be observed: the output is the well-known two-mode squeezed state of a parametric down-conversion source. In other words, in most cases a key element of CPC operation is the use of quantized inputs.

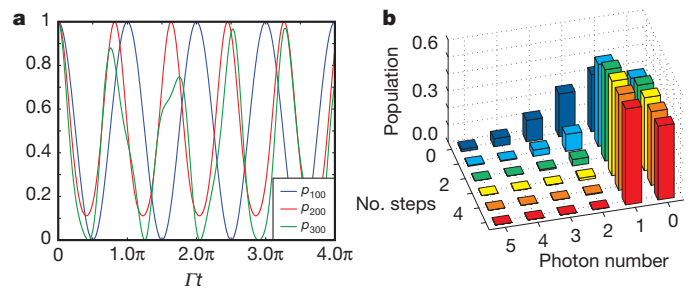
The basic conditions for a viable implementation of quantum computing are the DiVincenzo criteria<sup>6</sup>. The major unresolved challenges for photonic quantum information processing are good multiphoton sources, reliable multiqubit interactions and robust, high-efficiency single-photon detection. We show here that CPC provides tools to solve all three of these issues (Figs 1 and 2), all derived from a single process just by choosing different interaction strengths.

Figure 1a shows how CPC directly implements a two-qubit controlled-Z gate between the photons in the two modes *b* and *c*. The key insight is that CPC, like any coherent process that cycles between two orthogonal states, gives rise to geometric (Berry’s) phase effects<sup>22–25</sup>. Therefore, for  $t = \pi/I$ , an input state  $|011\rangle$  will undergo a full oscillation and undergo a phase shift of  $\pi$ , giving the final state  $-|011\rangle$ . This directly implements a maximally entangling, controlled-phase gate with 100% efficiency. We note that this geometric phase is truly non-classical and has no equivalent with classical input states. This controlled-Z gate can also be switched very fast optically (using the classical pump<sup>25</sup>), allowing the fast, real-time ‘rewiring’ of optical quantum circuits. This may have application in various adaptive quantum algorithms, such as quantum phase estimation, and might be particularly useful in waveguide and integrated-optics architectures.

If the input state undergoes half an oscillation ( $t = \pi/2I$ ), a single photon can be converted coherently and deterministically (with 100% efficiency) into two single photons—the process is a deterministic photon doubler<sup>26</sup> (or, in reverse, a deterministic two-photon absorber). Figure 1b illustrates one method for implementing a scalable photon



**Figure 1 | Satisfying the DiVincenzo criteria with CPC.** **a**, Deterministic controlled-phase gate. A ‘ $\pi$ ’ CPC interaction ( $t = \pi/I$ ) is an effective photon-photon interaction that implements an entangling controlled-Z gate between two logical states (for example polarization or spatial encoding) of photons with different frequencies. The input state,  $|\psi(0)\rangle = \sum_{ij} \alpha_{ij}|ij\rangle \equiv \sum_{ij} \alpha_{ij}|0ij\rangle$  is defined according to so-called ‘single-rail’ logic, where  $|ij\rangle$  denotes a state with *i* photons in mode *b* and *j* photons in mode *c*.  $E_d$  denotes a bright classical pump field in mode *d*. **b**, Scalable element for deterministic photon doubling. A ‘ $\pi/2$ ’ CPC interaction ( $t = \pi/2I$ ) can be used both to convert any single-photon source into a good source of multiphoton states and to perform high-efficiency, low-noise detection at any wavelength.  $E_j$  again denotes a bright classical pump field in mode *j*, and  $|1\rangle_j$  denotes a single-photon Fock state in mode *j*. **c**, Deterministic photon-doubling cascade. The scalable photon doubler from **b** (represented by the symbol in the dashed box) can be directly chained with others to create a deterministic cascade for either multiphoton state preparation or detection enhancement.



**Figure 2 | Heralded single-photon source.** **a**, Evolution of  $|n_a 0 0\rangle$  populations under the CPC interaction for  $n_a = 1, 2$  and  $3$ . This can be used to determine the optimal interaction length for preparing Fock states of different photon number. For example, like the controlled-Z gate, the one-photon Fock state preparation requires an interaction strength ( $I t$ ) corresponding to one full cycle of the state  $|100\rangle$  (compared with one full cycle of  $|011\rangle$  in the case of the controlled-Z gate). **b**, Number-state populations after each filtering step for  $t = \pi/I$ , giving  $|1\rangle_a$ . Combined with a single photon-doubling step and given a weak coherent input state with  $|\alpha|^2 = 1.5$ , in only five steps this scheme gives heralded single photons with high efficiency ( $\sim 56\%$ ) and minimal higher-order terms ( $< 0.3\%$ ).

doubler, allowing multiple doublers to be chained together to create an arbitrary number of photons (Supplementary Information). This efficient photon-doubling cascade (Fig. 1c) can be used to create a high-quality, scalable source of multiphoton states from any source of genuine single photons (on-demand or heralded). We note that the photon doubler can also be used in conjunction with existing methods to create arbitrary, heralded (also non-locally prepared) Bell-type two-photon and Greenberger–Horne–Zeinger-type three-photon entanglement, and that these tools can directly implement the encoding step for a simple nine-qubit error correction scheme<sup>27</sup> (Supplementary Information).

The same photon-doubling cascade (Fig. 1b) can also be used to perform high-efficiency, low-noise detection with real-world noisy, inefficient detectors by preceding detection with a ‘photon avalanche’ (Supplementary Information). Moreover, this technique can produce marked improvements in detector characteristics, even when the photon doubling efficiencies are less than 100%.

Finally, CPC can also be used to create a high-fidelity source of heralded single photons that could be used to seed the efficient photon-doubling cascade described above. As noted previously, higher-order input states,  $|n_a 0 0\rangle$ , will evolve within a restricted,  $(n_a + 1)$ -dimensional Hilbert space. As in the qubit case, this leads to coherent oscillations of population (see Fig. 2a for  $n_a = 1, 2$  and  $3$ ), but their complexity increases rapidly as  $n_a$  increases, because the evolution is governed by an increasingly complicated distribution of eigenfrequencies (see, for example, the  $n_a = 3$  case in Fig. 2a, and see Supplementary Information for details). As more competing frequencies come into play, for higher orders these oscillations are characterized by collapses and revivals in the input state population at often irregular times. Remarkably, these frequencies are incommensurate with the frequencies from other orders, so the revivals occur at different times for different input states (Fig. 2a).

We therefore consider an input state in mode *a* that is a superposition (or mixture) of states with different values of  $n_a$ , for example  $|\psi(0)\rangle_a = |\alpha\rangle_a$  (the latter a ‘classical’ coherent state). After one complete oscillation of the  $|100\rangle$  term (that is, after  $t = \pi/I$ , as for the controlled-Z gate), all other terms will, with non-zero probability, have converted into states with photons in modes *b* and *c*, which can be rejected using spectral filtering. Applying this process repeatedly will suppress all contributions from other orders, leaving only the  $|1\rangle_a$  state with a finite probability (Fig. 2b). (By detecting the dump port of the filtering step with high efficiency and rejecting trials that lead to detection events in these arms, this acts like a pure filter for Fock states<sup>28</sup>.) By combining this process with a single coherent photon-doubling step, it becomes a heralded single-photon source.

At present, spontaneous parametric down-conversion and spontaneous four-wave mixing provide the best available sources of heralded single photons, but the performance and achievable rates of these sources are intrinsically limited by the effects of higher-order photon-number terms<sup>29</sup>. By contrast, given a simple, weak coherent input state with  $|\alpha|^2 = 1.5$ , for example, in only five steps our scheme provides heralded single photons with production efficiencies of  $\sim 56\%$  and virtually no higher-order photon-number terms ( $< 0.3\%$ ) (Fig. 2b).

Using similar principles, CPC can also be used to create probabilistically other small Fock states with high fidelity (for example  $|200\rangle$ ) and to implement an improved form of down-conversion that can provide substantially higher pair-emission probabilities with much higher 'heralded' state fidelity than a standard down-conversion source with comparable emission rates (Supplementary Information).

From a practical perspective, there are several advantages to using a pumped  $\chi^{(3)}$  interaction to produce an effective  $\chi^{(2)}$  nonlinearity. First, although the  $\chi^{(3)}$  nonlinearity for a material is normally much weaker than the corresponding  $\chi^{(2)}$  nonlinearity (often by many orders of magnitude), the enhancement by the classical field can, for a sufficiently strong pump, result in an effective  $\chi^{(2)}$  nonlinear interaction that is stronger than the available natural  $\chi^{(2)}$  interaction. Also, materials with inversion symmetry have no  $\chi^{(2)}$  nonlinearity ( $\chi^{(2)} = 0$ ), whereas all materials possess a  $\chi^{(3)}$  nonlinearity. For example, amorphous glasses, for which there are highly advanced processing technologies, have a  $\chi^{(3)}$  nonlinearity but no  $\chi^{(2)}$  nonlinearity. Using the classical pump creates a quadratic nonlinearity that is tunable and no longer constrained by fixed material properties. Finally, and perhaps most importantly, conservation of energy allows the four-mode interaction to take place between nearly degenerate frequency modes, which makes CPC compatible with standard telecommunication-band, fibre-based implementations, unlike standard  $\chi^{(2)}$  interactions, in which the pump frequency must, by energy conservation, be the sum of the frequencies of the other two photons.

In our proof-of-principle experiments, we study a four-colour interaction in a photonic crystal fibre (PCF) that is a potential candidate for implementing CPC, and investigate the feasibility of reaching the deterministic regime. Specifically, we demonstrate the principle of creating a tunable  $\chi^{(2)}$  nonlinearity from a pumped  $\chi^{(3)}$  interaction, using a standard commercial, polarization-maintaining PCF, pumped with a 532-nm pulsed laser (Fig. 3). We then use weak coherent states from a 710-nm diode laser in mode  $a$  and characterize the feasible interaction strength using the resulting double-pumped correlated-pair source, with output photons with respective wavelengths of 504 and 766 nm.

Figure 4a shows the signal observed for an average power of  $\sim 90$  mW in the 532-nm pulses and an average power of  $\sim 8.5$  mW from the 710-nm diode laser. The diode laser delivers around  $10^5$  photons during each 532-nm pulse (that is, an effective power of  $\sim 4.8$   $\mu$ W), more than four orders of magnitude fewer than the pulsed pump. The background signals measured when only one beam is present show that the observed peak is a combined effect of both input beams. The full time trace allows us to correct very precisely for the periodic background and to isolate the signal that arises from the target four-colour nonlinear interaction that underlies our four-mode CPC process (Fig. 4b).

Figure 4c shows the dependence of the pair production rate on the pump power, which has a linear trend with some saturation at higher pump powers. The saturation arises predominantly from two technical effects, detector and counting saturation and reduced performance at high powers of generic single-mode fibres for spatial filtering, both of which can be addressed in future experiments. We can now use the results from Fig. 4c to estimate experimentally the nonlinear interaction strength,  $\Gamma t$ , that appears in equation (3). The linear fit (for the points up to a pump power of 20 mW) corresponds to a pair detection rate of  $1.45 \pm 0.02$  pairs per second per milliwatt of 532-nm pump power (error (s.d.) calculated using Monte Carlo simulation).

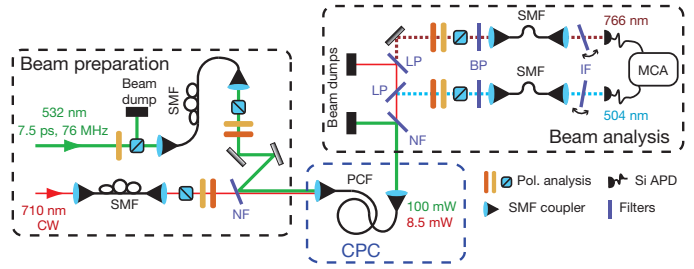


**Figure 3 | Experimental set-up.** There are three main stages: beam preparation (polarization state and spatial mode of input beams), CPC nonlinear interaction and beam analysis. The nonlinear medium is a standard commercial, polarization-maintaining PCF (core diameter, 1.8  $\mu$ m; nonlinearity,  $\sim 95$   $W^{-1}$   $km^{-1}$ ). The  $\chi^{(3)}$  nonlinearity is pumped by a frequency-doubled, pulsed neodymium vanadate (Nd:YVO<sub>4</sub>) laser (532 nm, 7.5 ps, 76 MHz) to create the desired tunable effective  $\chi^{(2)}$  nonlinearity. A continuous-wave (CW), external-cavity diode laser (710 nm,  $\sim 2 \times 10^7$  photons per Nd:YVO<sub>4</sub> pulse) provides the input state in mode  $a$  that we use to characterize the strength of the CPC interaction. From the estimated dispersion of the PCF, birefringent phase matching is satisfied for the following four-mode interaction: 532 nm (H) + 710 nm (H)  $\rightarrow$  504 nm (V) + 766 nm (V), where H and V denote horizontal and vertical polarizations, respectively. The 532-nm and 710-nm input beams are spatially filtered with single-mode fibres (SMF) before being combined on a notch filter (NF) and coupled into the PCF. The beams emerging from the output are then spectrally separated using a range of filters (NF; LP, long-pass filter; BP, band-pass filter) and a simple monochromator (a rotating interference filter (IF)), passed through polarization analysers and, finally, detected using avalanche photodiodes (APDs) and analysed in coincidence using time-to-amplitude conversion and a multichannel analyser (MCA).

Accounting for measured losses due to coupling and optical elements in the beam analysis circuit (transmissions:  $\sim 2.6\%$  in arm 1,  $\sim 14.6\%$  in arm 2), this corresponds to a nonlinear interaction parameter inside the PCF of  $\Gamma t \approx 5 \times 10^{-6}$  per (milliwatt)<sup>1/2</sup> (estimated directly from equation (3)). For 20 mW of pump power at 532 nm, this gives an effective brightness of  $\sim 10^6$  created pairs per milliwatt of effective input power at 710 nm (4.8  $\mu$ W).

We now discuss possible approaches to improving the effective  $\chi^{(2)}$  nonlinearity (see Supplementary Information for more detail). For a reasonable fibre-coupled pump power of 1 W, the measured rates predict that  $\Gamma t \approx 10^{-4}$ , which, with a single photon in mode  $a$ , would already give pair probabilities (per photon) comparable to present state-of-the-art, high-brightness spontaneous pair sources<sup>3,7</sup>. These interaction strengths could be further improved by using a lower repetition rate, so that the pulse energy can be increased without also increasing the average pump power; for example, using a system with a kilohertz repetition rate could perhaps improve  $\Gamma$  by another factor of up to  $10^2$ . Nevertheless, although we might reasonably expect future experiments to bring further technical improvements, for example by specifically engineering the nonlinear and dispersion properties of longer PCFs and matching them with the optical wavelengths, these initial results suggest that reaching the deterministic regime ( $\Gamma t \approx \pi/2$ ) using silica might be challenging. Other materials, however, provide access to far stronger  $\chi^{(3)}$  nonlinearities than does silica. For example, chalcogenide glasses, with a material  $\chi^{(3)}$  up to  $10^3$  times that of silica, have been used to make microstructured fibres, waveguides and nanowires, which have in turn been used in ultrabroadband telecommunication devices (see ref. 30 and references therein). Combined with high refractive indices, which allow for extremely strong mode confinement in chalcogenide integrated devices, such an increase in nonlinearity should provide a promising path towards interactions strong enough to make deterministic CPC possible.

We believe that CPC is a useful technique for implementing coherent, deterministic multiphoton dynamics both for applications in quantum-enhanced technologies and for fundamental tests involving entanglement and large-scale quantum systems. CPC also provides benefits in



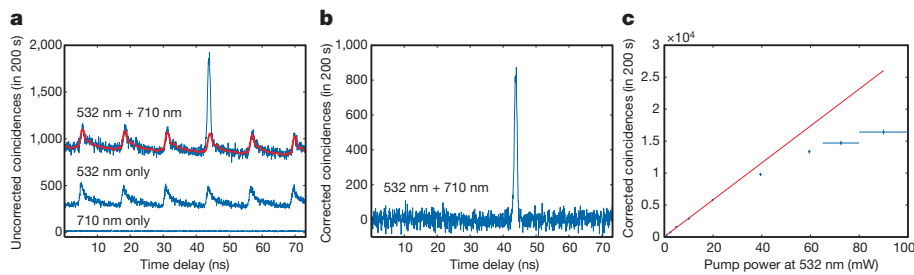


**Figure 4 | Experimental results.** **a**, Photon-doubling signal resulting from the four-mode nonlinear interaction that underlies our four-mode CPC. The signal (output polarization analysers both vertical) is only observed when both input beams are present (and horizontally polarized). The strong periodic background (fitted background signal shown in red; see Supplementary Information for more details) is caused by accidental coincidences from single photons created by Raman scattering from both beams, although very few such coincidences arise from just the 710-nm input because it creates very few Raman photons at 504 nm. **b**, The full MCA trace allows us to correct very precisely for this periodic background and isolate a background-subtracted signal that arises from only the CPC interaction. **c**, The pair production rate depends linearly on the pump power with some saturation at higher pump powers. The saturation arises predominantly from detector and counting

systems in which interaction strengths are substantially less than those required for deterministic operation. For example, because the photon doubler does not introduce any of the higher-order terms that limit the performance of down-conversion-based photon sources<sup>29</sup>, even at low efficiencies, a CPC-based multiphoton source offers the potential for higher multiphoton rates with much lower noise terms.

Finally, we emphasize that the above four-mode example of the CPC interaction demonstrates all of the building blocks required for a CPC-based approach to photonic quantum computing. These include deterministic two-qubit entangling gates based on a novel type of effective photon-photon interaction induced by Berry's phase effects, heralded multiphoton sources (potentially entangled) with almost no higher-order terms, and efficient, low-noise single-photon detection using real-world detectors. More specifically, all of these functions can be implemented using a single, reconfigurable, eight-port device (with an input and output for each mode) controlled by choosing the appropriate inputs, for example by tuning the interaction strength with the pump power.

Received 9 June; accepted 16 August 2011.

Published online 12 October 2011.

1. Clauser, J. F. & Shimony, A. Bell's theorem: experimental tests and implications. *Rep. Prog. Phys.* **41**, 1881–1927 (1978).
2. Barreiro, J. T., Langford, N. K., Peters, N. A. & Kwiat, P. G. Generation of hyperentangled photon pairs. *Phys. Rev. Lett.* **95**, 260501 (2005).
3. Fedrizzi, A., Herbst, T., Poppe, A., Jennewein, T. & Zeilinger, A. A wavelength-tunable fiber-coupled source of narrowband entangled photons. *Opt. Express* **15**, 15377–15386 (2007).
4. Cohen, O. *et al.* Tailored photon-pair generation in optical fibers. *Phys. Rev. Lett.* **102**, 123603 (2009).
5. Knill, E., Laflamme, R. & Milburn, G. J. A scheme for efficient quantum computation with linear optics. *Nature* **409**, 46–52 (2001).
6. DiVincenzo, D. P. & Loss, D. Quantum information is physical. *Superlattices Microstruct.* **23**, 419–432 (1998).
7. Fulconis, J., Alibart, O., Wadsworth, W. J., Russell, P. S. & Rarity, J. G. High brightness single mode source of correlated photon pairs using a photonic crystal fiber. *Opt. Lett.* **13**, 7572–7582 (2005).
8. Holmes, C. A. & Milburn, G. J. Parametric self pulsing in a quantum optomechanical system. *Fortschr. Phys.* **57**, 1052–1063 (2009).
9. Chang, D. E., Safavi-Naeini, A. H., Hafezi, M. & Painter, O. Slowing and stopping light using an optomechanical crystal array. *N. J. Phys.* **13**, 023003 (2011).
10. Thompson, J. D. *et al.* Strong dispersive coupling of a high-finesse cavity to a micromechanical membrane. *Nature* **452**, 72–75 (2008).
11. Moon, K. & Girvin, S. M. Theory of microwave parametric down-conversion and squeezing using circuit QED. *Phys. Rev. Lett.* **95**, 140504 (2005).
12. Marquardt, F. Efficient on-chip source of microwave photon pairs in superconducting circuit QED. *Phys. Rev. B* **76**, 205416 (2007).
13. Kok, P. *et al.* Linear optical quantum computing with photonic qubits. *Rev. Mod. Phys.* **79**, 135–174 (2007).
14. Raussendorf, R. & Briegel, H. J. A one-way quantum computer. *Phys. Rev. Lett.* **86**, 5188–5191 (2001).

saturation and the reduced performance at high powers of the generic SMFs used to spatially filter the 532-nm beam before it is coupled into the PCF. In particular, the detector saturation results mainly from unwanted Raman scattering, and it should be possible to suppress this effect drastically by cooling the PCF. Each point corresponds to a single 200-s integration. Vertical error bars represent statistical errors (s.d.) given Poisson-distributed coincidence counts. Horizontal error bars represent the worst case uncertainty (range) in pump power inside the PCF resulting from drift in fibre coupling during the course of the measurement. The linear fit (for the points up to 20 mW of pump power) corresponds to a pair detection rate (for 4.8  $\mu$ W of effective power in the 710-nm input) of  $1.45 \pm 0.02$  pairs per second per milliwatt of 532-nm pump power (the uncertainty (s.d.) was determined by Monte Carlo simulation with Poisson-distributed noise).

15. Walther, P. *et al.* Experimental one-way quantum computing. *Nature* **434**, 169–176 (2005).
16. Prevedel, R. *et al.* High-speed linear optics quantum computing using active feed-forward. *Nature* **445**, 65–69 (2007).
17. Munro, W. J., Nemoto, K., Beausoleil, R. G. & Spiller, T. P. High-efficiency quantum-nondemolition single-photon-number-resolving detector. *Phys. Rev. A* **71**, 033819 (2005).
18. Nemoto, K. & Munro, W. J. Nearly deterministic linear optical controlled-NOT gate. *Phys. Rev. Lett.* **93**, 250502 (2004).
19. Franson, J. D., Jacobs, B. C. & Pittman, T. B. Quantum computing using single photons and the Zeno effect. *Phys. Rev. A* **70**, 062302 (2004).
20. Shapiro, J. H. & Razavi, M. Continuous-time cross-phase modulation and quantum computation. *N. J. Phys.* **9**, 16 (2007).
21. Leung, P. M., Munro, W. J., Nemoto, K. & Ralph, T. C. Spectral effects of strong  $\chi^{(2)}$  nonlinearity for quantum processing. *Phys. Rev. A* **79**, 042307 (2009).
22. Berry, M. V. Quantal phase factors accompanying adiabatic changes. *Proc. R. Soc. Lond. A* **392**, 45–57 (1984).
23. Pancharatnam, S. Generalized theory of interference, and its applications—i. *Proc. Indian Acad. Sci. A* **44**, 247–262 (1956).
24. Rauch, H. *et al.* Verification of coherent spinor rotation of fermions. *Phys. Lett. A* **54**, 425–427 (1975).
25. VanDevender, A. P. & Kwiat, P. G. High-speed transparent switch via frequency upconversion. *Opt. Express* **15**, 4677–4683 (2007).
26. Koshino, K. Down-conversion of a single photon with unit efficiency. *Phys. Rev. A* **79**, 013804 (2009).
27. Shor, P. W. Scheme for reducing decoherence in quantum computer memory. *Phys. Rev. A* **52**, R2493–R2496 (1995).
28. Zeilinger, A., Horne, M. A. & Greenberger, D. M. in *Proc. Squeezed States Quantum Uncertainty* (eds Han, D., Kim, Y. S. & Zachary, W. W.) 73–81 (NASA Conference Publication 3135, NASA, 1992).
29. Barbieri, M. *et al.* Parametric downconversion and optical quantum gates: twos company, fours a crowd. *J. Mod. Opt.* **56**, 209–214 (2009).
30. Eggleton, B. J., Luther-Davies, B. & Richardson, K. Chalcogenide photonics. *Nature Photon.* **5**, 141–148 (2011).

**Supplementary Information** is linked to the online version of the paper at [www.nature.com/nature](http://www.nature.com/nature).

**Acknowledgements** The authors would like to acknowledge discussions with T. Jennewein, A. Fedrizzi, D. R. Austin, T. Paterek, B. J. Smith, W. J. Wadsworth, M. Halder, J. G. Rarity, F. Verstraete and A. G. White. This work was supported by the ERC (Advanced Grant QIT4QAD), the Austrian Science Fund (grant F4007 and an Erwin Schroedinger Fellowship), the EC (QU-ESSENCE and QAP), the Vienna Doctoral Program on Complex Quantum Systems, the John Templeton Foundation and in part by the Japanese FIRST programme and the Ontario Ministry of Research and Innovation.

**Author Contributions** N.K.L. and S.R. conceived the original theory and developed it with A.Z., G.J.M. and W.J.M. N.K.L., S.R., R.P. and A.Z. designed the experiment and N.K.L., S.R. and R.P. performed the experiment and carried out the data analysis. All authors contributed to writing the manuscript.

**Author Information** Reprints and permissions information is available at [www.nature.com/reprints](http://www.nature.com/reprints). The authors declare no competing financial interests. Readers are welcome to comment on the online version of this article at [www.nature.com/nature](http://www.nature.com/nature). Correspondence and requests for materials should be addressed to N.K.L. ([nathan.langford@univie.ac.at](mailto:nathan.langford@univie.ac.at)) or A.Z. ([anton.zeilinger@univie.ac.at](mailto:anton.zeilinger@univie.ac.at)).



## Chapter 4

# Discrete, tunable color-entanglement

## 4.1 Introduction

In this chapter the background and experimental results for the creation, tuning and verification of discrete tunable color-entanglement are presented. Color is one of the most intuitive properties of light and has been studied for a long time going back even to the beginning of the modern natural sciences. Nevertheless, in quantum optics experiments with single photons it has not played a major role, possible because it is arguably harder to manipulate when used for encoding quantum information in photons.

The idea to this experiment originated in realizing that single photon conversion in principle gives access to this not much explored degree-of-freedom (DOF) – the frequency, or color degree-of-freedom. When converted from one frequency to another but with only 50% efficiency, a photon will be brought in to a superposition of these two frequencies – perfectly analogue to a  $\pi/2$ -pulse in atom optics will bring an atom in a superposition of its ground and excited state. Therefore one can think of these discrete frequencies as the two eigenstates of a "color-qubit". We then thought about going even a step further by creating a state of two photons in a state of two entangled color qubits. Such a state had never been created before, although some proposals have been made. Remarkable, we then conceived a novel method, which does not involve frequency conversion, but could still generate such states simply by swapping over polarization entanglement to the color DOF by a "hybrid quantum gate" and a suitable input state of two non-degenerate, polarization entangled photons. A crucial ingredient was also that we could successfully employ the flexibility of our fiber coupled Sagnac-based entanglement source which allows for very easy tuning of the wavelength of the created photons without degrading its high quality polarization entanglement. It is also worth noting, that this idea of swapping entanglement between different DOFs can be used more general – for example also to swap entanglement from polarization the orbital angular momentum of photons, which has indeed stimulated further experimental efforts in our group.

A major challenge in our experiment was further to find a way to unambiguously verify and quantify color entanglement. Standard techniques that for example are used for polarization are not suitable here, because to measure directly in the superposition state of two relatively far away frequencies (with a separation on the order of THz) would have required fs timing resolution single photon detection, which is outside the range of current technology. However, we could use an indirect method that relied on quantum two-photon-interference in which the occurrence of anti-bunching is a stringent criterion for entanglement between the two interfering photons. By the

strength of the observed anti-bunching and other features in the measurement results we could even reconstruct a (restricted) density matrix of the created color entangled states and thereby fully characterize and quantify its properties. To demonstrate the flexibility of our setup we finally showed that our approach worked equally well for a full family of polarization entangled input states and more importantly also for different wavelength separation up to around 18 nm.

The following pages contain the final publication of these results that was published in Physical Review Letters. The work was a close cooperation of all co-authors, especially Lothar Ratschbacher, for whom this was part of his final graduation project.

## **4.2 Publication Phys. Rev. Lett. 103, 253601 (2009)**

## Discrete Tunable Color Entanglement

S. Ramelow,<sup>1,2</sup> L. Ratschbacher,<sup>1</sup> A. Fedrizzi,<sup>1,2,3</sup> N. K. Langford,<sup>1,2</sup> and A. Zeilinger<sup>1,2</sup>

<sup>1</sup>*Institute for Quantum Optics and Quantum Information, Austrian Academy of Sciences, Boltzmannngasse 3, A-1090 Vienna, Austria*

<sup>2</sup>*Faculty of Physics, University of Vienna, Boltzmannngasse 5, A-1090 Vienna, Austria*

<sup>3</sup>*Physics Department & Centre for Quantum Computer Technology, University of Queensland, Qld 4072, Australia*

(Received 30 April 2009; published 16 December 2009)

Although frequency multiplexing of information has revolutionized the field of classical communications, the color degree of freedom (DOF) has been used relatively little for quantum applications. We experimentally demonstrate a new hybrid quantum gate that transfers polarization entanglement of nondegenerate photons onto the color DOF. We create, for the first time, high-quality, discretely color-entangled states (with energy band gap up to 8.4 THz) without any spectrally selective filtering, and unambiguously verify and quantify the amount of entanglement (tangle,  $0.611 \pm 0.009$ ) by reconstructing a restricted density matrix; we generate a range of maximally entangled states, including a set of mutually unbiased bases for an encoded qubit space. The technique can be generalized to transfer polarization entanglement onto other photonic DOFs, like orbital angular momentum.

DOI: 10.1103/PhysRevLett.103.253601

PACS numbers: 42.50.Dv, 03.65.Wj, 03.67.Bg, 42.50.Ex

Color, or frequency, is one of the most familiar degrees of freedom (DOFs) of light and has been routinely analyzed in spectroscopy for centuries. However, although frequency multiplexing of information has had a profound impact on classical telecommunications, little work has aimed at exploiting the frequency DOF for quantum-based information technologies. A key ingredient in many such technologies is discretely encoded entanglement, which has been extensively investigated for other optical degrees of freedom (e.g., [1–9]). In contrast, discrete frequency entanglement has not yet been unambiguously demonstrated, despite potentially interesting applications such as enhanced clock synchronization beyond the classical limit [10,11], improved quantum communication in noisy channels [12], and novel dispersion cancellation techniques in quantum interferometry [13]. Flying qubits encoded in tunable frequency bins would also be an ideal mediator between stationary qubits with different energy levels; e.g., very recently the state of two photons emitted by two separate Yb ions was projected onto a discrete frequency-entangled state, allowing the creation of entanglement and realization of teleportation between the ions [14]. Finally, the higher-dimensional Hilbert space accessible with the color DOF has known benefits for quantum communication [15,16] and quantum cryptography [17–19], and would also allow the exploration of fundamental questions about quantum mechanics [20].

Continuous frequency entanglement between photon pairs arises naturally in spontaneous parametric down-conversion (SPDC) experiments as a consequence of energy conservation [5,21–23]. It is often, however, much simpler to control and use entanglement between systems with discrete, well-separated basis states (cf. time-bin entanglement [6]). A simple discrete-color-entangled state would be  $(|\omega_1\rangle|\omega_2\rangle + |\omega_2\rangle|\omega_1\rangle)/\sqrt{2}$ , where  $|\omega_j\rangle$  represent single-photon states occupying discrete, well-separated

frequency bins. Although some behavior of such a state can be realized in a destructive fashion by using broadband, continuous frequency entanglement and projecting onto separable frequency states during measurement (e.g., as in [21,22]), for most quantum applications it is necessary to use explicitly discrete quantum states that are not components of a broader continuous distribution. There have been some proposals and attempts to create and demonstrate discrete-color entanglement in nonlinear waveguides [24,25] and fiber Sagnac loops [26]. To date, however, no experiment has been able to conclusively show the creation or quantitative characterization of discretely color-entangled photons.

Here we report the first experimental demonstration of genuine discretely color-entangled states, created without any spectrally selective filtering. We used a hybrid quantum gate, a gate that acts simultaneously on different DOFs, that can deterministically transfer polarization onto color entanglement and unambiguously verified and quantified this entanglement using nonclassical interference. We also demonstrated full control over the frequency separation and phase of the created states, while maintaining a high fidelity.

In our experiment (Fig. 1), a tunable source of polarization entanglement based on continuous-wave SPDC [4] generates fiber-coupled photon pairs close to a pure state:

$$|\psi_{\text{in}}\rangle = (\alpha|H\rangle_1|H\rangle_2 + e^{i\phi}\beta|V\rangle_1|V\rangle_2) \otimes |\omega_1\rangle_1|\omega_2\rangle_2, \quad (1)$$

where  $\alpha^2 + \beta^2 = 1$ ,  $H$  and  $V$  denote vertical and horizontal polarization, and  $\omega_j$  is the central frequency of mode  $j$ . This notation neglects the spectral entanglement within the single-photon bandwidth, which was much less than the photons' frequency separation,  $\mu = \omega_1 - \omega_2$ . By varying the temperature of the source's nonlinear crystal (periodically poled potassium titanyl phosphate, ppKTP), we continuously tuned the photon frequencies from degeneracy

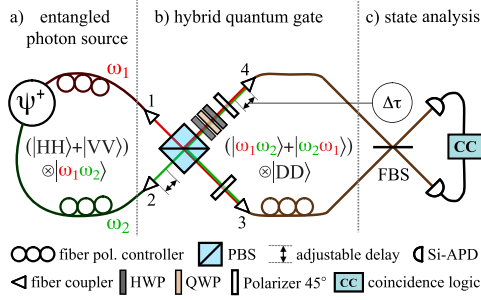


FIG. 1 (color online). Schematic of the experimental setup. (a) Source of polarization-entangled photon pairs with tunable central frequencies. (b) The hybrid quantum gate’s polarizing beam splitter (PBS) maps the polarization entanglement onto the color degree of freedom. Subsequently projecting on diagonal (D) polarization with polarizers (POL) generates the discretely color-entangled state. (c) The state is analyzed by two-photon interference at a fiber beam splitter (FBS); Si-APD single-photon detectors and coincidence counting (CC) logic measure the coincidence rate as a function of temporal delay between modes.

(809.6 nm at 25.1 °C) to a maximum separation of 8.4 THz (18.3 nm) at 68.1 °C while maintaining high-quality polarization entanglement [4]. We controlled the polarization state with wave plates.

Single mode fibers connect the source to the inputs of the hybrid gate depicted in Fig. 1(b). The polarizing beam splitter (PBS) maps the state  $|\omega_1\rangle_1$ , depending on its polarization, to  $|\omega_1\rangle_3$  ( $H$ ) or  $|\omega_1\rangle_4$  ( $V$ ), and similarly for the state  $|\omega_2\rangle_2$ . This transfers the existing polarization entanglement onto color with the resulting *hypoentangled* [27,28] multi-DOF state:

$$|\psi_{\text{hypo}}\rangle = \alpha|H\omega_1\rangle_3|H\omega_2\rangle_4 + e^{i\phi}\beta|V\omega_2\rangle_3|V\omega_1\rangle_4. \quad (2)$$

To create the desired state, the frequency entanglement must then be decoupled from the polarization DOF. This can be achieved deterministically by selectively rotating the polarization of one of the two frequencies (e.g., using dual-wavelength wave plates). For simplicity, we instead chose to erase the polarization information probabilistically by projecting both photons onto diagonal polarization using polarizers at 45°. We erased temporal distinguishability between input photons by translating fiber coupler 2 to maximize the nonclassical interference visibility at the PBS for degenerate photons. Finally, we compensated for unwanted birefringent effects of the PBS using wave plates in one arm. The gate output is then:

$$|\psi_{\text{out}}\rangle = \alpha|\omega_1\rangle_3|\omega_2\rangle_4 + e^{i\phi}\beta|\omega_2\rangle_3|\omega_1\rangle_4. \quad (3)$$

The parameters defining this state can be set by preparing an appropriate polarization input state [Eq. (1)].

To explore the performance of the hybrid gate, we first injected photon pairs close to the polarization state  $(|H\rangle_1|H\rangle_2 - |V\rangle_1|V\rangle_2)/\sqrt{2}$  with individual wavelengths 811.9 and 807.3 nm. The gate should then ideally produce the discrete, anticorrelated color-entangled state:  $|\psi\rangle =$

$(|\omega_1\rangle_3|\omega_2\rangle_4 - |\omega_2\rangle_3|\omega_1\rangle_4)/\sqrt{2}$ . Figure 2(a) shows the unfiltered single-photon spectra of the two output modes, illustrating that each photon is measured at either  $\omega_1$  or  $\omega_2$ . This reflects a curious feature of discretely color-entangled states, that individual photons have no well-defined color and no photon is ever observed at the “mean-value” frequency. This is one of the features that clearly distinguishes our experiment from the continuous frequency entanglement studied in Refs. [5,21,22].

Because the detuning,  $\mu = 4.6$  nm, is much larger than the FWHM bandwidth of the individual color modes of 0.66 nm (0.30 THz; defined by the 10 mm nonlinear crystal), the two modes are truly orthogonal, making them good logical states for a frequency-bin qubit. This orthogonality also means that color anticorrelations are strictly enforced by energy conservation, because a single down-conversion event cannot produce two photons in the same frequency bin. We confirmed this by directly measuring the gate output in the frequency-bin computational basis (i.e., with coarse-scale 2 nm-wide filtering in each arm at either  $\omega_1$  or  $\omega_2$ ). We observed strong, comparable coincidence rates for the two “anticorrelated” basis states ( $10882 \pm 104$  and  $9068 \pm 95$  in 30 s for  $|\omega_1\rangle_3|\omega_2\rangle_4$  and  $|\omega_2\rangle_3|\omega_1\rangle_4$ , respectively), and no coincidences for the same-frequency states ( $|\omega_1\rangle_3|\omega_1\rangle_4$  and  $|\omega_2\rangle_3|\omega_2\rangle_4$ ) to within error bars determined by the filters’ finite extinction ratios.

To demonstrate that the color state was not only anticorrelated but genuinely entangled, we used nonclassical two-photon interference [29], overlapping the photons at a 50:50 fiber beam splitter (FBS) [Fig. 1(c)] and varying their relative arrival time by translating fiber coupler 4 while observing the output coincidences. The results in

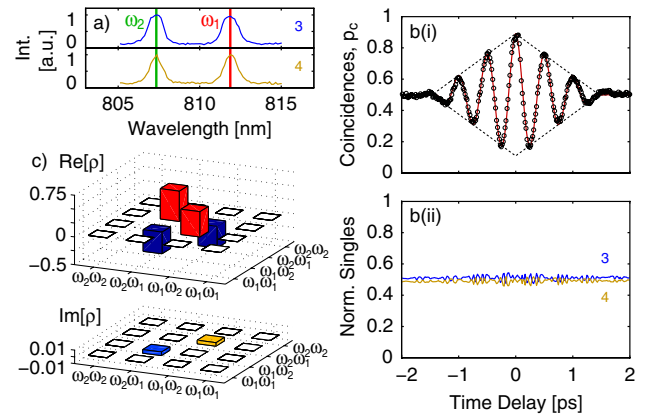


FIG. 2 (color online). Analysis of the discretely color-entangled state. (a) Single-photon spectra for modes 3 and 4; frequency separation is 2.1 THz (4.6 nm). The observed width of each bin is limited by the single-photon spectrometer. (b) Normalized (i) coincidence and (ii) singles count rates as a function of delay in mode 4. The solid line in (i) is a fit of Eq. (5) to determine  $V$  and the phase  $\phi$ . (c) The estimated restricted density matrix: target-state fidelity,  $0.891 \pm 0.003$ ; tangle,  $0.611 \pm 0.009$ ; and purity,  $0.801 \pm 0.004$ .

Fig. 2(b) show high-visibility sinusoidal oscillations (frequency  $\mu$ ) within a triangular envelope caused by the *unfiltered* “sinc-squared” spectral distribution of the source [4], whereas the single-photon detection rates exhibit negligible interference effects. At the central delay, the normalised coincidence probability reaches up to  $0.881 \pm 0.007$ , far above ( $>50\sigma$ ) the baseline level of 0.5. This two-photon antibunching is an unambiguous signature of antisymmetric entanglement [23,30,31] and, in conjunction with the measured single-photon spectra, conclusively demonstrates that we have created a truly discrete-color state that is strongly entangled. We emphasize again that our measurements do not rely on any spectrally selective filtering, but result from directly generated discrete color entanglement.

On its own, our measured nonclassical fringes are similar to those observed in previous work on frequency entanglement. However, as demonstrated by Kaltenbaek *et al.* [32], observing such a signal in different contexts cannot always lead to the same conclusions. In earlier experiments [21,22], the observed signal resulted from broadband, continuous frequency entanglement which was projected onto separable frequency states during measurement. At no point could the quantum state of the photons be described as both a discrete-color and a color-entangled state, as well as being uncoupled from other DOFs. In more recent work [26], Li and co-workers produced and verified high-quality continuous color entanglement using a Sagnac-based source. In principle, such a configuration might also produce discrete color entanglement, but their filter-based measurements alone would not be able to discriminate this from the continuous case.

We now show how we can combine the above measurements to estimate a restricted density matrix in color space. We first recall that energy conservation in the SPDC pair source and during photon propagation constrains the state to the two-dimensional anticorrelated subspace of the two-qubit color space (before and after the gate). This is a physical constraint, validated by the measurements in the computational basis. The complete density matrix within this subspace can be written (in the computational basis,  $\{|\omega_1\rangle_3|\omega_1\rangle_4, |\omega_1\rangle_3|\omega_2\rangle_4, |\omega_2\rangle_3|\omega_1\rangle_4, |\omega_2\rangle_3|\omega_2\rangle_4\}$ ):

$$\rho = \begin{pmatrix} 0 & 0 & 0 & 0 \\ 0 & p & \frac{V}{2}e^{-i\phi} & 0 \\ 0 & \frac{V}{2}e^{i\phi} & 1-p & 0 \\ 0 & 0 & 0 & 0 \end{pmatrix} \quad (4)$$

with real parameters that obey the physicality constraints:  $0 \leq p \leq 1$  and  $0 \leq \frac{V}{2} \leq \sqrt{p(1-p)}$ . Any detection events outside this subspace arise from higher-order emissions and accidental coincidences, and also lie outside the full two-qubit space. Our computational basis measurements showed that these vanished to within error bars, and we directly calculated the balance parameter,  $p = 0.546 \pm 0.004$  (using Poissonian errors). We estimated the remaining parameters by fitting them to the nonclassical interference

signal. For the above density matrix, given the source’s spectral properties, we analytically calculated the expected interference probability,  $p_c$ , to be (following [23])

$$p_c(\tau) = \frac{1}{2} - \frac{V}{2} \cos(\mu\tau + \phi) \left(1 - \left|\frac{2\tau}{\tau_c}\right|\right) \quad \text{for } |\tau| < \frac{\tau_c}{2}, \quad (5)$$

where the coherence time  $\tau_c$  is the base-to-base envelope width, related to the single-photon frequency bandwidth via  $\Delta f_{\text{FWHM}} = 0.885/\tau_c \sim 0.3$  THz. The missing elements  $V$  and  $\phi$  can be identified as the visibility and phase of the oscillating signal and can therefore be estimated using curve fitting (for this state,  $V = 0.782 \pm 0.006$  and  $\phi = 179.2 \pm 0.4^\circ$ ). The resulting density matrix [Fig. 2(c)] is strongly entangled, with a target-state fidelity of  $0.891 \pm 0.003$ , tangle [33] of  $0.611 \pm 0.009$ , and purity of  $0.801 \pm 0.004$  (error bars include Poissonian and fitting errors). This is the first quantitative measurement of the entanglement of any color-entangled state.

Several error sources in our experiment contributed cumulatively to unwanted photon distinguishability in the final color state and reduced the measured entanglement, including imperfect input polarization states, imperfect mode matching and residual polarization misalignment at the PBS, the finite PBS extinction ratio, and a slightly asymmetric FBS splitting. Accidental coincidence counts caused by detector dark counts and higher-order SPDC contributions were negligible.

To illustrate the flexibility of the hybrid gate, we analyzed a series of output states for different frequency detunings  $\mu$  and phases  $\phi$ . We first tuned  $\mu$  by varying the crystal temperature in the source, and the results (Fig. 3) agree well with Eq. (5). The source enabled us to reach a detuning of 18.3 nm (8.4 THz), about 30 times the individual color-bin bandwidths. The detunings estimated from curve fitting matched the single-photon spectra.

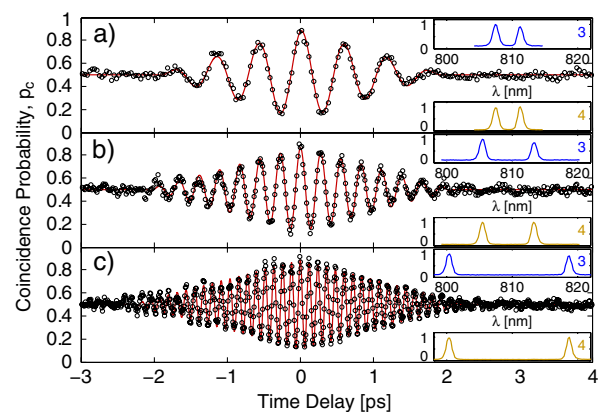


FIG. 3 (color online). Two-photon interference for color-entangled states with three different frequency separations (and corresponding crystal temperatures): (a) 1.7 THz (3.8 nm), 33.7 °C; (b) 3.6 THz (7.9 nm), 43.7 °C; and (c) 8.4 THz (18.3 nm), 68.1 °C. Solid lines are fits to Eq. (5) with  $V$ ,  $\mu$ , and  $\phi$  as fitting parameters. The insets show the measured single-photon spectra for both modes of each state.



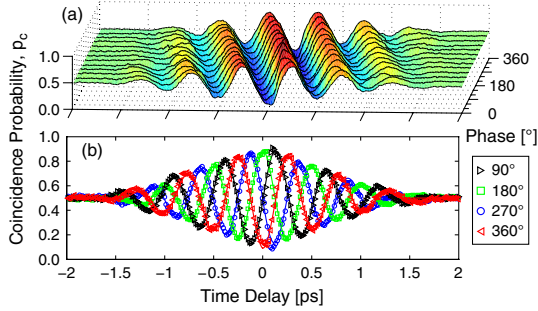


FIG. 4 (color online). (a) Coincidence probabilities after the FBS as a function of the delay for 13 close-to-maximally entangled discrete color states. The phase of the oscillation pattern is proportional to the phase of the original polarization-entangled state. (b) Four close-to-maximally entangled discrete-color states that represent two unbiased bases.

We next prepared discrete-color states of the form  $(|\omega_1\rangle_3|\omega_2\rangle_4 + e^{i\phi}|\omega_2\rangle_3|\omega_1\rangle_4)/\sqrt{2}$  with varying phase ( $\phi = 0^\circ, 30^\circ, \dots, 360^\circ$ ) (Fig. 4). The measured states display an average target-state fidelity of  $0.90 \pm 0.01$ , a tangle of  $0.63 \pm 0.03$ , and a purity of  $0.82 \pm 0.02$ , demonstrating that the hybrid gate accurately preserves quantum information stored in the original polarization state. Note that, together with the product states  $|\omega_1\rangle_3|\omega_2\rangle_4$  and  $|\omega_2\rangle_3|\omega_1\rangle_4$ , the entangled states with phase  $0^\circ, 90^\circ, 180^\circ$ , and  $270^\circ$  constitute a full set of qubit mutually unbiased bases. This illustrates the states' potential usefulness for quantum protocols such as quantum cryptography.

In this Letter, we have for the first time conclusively demonstrated the creation, control, and characterization of high-quality, discretely color-entangled states, prepared without any spectrally selective filtering using a hybrid quantum gate. We performed the first quantitative measurement of color entanglement using a novel technique for characterizing the two-qubit color state within a restricted, antisymmetric subspace defined by energy conservation. Our hybrid gate can in fact be used to transfer polarization entanglement onto any desired photonic DOF ( $\xi$ ), by preparing the input  $|\psi\rangle_{\text{pol}} \otimes |\xi_1, \xi_2\rangle$  and by appropriately erasing the polarization information after the PBS. Because the preparation of high-quality polarization states can be much easier than in other photonic DOFs, this gate represents a valuable tool for quantum information processing tasks in those DOFs. Our work also has important implications for the development of quantum memories and repeaters, because color-encoded information could provide a natural interface between flying and stationary qubits (such as single ions, atoms, or atom ensembles) where information is encoded in different energy levels. Indeed, by inverting the procedure from [14], one could potentially entangle distant ions directly by letting them absorb a photon pair with the appropriate discrete-color entanglement. Finally, we point out that genuine, discretely color-entangled states could also be extracted nondeterministically from broadband sources of continuous spec-

tral entanglement (such as traditional SPDC) using custom-designed multiband bandpass filters. This is a fundamentally different approach from previous experiments, where some signatures of discrete-color entanglement were reproduced by projecting onto discrete, separable states during measurement using single-band bandpass filters. Although this novel alternative would not be easily tunable and efficient, as ours is, it would allow access to higher-dimensional entangled states in the color DOF.

We would like to thank T. Jennewein and B. Blaustein and acknowledge support from the FWF (SFB 015 and CoQuS), the E.C. Project QAP, and the DTO-funded U.S. Army Research Office QCCM program.

- 
- [1] P.G. Kwiat *et al.*, Phys. Rev. Lett. **75**, 4337 (1995).
  - [2] P.G. Kwiat *et al.*, Phys. Rev. A **60**, R773 (1999).
  - [3] T. Kim, M. Fiorentino, and F.N.C. Wong, Phys. Rev. A **73**, 012316 (2006).
  - [4] A. Fedrizzi *et al.*, Opt. Express **15**, 15 377 (2007).
  - [5] P.G. Kwiat, A.M. Steinberg, and R.Y. Chiao, Phys. Rev. A **47**, R2472 (1993).
  - [6] J. Brendel *et al.*, Phys. Rev. Lett. **82**, 2594 (1999).
  - [7] J.G. Rarity and P.R. Tapster, Phys. Rev. Lett. **64**, 2495 (1990).
  - [8] A. Mair *et al.*, Nature (London) **412**, 313 (2001).
  - [9] N.K. Langford *et al.*, Phys. Rev. Lett. **93**, 053601 (2004).
  - [10] M. de Burgh and S.D. Bartlett, Phys. Rev. A **72**, 042301 (2005).
  - [11] V. Giovannetti, S. Lloyd, and L. Maccone, Nature (London) **412**, 417 (2001).
  - [12] L. Xiao *et al.*, Phys. Rev. A **77**, 042315 (2008).
  - [13] O. Minaeva *et al.*, Phys. Rev. Lett. **102**, 100504 (2009).
  - [14] S. Olmschenk *et al.*, Science **323**, 486 (2009).
  - [15] M. Fujiwara *et al.*, Phys. Rev. Lett. **90**, 167906 (2003).
  - [16] C. Wang *et al.*, Phys. Rev. A **71**, 044305 (2005).
  - [17] D. Bruss and C. Macchiavello, Phys. Rev. Lett. **88**, 127901 (2002).
  - [18] N.J. Cerf *et al.*, Phys. Rev. Lett. **88**, 127902 (2002).
  - [19] R.W. Spekkens and T. Rudolph, Phys. Rev. A **65**, 012310 (2001).
  - [20] S. Kochen and E.P. Specker, J. Math. Mech. **17**, 59 (1967).
  - [21] J.G. Rarity and P.R. Tapster, Phys. Rev. A **41**, 5139 (1990).
  - [22] Z.Y. Ou and L. Mandel, Phys. Rev. Lett. **61**, 54 (1988).
  - [23] A. Fedrizzi *et al.*, New J. Phys. **11**, 103052 (2009).
  - [24] M.C. Booth *et al.*, Phys. Rev. A **66**, 023815 (2002).
  - [25] M. Ravaro *et al.*, J. Appl. Phys. **98**, 063103 (2005).
  - [26] X. Li *et al.*, Phys. Rev. A **79**, 033817 (2009).
  - [27] N.K. Langford, Ph.D. thesis, Univ. of Queensland, 2007.
  - [28] X.-F. Ren *et al.*, Chin. Phys. Lett. **23**, 552 (2006).
  - [29] C.K. Hong, Z.Y. Ou, and L. Mandel, Phys. Rev. Lett. **59**, 2044 (1987).
  - [30] K. Mattle *et al.*, Phys. Rev. Lett. **76**, 4656 (1996).
  - [31] K. Wang, J. Phys. B **39**, R293 (2006).
  - [32] R. Kaltenbaek, J. Lavoie, and K.J. Resch, Phys. Rev. Lett. **102**, 243601 (2009).
  - [33] V. Coffman, J. Kundu, and W.K. Wootters, Phys. Rev. A **61**, 052306 (2000).



# Chapter 5

## Conclusions and Outlook

The conversion of photonic states opens up intriguing new possibilities for optical quantum experiments. This is a main overall conclusion that can be drawn from the three presented experiments in this thesis. The experiments are dedicated to studying the conversion of photons between different wavelengths (SPUC), conversion between different number states (CPC) and conversion of entanglement between different photonic degrees-of-freedom. Each of them have their specific motivations and fields of interest and they feature a wide range of possible application and possible future lines of research.

A specific conclusion of the single-photon upconversion experiment described in the first part of the thesis is that very high fidelity polarization entanglement preserving conversion can be implemented in a setup that is flexible, compact and robust. It uses simple bulk nonlinear materials, requires no complex cryogenic or vacuum apparatus, and is compatible with standard integrated-fibre and waveguide technologies. Thus, it is well-suited for large-scale deployment in quantum networks and possibly other future quantum technologies benefiting from quantum frequency conversion. Using longer crystals and moving to bi-directionally pumped schemes (e.g. Sagnac-type, or Michelson-type interferometers), as well as using high peak power pulsed lasers or nonlinear waveguide can significantly increase the efficiency. This, however, can be considered more of an engineering task than giving fundamentally new insights and was therefore not in the focus of this work.

Worth noting is, that the wavelengths in the presented setup are interchangeable. Converting 810 nm to 532 nm, as demonstrated here, has its merits – commercial 532 nm single-photon detectors can have up to 10 times lower timing jitter than their 810 nm counterparts and superconducting nano-wire detectors and CCD cameras are more efficient at shorter wavelengths. Up-

converting 1550 nm photons, however – particularly interesting for accessing fiber compatible wavelengths – can also be achieved by pumping with 810 nm, where powerful pulsed lasers are readily available.

As a side remark, it is interesting to realize that any polarization-coherent frequency conversion device using sum-frequency generation is equivalent to a polarization-entangled down-conversion pair source run in reverse. Therefore, most advantages of the designs and technologies for perfecting entanglement sources can be also used to optimise a quantum frequency-conversion experiment. For example one could think of an polarization coherent upconversion design, based on a polarization sagnac configuration in perfect analogy the sagnac-based polarization entanglement source.

As another future challenge, there is the interesting possibility of simultaneously changing the photon bandwidth by suitably designed phase-matching at the same time as converting the wavelength. This could prove extremely useful, especially in the context of interfacing photons with bandwidth-limited quantum memories.

The concept of coherent photon conversion (CPC) – introduced in the second part of the thesis – follows from generalizing single-photon upconversion and considering pumped parametric processes with higher order non-linearities. A main conclusion is, that an important example of this novel concept of CPC is a single pumped four-wave mixing process that provides a versatile array of tools which could have significant impact as building blocks for many photonic quantum technologies, including quantum computing. In particular, it is shown that two of these building blocks are already sufficient to define a new CPC-based approach for photonic quantum computing that fulfils all of the DiVincenzo criteria. This includes scalable two-qubit entangling gates based on a novel type of deterministic photon-photon-interaction, heralded multi-photon sources with almost no higher-order terms, and boosting efficiency and noise-resilience for single-photon detection with real-world detectors.

A main conclusion from the presented experimental results for the proof-of-principle demonstration of a four-mode process underlying CPC, is that an effective  $\chi^{(2)}$  nonlinearity can be produced and tuned in a material where such a nonlinearity is otherwise unavailable. The experimentally determined effective interaction strength is  $((\Gamma t)_{1W} \approx 1.5 \times 10^{-4})$  in reasonable agreement with a simplified theoretical derivation of this parameter. Importantly one can conclude, that by interpolating this result for example for chalcogenide glasses, that possess a  $10^3$  times higher third order nonlinearity, operation efficiencies near 100% could be achieved using current technology based on

these highly nonlinear glasses. At the same time this represents a road for future experiments with the ultimate aim of reaching the deterministic regime of CPC.

Technologically, since CPC is derived from a  $\chi^{(3)}$  nonlinear interaction where near-degenerate operation is possible, this process is therefore compatible with telecom technology (unlike normal  $\chi^{(2)}$  processes) because all wavelength – including the pump wavelength – could be in the telecom band around 1550 nm. Consequently, CPC is ideally suited to integrated optics and waveguide applications which is a promising future pathway for scaling this scheme up using standard optical integration techniques. Finally, since the CPC scheme is conceptually based on interacting bosonic fields (which are not limited to photons), it is an interesting question for future research if it can be applied in opto-mechanical, electromechanical and superconducting systems where strong, intrinsic non-linearities are also readily available.

For the third experiment, the main conclusion is that a good way of preparing entangled states in other photonic degrees-of-freedom than polarization is to convert them from polarization entanglement, which can be prepared reliably and with very high quality. This was shown in the experiment by creating – for the first time – discretely color-entangled states. Another interesting conclusion is related to the way entanglement was detected and verified in this experiment: Because it is technologically outside reach to detect in a superposition basis of two different color states anti-bunching in two-photon interference was used to unambiguously verify entanglement. This conceptually interesting method can in principle also be used for other degrees of freedom, where it is equally difficult to measure in different superposition bases. In future experiments discretely color-entangled states could be useful in dispersion-cancellation high-order interference experiments. Moreover, one proposal that builds on the main conclusion of this experiment is to convert polarization entanglement also to orbital angular momentum states of light. It is worth noting, that this was in the meantime already implemented in our group.



# Bibliography

- [1] Marius A. Albota. *Single-Photon Frequency Upconversion for Long-Distance Quantum Teleportation and Communication*. PhD thesis.
- [2] Marius A. Albota, Franco N. C. Wong, and Jeffrey H. Shapiro. Polarization-independent frequency conversion for quantum optical communication. *Journal of the Optical Society of America B*, 23(5):918–924, May 2006.
- [3] Marius A. Albota and Franco N. C. Wong. Efficient single-photon counting at  $1.55 \mu\text{m}$  by means of frequency upconversion. *Optics Letters*, 29(13):1449–1451, July 2004.
- [4] O Alibart, J Fulconis, G K L Wong, S G Murdoch, W J Wadsworth, and J G Rarity. Photon pair generation using four-wave mixing in a microstructured fibre: theory versus experiment. *New Journal of Physics*, 8(5):67–67, 2006.
- [5] J. A. Armstrong, N. Bloembergen, J. Ducuing, and P. S. Pershan. Interactions between light waves in a nonlinear dielectric. *Physical Review*, 127(6):1918, 1962.
- [6] Alain Aspect, Jean Dalibard, and Gerard Roger. Experimental test of bell’s inequalities using time-varying analyzers. *Physical Review Letters*, 49(25):1804, December 1982.
- [7] Julio T. Barreiro, Nathan K. Langford, Nicholas A. Peters, and Paul G. Kwiat. Generation of hyperentangled photon pairs. *Physical Review Letters*, 95(26):260501, December 2005.
- [8] John Bell. On the Einstein-Podolsky-Rosen paradox. *Physics*, 1:195–200, 1964.

- [9] M. V. Berry. Quantal phase factors accompanying adiabatic changes. *Proceedings of the Royal Society of London. A. Mathematical and Physical Sciences*, 392(1802):45–57, March 1984.
- [10] G. D. Boyd and D. A. Kleinman. Parametric interaction of focused gaussian light beams. *Journal of Applied Physics*, 39(8):3597–3639, July 1968.
- [11] Robert W. Boyd. *Nonlinear Optics: Third Edition*. Academic Press, 3 edition, April 2008.
- [12] J. Brendel, N. Gisin, W. Tittel, and H. Zbinden. Pulsed Energy-Time entangled Twin-Photon source for quantum communication. *Physical Review Letters*, 82(12):2594, March 1999.
- [13] Isaac L. Chuang and M. A. Nielsen. Prescription for experimental determination of the dynamics of a quantum black box. *Journal of Modern Optics*, 44:2455–2467, November 1997.
- [14] J F Clauser and A Shimony. Bell’s theorem. experimental tests and implications. *Reports on Progress in Physics*, 41(12):1881–1927, 1978.
- [15] John F. Clauser, Michael A. Horne, Abner Shimony, and Richard A. Holt. Proposed experiment to test local Hidden-Variable theories. *Physical Review Letters*, 23(15):880, October 1969.
- [16] Valerie Coffman, Joydip Kundu, and William K. Wootters. Distributed entanglement. *Physical Review A*, 61(5):052306, April 2000.
- [17] Nojima, Rob Thew, Christoph Simon, Nicolas Gisin, and Hugo Zbinden. Coherent frequency-down-conversion interface for quantum repeaters. *Optics Express*, 18(21):22099–22104, October 2010.
- [18] Eleni Diamanti, Hiroki Takesue, Toshimori Honjo, Kyo Inoue, and Yoshihisa Yamamoto. Performance of various quantum-key-distribution systems using 1.55- $\mu\text{m}$  up-conversion single-photon detectors. *Physical Review A*, 72(5):052311, November 2005.
- [19] D. P. DiVincenzo and D. Loss. Quantum information is physical. *Superlattices and Microstructures*, 23(3-4):419–432, March 1998.
- [20] Huafang Dong, Haifeng Pan, Yao Li, E Wu, and Heping Zeng. Efficient single-photon frequency upconversion at 1.06  $\mu\text{m}$  with ultralow background counts. *Applied Physics Letters*, 93(7):071101, 2008.



- [21] Y. O Dudin, A. G Radnaev, R. Zhao, J. Z Blumoff, T. A. B Kennedy, and A. Kuzmich. Entanglement of light-shift compensated atomic spin waves with telecom light. *1009.4180*, September 2010.
- [22] S.W. Dugan, X. Li, P.L. Voss, and P. Kumar. Frequency up-conversion at the single-photon level in a periodically-poled lithium-niobate waveguide. In *Quantum Electronics and Laser Science Conference, 2005. QELS '05*, volume 1, pages 661–663 Vol. 1, 2005.
- [23] Benjamin J. Eggleton, Barry Luther-Davies, and Kathleen Richardson. Chalcogenide photonics. *Nat Photon*, 5(3):141–148, March 2011.
- [24] A. Einstein, B. Podolsky, and N. Rosen. Can Quantum-Mechanical description of physical reality be considered complete? *Physical Review*, 47(10):777, May 1935.
- [25] Alessandro Fedrizzi, Thomas Herbst, Andreas Poppe, Thomas Jennewein, and Anton Zeilinger. A wavelength-tunable fiber-coupled source of narrowband entangled photons. *Optics Express*, 15(23):15377–15386, November 2007.
- [26] Alessandro Fedrizzi, Rupert Ursin, Thomas Herbst, Matteo Nespoli, Robert Prevedel, Thomas Scheidl, Felix Tiefenbacher, Thomas Jennewein, and Anton Zeilinger. High-fidelity transmission of entanglement over a high-loss free-space channel. *Nat Phys*, 5(6):389–392, June 2009.
- [27] J. D. Franson, B. C. Jacobs, and T. B. Pittman. Quantum computing using single photons and the zeno effect. *Physical Review A*, 70(6):062302, December 2004.
- [28] Stuart J. Freedman and John F. Clauser. Experimental test of local Hidden-Variable theories. *Physical Review Letters*, 28(14):938–941, April 1972.
- [29] Christopher Gerry and Peter Knight. *Introductory Quantum Optics*. November 2004.
- [30] G. Giorgi, P. Mataloni, and F. De Martini. Frequency hopping in quantum interferometry: Efficient Up-Down conversion for qubits and ebits. *Physical Review Letters*, 90(2):027902, January 2003.
- [31] N. Gisin. Bell’s inequality holds for all non-product states. *Physics Letters A*, 154(5-6):201–202, April 1991.

- [32] Nicolas Gisin, GrÃ©goire Ribordy, Wolfgang Tittel, and Hugo Zbinden. Quantum cryptography. *Reviews of Modern Physics*, 74(1):145, March 2002.
- [33] Shekhar Guha and Joel Falk. The effects of focusing in the three-frequency parametric upconverter. *Journal of Applied Physics*, 51(1):50–60, 1980.
- [34] Scott Hill and William K. Wootters. Entanglement of a pair of quantum bits. *Physical Review Letters*, 78(26):5022, June 1997.
- [35] Ryszard Horodecki, Pawel Horodecki, Michal Horodecki, and Karol Horodecki. Quantum entanglement. *quant-ph/0702225*, February 2007. *Rev. Mod. Phys.* Vol. 81, No. 2, pp. 865-942 (2009).
- [36] Jianming Huang and Prem Kumar. Observation of quantum frequency conversion. *Physical Review Letters*, 68(14):2153, April 1992.
- [37] Hannes Hubel, Deny R. Hamel, Alessandro Fedrizzi, Sven Ramelow, Kevin J. Resch, and Thomas Jennewein. Direct generation of photon triplets using cascaded photon-pair sources. *Nature*, 466(7306):601–603, July 2010.
- [38] Daniel F. V. James, Paul G. Kwiat, William J. Munro, and Andrew G. White. Measurement of qubits. *Physical Review A*, 64(5):052312, October 2001.
- [39] H. Kamada, M. Asobe, T. Honjo, H. Takesue, Y. Tokura, Y. Nishida, O. Tadanaga, and H. Miyazawa. Efficient and low-noise single-photon detection in 1550 nm communication band by frequency upconversion in periodically poled LiNbO3 waveguides. *Optics Letters*, 33(7):639–641, April 2008.
- [40] D. N. Klyshko. *JETP Letters*, page 23, 1967.
- [41] E. Knill, R. Laflamme, and G. J. Milburn. A scheme for efficient quantum computation with linear optics. *Nature*, 409(6816):46–52, January 2001.
- [42] Pieter Kok, W. J. Munro, Kae Nemoto, T. C. Ralph, Jonathan P. Dowling, and G. J. Milburn. Linear optical quantum computing with photonic qubits. *Reviews of Modern Physics*, 79(1):135, January 2007.
- [43] Kazuki Koshino. Down-conversion of a single photon with unit efficiency. *Physical Review A*, 79(1):013804, January 2009.

- [44] Prem Kumar. Quantum frequency conversion. *Optics Letters*, 15(24):1476–1478, December 1990.
- [45] Onur Kuzucu, Franco N. C. Wong, Sunao Kurimura, and Sergey Tovstonog. Joint temporal density measurements for Two-Photon state characterization. *Physical Review Letters*, 101(15):153602–4, October 2008.
- [46] Onur Kuzucu, Franco N. C. Wong, Sunao Kurimura, and Sergey Tovstonog. Time-resolved single-photon detection by femtosecond up-conversion. *Optics Letters*, 33(19):2257–2259, October 2008.
- [47] Paul G. Kwiat, Klaus Mattle, Harald Weinfurter, Anton Zeilinger, Alexander V. Sergienko, and Yanhua Shih. New High-Intensity source of Polarization-Entangled photon pairs. *Physical Review Letters*, 75(24):4337, December 1995.
- [48] Paul G. Kwiat, Edo Waks, Andrew G. White, Ian Appelbaum, and Philippe H. Eberhard. Ultrabright source of polarization-entangled photons. *Physical Review A*, 60(2):R773, 1999.
- [49] N. K. Langford, S. Ramelow, R. Prevedel, W. J. Munro, G. J. Milburn, and A. Zeilinger. Efficient quantum computing using coherent photon conversion. *Nature*, 478(7369):360–363, October 2011.
- [50] Nathan K. Langford. *Encoding, Manipulating and Measuring Quantum Information in Optics*. PhD thesis, University of Queensland (UQ).
- [51] Carsten Langrock, Eleni Diamanti, Rostislav V. Roussev, Yoshihisa Yamamoto, M. M. Fejer, and Hiroki Takesue. Highly efficient single-photon detection at communication wavelengths by use of upconversion in reverse-proton-exchanged periodically poled LiNbO<sub>3</sub> waveguides. *Optics Letters*, 30(13):1725–1727, July 2005.
- [52] Matthieu Legrèj,  $\frac{1}{2}$ , Rob Thew, Hugo Zbinden, and Nicolas Gisin. High resolution optical time domain reflectometer based on 1.55 $\mu$ m up-conversion photon-counting module. *Optics Express*, 15(13):8237–8242, June 2007.
- [53] Patrick M. Leung, William J. Munro, Kae Nemoto, and Timothy C. Ralph. Spectral effects of strong  $\chi^{(2)}$  nonlinearity for quantum processing. *Physical Review A*, 79(4):042307, April 2009.

- [54] Adriana E. Lita, Aaron J. Miller, and Sae Woo Nam. Counting near-infrared single-photons with 95% efficiency. *Optics Express*, 16(5):3032–3040, March 2008.
- [55] P. Mataloni, O. Jedrkiewicz, and F. De Martini. Single-photon femtosecond detection by frequency mixing up-conversion optical gate. *Physics Letters A*, 243(5-6):270–274, July 1998.
- [56] H. J. McGuinness, M. G. Raymer, C. J. McKinstrie, and S. Radic. Quantum frequency translation of Single-Photon states in a photonic crystal fiber. *Physical Review Letters*, 105(9):093604, 2010.
- [57] Kae Nemoto and W. J. Munro. Nearly deterministic linear optical Controlled-NOT gate. *Physical Review Letters*, 93(25):250502, December 2004.
- [58] Michael A. Nielsen and Isaac L. Chuang. *Quantum computation and quantum information*. Cambridge University Press, 2000.
- [59] J. L. O’Brien, G. J. Pryde, A. G. White, T. C. Ralph, and D. Branning. Demonstration of an all-optical quantum controlled-NOT gate. *Nature*, 426(6964):264–267, November 2003.
- [60] Haifeng Pan and Heping Zeng. Efficient and stable single-photon counting at 1.55  $\mu\text{m}$  by intracavity frequency upconversion. *Optics Letters*, 31(6):793–795, March 2006.
- [61] Jian-Wei Pan, Dik Bouwmeester, Harald Weinfurter, and Anton Zeilinger. Experimental entanglement swapping: Entangling photons that never interacted. *Physical Review Letters*, 80(18):3891, May 1998.
- [62] T. B. Pittman, M. J. Fitch, B. C Jacobs, and J. D. Franson. Experimental controlled-NOT logic gate for single photons in the coincidence basis. *Physical Review A*, 68(3):032316, 2003.
- [63] J. F. Poyatos, J. I. Cirac, and P. Zoller. Complete characterization of a quantum process: The Two-Bit quantum gate. *Physical Review Letters*, 78(2):390, January 1997.
- [64] A. G. Radnaev, Y. O. Dudin, R. Zhao, H. H. Jen, S. D. Jenkins, A. Kuzmich, and T. A. B. Kennedy. A quantum memory with telecom-wavelength conversion. *Nat Phys*, advance online publication, 2010.

- [65] Matthew T. Rakher, Lijun Ma, Oliver Slattery, Xiao Tang, and Kartik Srinivasan. Quantum transduction of telecommunications-band single photons from a quantum dot by frequency upconversion. *Nat Photon*, 4(11):786–791, November 2010.
- [66] S. Ramelow, L. Ratschbacher, A. Fedrizzi, N. K. Langford, and A. Zeilinger. Discrete tunable color entanglement. *Physical Review Letters*, 103(25):253601, December 2009.
- [67] J. Rarity, J. Fulconis, J. Duligall, W. Wadsworth, and P. Russell. Photonic crystal fiber source of correlated photon pairs. *Optics Express*, 13(2):534–544, January 2005.
- [68] J. G. Rarity and P. R. Tapster. Experimental violation of bell’s inequality based on phase and momentum. *Physical Review Letters*, 64(21):2495, May 1990.
- [69] Lothar Ratschbacher. Diploma thesis - discrete photonic color entanglement and single-photon up-conversion.
- [70] William Paul Risk, Timothy R. Gosnell, and Arto V. Nurmikko. *Compact blue-green lasers*. Cambridge University Press, January 2003.
- [71] Rostislav V. Roussev, Carsten Langrock, Jonathan R. Kurz, and M. M. Fejer. Periodically poled lithium niobate waveguide sum-frequency generator for efficient single-photon detection at communication wavelengths. *Optics Letters*, 29(13):1518–1520, July 2004.
- [72] Bahaa E A Saleh and Malvin Carl Teich. *Fundamentals of photonics*. Wiley, New York, NY, 1991.
- [73] Nicolas Sangouard, Christoph Simon, Hugues de Riedmatten, and Nicolas Gisin. Quantum repeaters based on atomic ensembles and linear optics. *Reviews of Modern Physics*, 83(1):33, March 2011.
- [74] Thomas Scheidl, Rupert Ursin, Johannes Kofler, Sven Ramelow, Xiao-Song Ma, Thomas Herbst, Lothar Ratschbacher, Alessandro Fedrizzi, Nathan Langford, Thomas Jennewein, and Anton Zeilinger. Violation of local realism with freedom of choice. *0811.3129*, November 2008.
- [75] Jeffrey H. Shapiro. Architectures for long-distance quantum teleportation. *New Journal of Physics*, 4:47, July 2002.
- [76] Jeffrey H. Shapiro. Single-photon kerr nonlinearities do not help quantum computation. *Physical Review A*, 73(6):062305, June 2006.

- [77] Ichiro Shoji, Takashi Kondo, Ayako Kitamoto, Masayuki Shirane, and Ryoichi Ito. Absolute scale of second-order nonlinear-optical coefficients. *Journal of the Optical Society of America B*, 14(9):2268–2294, 1997.
- [78] Peter W. Shor. Scheme for reducing decoherence in quantum computer memory. *Physical Review A*, 52(4):R2493, October 1995.
- [79] Hiroki Takesue. Erasing distinguishability using quantum frequency Up-Conversion. *Physical Review Letters*, 101(17):173901–4, October 2008.
- [80] Hiroki Takesue. Single-photon frequency down-conversion experiment. *Physical Review A*, 82(1):013833, July 2010.
- [81] S. Tanzilli, W. Tittel, M. Halder, O. Alibart, P. Baldi, N. Gisin, and H. Zbinden. A photonic quantum information interface. *Nature*, 437(7055):116–120, 2005.
- [82] R. T. Thew, S. Tanzilli, L. Krainer, S. C. Zeller, A. Rochas, I. Rech, S. Cova, H. Zbinden, and N. Gisin. Low jitter up-conversion detectors for telecom wavelength GHz QKD. *New Journal of Physics*, 8:32, March 2006.
- [83] Aaron P. Vandevender and Paul G. Kwiat. High efficiency single photon detection via frequency up-conversion. *Journal of Modern Optics*, 51:1433–1445, July 2004.
- [84] Aaron P. VanDevender and Paul G. Kwiat. High-speed transparent switch via frequency upconversion. *Optics Express*, 15(8):4677–4683, April 2007.
- [85] Aaron P. VanDevender and Paul G. Kwiat. Quantum transduction via frequency upconversion (Invited). *Journal of the Optical Society of America B*, 24(2):295–299, February 2007.
- [86] Alipasha Vaziri, Gregor Weihs, and Anton Zeilinger. Experimental Two-Photon, Three-Dimensional entanglement for quantum communication. *Physical Review Letters*, 89(24):240401, November 2002.
- [87] Reinhard F. Werner. Quantum states with Einstein-Podolsky-Rosen correlations admitting a hidden-variable model. *Physical Review A*, 40(8):4277, October 1989.
- [88] W. K. Wootters and W. H. Zurek. A single quantum cannot be cloned. *Nature*, 299(5886):802–803, October 1982.

- [89] Anton Zeilinger, Gregor Weihs, Thomas Jennewein, and Markus Aspelmeyer. Happy centenary, photon. *Nature*, 433(7023):230–238, January 2005.





# Chapter 6

## Acknowledgements

First of all, I want to thank Prof. Zeilinger, for the unique opportunity to carry out the research that led to this thesis in his group. I greatly appreciated the chance to quite independently follow new ideas and also the great and productive atmosphere in the group.

Then, I would like to give my thanks to Andreas, who brought me to Vienna and was a big source of enthusiasm. The only one I met so far, who could follow my sometimes a bit winding line of thoughts so quickly, that he could – before I even finished the sentence – actually point out the weak spots or add some great aspect. Also I would like to thank Alessandro, for helping me with the first steps to become a "gelernter Österreicher" and introducing me to the secrets of entangled photon sources – but also to the secrets of living a good life in Vienna. Thanks also to Nathan, who is a great inspiration and taught me a lot of things and every discussion is a pleasure. Thanks to Lothar who I had the pleasure of supporting during his diploma thesis and who in fact made me aware of "The Big Bang Theory".

Johannes for all the great disputes about politics and society – but also for his calm wisdom when confronted with confused questions about physics. I thank Rupert, for his great moral support through the hardships of the finishing process and his always spirit-lifting attitude.

In general, I would like to thank all the people from the group I have not explicitly mentioned for the great cooperation and atmosphere and also very specially the administrative team – Dany, Verena, Aylin, Manuela and Andrea for all their wonderful support during the years.

Of course, warm thanks to my family for all their support. A very special "thank you" goes to Heidi for her motivating patience and energy and affection, without which this thesis is not imaginable.

***personal data***

---

Date of birth	6th November 1978
Place of birth	Berlin, Germany
Nationality	German

***studies***

---

01 – 04 / 2009	Secondment at the University of Queensland, Australia
09 / 2008	Physics school “Foundations of Quantum” in Bad Honnef
03 / 2008	QAP Spring school 2008, Bristol, UK
02 / 2007	QUROPE Winter School 2007, Obergurgl, Austria
since 3 / 2006	PhD about Single Photon Up-Conversion in the group of Prof. Anton Zeilinger
10 / 2005	diploma in physics, mark: 1.0 (distinction) elective subjects: computational physics, optics and spectroscopy diploma thesis on experiments with single photons from quantum dots
10 / 2003 – 10 / 2005	post graduate studies and diploma thesis about single photons and quantum dots for quantum information processing in the group of Prof. O. Benson at the Humboldt-Universität in Berlin
11 / 2002 – 08 / 2003	studies and project work at the University of Melbourne, Australia and the Centre for Quantum Computer Technology
10 / 1999 – 08 / 2002	post- and undergraduate studies at the Humboldt-Universität elective subject: theoretical computer science
07 / 1998	Abitur, mark: 1.3
09 / 1991 – 07 / 1998	Heinrich-Hertz-Gymnasium in Berlin, specialized gymnasium for mathematics and science
09 / 1985 – 08 / 1991	16. elementary school Berlin, Prenzlauerberg

***sponsorships and prizes***

---

09/2007 – 9/2010	PhD stipend from CoQuS doctoral program
10 / 2003	sponsorship from the Humboldt-Universität for studies at the University of Melbourne
07 / 2003	two prizes of the Behnken-Berger-Foundation for the best final exams in the compulsory courses of the postgraduate studies in solid state physics and high energy & particle physics
until 1997	several prizes in mathematics and physics competitions (e.g. 2 <sup>nd</sup> price at the national physics competition 1997, 1 <sup>st</sup> price at the national Mathematikolympiade 1994)

## ***employment and teaching***

---

since 11/2010	research assistant at IQOQI, Vienna, Austrian Academy of Sciences
06 / 2006 – 11/2010	PhD student at the University of Vienna
05 / 2005 – 09 / 2005	staff member at the exhibition “Albert Einstein – Engineer of the universe” in Berlin (technical support for the first publicly exhibited experiment with entangled photons)
10 / 2003 – 03 / 2005	tutor for the lectures of experimental physics at the Humboldt-Universität (teaching, preparation and marking of assignments and exams)
12 / 2002 – 07 / 2003	project student at the Melbourne node of the Centre for Quantum Computer Technology” at the University of Melbourne (different projects with atomic force microscopy and nano-fabrication)
08 / 1998 – 09 / 1999	civil service at the hospital Charité in Berlin

## ***Language Skills:***

---

German:	mother tongue
English:	fluent in speaking and writing (8 years at school, various special courses, 10 month + 4 month studying in Australia)
Russian:	basic skills in speaking and writing (7 years at school, 1 year language course at Humboldt University)

## ***Soft skill trainings:***

---

Scientific Publishing, Prof. Ascheron, 08.05.2008

## ***Publications:***

---

B. Wittmann\*, **S. Ramelow\***, (\*equally contributing), F. Steinlechner, N. K. Langford, N. Brunner, H. Wiseman, R. Ursin, Anton Zeilinger, *Loophole-free quantum steering*, arXiv:1111.0760 **(2011)**

N. K. Langford, **S. Ramelow**, R. Prevedel, W. J. Munro, G. J. Milburn & A. Zeilinger  
*Efficient quantum computing using coherent photon conversion*, **Nature 478**, 360-363, **(2011)**

R. Lapkiewicz, P. Li, C. Schäff, N. K. Langford, **S. Ramelow**, M. Wiesniak, A. Zeilinger  
*Experimental non-classicality of an indivisible quantum system*, **Nature 490**, 490-493, **(2011)**

**S. Ramelow**, A. Fedrizzi, A. Poppe, N. K. Langford, and A. Zeilinger  
*Polarization-entanglement conserving frequency conversion of photons*,  
arXiv:1106.1867 (2011), submitted to Phys. Rev. X

T. Scheidl, R. Ursin, J. Kofler, **S. Ramelow**, X. Ma, T. Herbst, L. Ratschbacher, A. Fedrizzi, N. K. Langford, T. Jennewein, A. Zeilinger, *Violation of local realism with freedom of choice*, **PNAS 107**, 19708-19713 **(2010)**

H. Hübel, D. R. Hamel, A. Fedrizzi, **S. Ramelow**, K. J. Resch, T. Jennewein, *Direct generation of photon triplets using cascaded photon-pair sources*, **Nature 466**, 601 **(2010)**,

**S. Ramelow\***, A. Fedrizzi\*, (\*equally contributing), A.M. Steinberg, A.G. White,  
*Matchgate quantum computing and non-local process analysis*, **New J. Phys.** **12**, 083027 (2010)

**S. Ramelow\***, L. Ratschbacher\*, (\*equally contributing), A. Fedrizzi, N. K. Langford, A. Zeilinger  
*Discrete, Tunable Color Entanglement*, **Phys. Rev. Lett.** **103**, 253601 (2009)

T. Scheidl, R. Ursin, A. Fedrizzi, **S. Ramelow**, X. Ma, T. Herbst, R. Prevedel, L. Ratschbacher, J. Kofler,  
T. Jennewein and A. Zeilinger, *Feasibility of 300 km quantum key distribution with entangled state*,  
**New J. Phys.** **11**, 085002 (2009)

N.K. Langford and **S. Ramelow** (application non-provisional patent filed 2009)  
*Extended Proposal - Coherent Photonic Frequency Conversion (CPFC) For Quantum Computing Using  
Pumped Four-Wave Mixing Processes*, Patent – no. 61/101,473, 30.September 2008, US Provisional

„Can Scientists Dance?“ John Bohannon, **Science**, Vol. 319. no. 5865, p. 905 (2008)

A. Poppe, H. Hübel, B. Schrenk, B. Blauensteiner, M. Hentschel, **S. Ramelow**, T. Kelling und A. Zeilinger,  
*„Der Einsatz verschränkter Photonen für die Quantenkryptographie“*  
**E & I**, Volume 124, Number 5, (2007)

M. Scholz, T. Aichele, **S. Ramelow**, and O. Benson  
*„Deutsch-Jozsa Algorithm using Triggered Single Photons from a Single Quantum Dot“*,  
**Phys. Rev. Lett.**, **96**, 180501 (2006)

T. Aichele, M. Scholz, **S. Ramelow**, O. Benson  
*„Non-Classical Light from Artificial Atoms“*  
*Book Chapter in Adv. Atomic and Mol. Physics*, Vol. 53, G. Rempe and M. Scully eds. (2006)

C.I. Pakes, **S. Ramelow**, S. Prawer and D.N. Jamieson  
*„Nanoscale electrical characterisation of trap-assisted quasi-breakdown fluctuations in  
SiO<sub>2</sub>“*, **Appl. Phys. Lett.**, **84**, 3142, (2004)

C.I. Pakes, D.P. George, **S. Ramelow**, A. Cimmino, D.N. Jamieson, S. Prawer  
*„Manipulation of single magnetic protein particles using atomic force microscopy“*,  
**J. Magn. Mat.**, 272-276s, E1232 (2004)